



DIGITAL ACCESS TO SCHOLARSHIP AT HARVARD

Circuit interactions between the cortex and basal ganglia

The Harvard community has made this article openly available.
[Please share](#) how this access benefits you. Your story matters.

Citation	No citation.
Accessed	February 17, 2015 12:22:18 AM EST
Citable Link	http://nrs.harvard.edu/urn-3:HUL.InstRepos:13129563
Terms of Use	This article was downloaded from Harvard University's DASH repository, and is made available under the terms and conditions applicable to Other Posted Material, as set forth at http://nrs.harvard.edu/urn-3:HUL.InstRepos:dash.current.terms-of-use#LAA

(Article begins on next page)

HARVARD UNIVERSITY
Graduate School of Arts and Sciences



DISSERTATION ACCEPTANCE CERTIFICATE

The undersigned, appointed by the
Division of Medical Sciences
Program in Neuroscience
have examined a dissertation entitled

Circuit interactions between the cortex and basal ganglia

presented by Arpiar Bruce Saunders
candidate for the degree of Doctor of Philosophy and hereby
certify that it is worthy of acceptance.

Signature: 

Typed Name: Dr. Naoshige Uchida

Signature: 

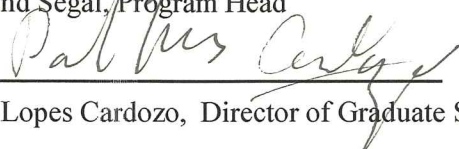
Typed Name: Dr. Beth Stevens

Signature: 

Typed Name: Dr. Mike Higley


Dr. Rosalind Segal, Program Head

Date: July 28, 2014


Dr. David Lopes Cardozo, Director of Graduate Studies

Circuit interactions between the cortex and basal ganglia

A dissertation presented
by
Arpiar Bruce Saunders

to
Division of Medical Sciences

In partial fulfillment of the requirement
for the degree of
Doctor of Philosophy
in the subject of Neurobiology

Harvard University
Cambridge, Massachusetts
July 2014

Circuit interactions between the cortex and basal ganglia

Abstract

All animals must adapt their behaviors by experience to survive. In mammals, this adaptive process is thought occur through a synaptic loop involving the cortex, basal ganglia (BG) and thalamus. Here we use transgenic mice and novel recombinant viruses (Chapter 1) to explore the brain circuits that underlie this interaction. Our focus is on how cell types within the BG affect cortical feedback during development and in adulthood.

Accepted models postulate that the BG modulate cerebral cortex 1) indirectly via an inhibitory output to thalamus and that this thalamic output is 2) bi-directionally controlled from within the BG by striatal direct (dSPNs) and indirect (iSPNs) pathway spiny neurons. In Chapter 2, we show that activity in iSPNs and dSPNs plays a complementary role in the post-natal synaptic wiring of the BG. Inhibiting iSPNs or dSPNs results in opposite changes in the number of excitatory synapses made onto SPNs from cortical and thalamic inputs. Our results suggest that the cortex-BG-thalamus function in a closed-loop and balanced iSPN/dSPN activity is required for proper synaptic wiring during development.

In Chapter 3, we describe a non-thalamic output of the BG to the frontal cortex (FC) emanating from globus pallidus externus (GP). The GP-FC projection consists of two cell types that release GABA and GABA/Acetylcholine, mostly onto cortical interneurons, with the net effect of increasing cortical firing rate. These results suggest that iSPNs and dSPNs can affect cortical output through GP-based disinhibition in addition to thalamus-based excitation. Moreover, GP-FC cells provide a pathway by which drugs that target dopamine receptors for the treatment of neuropsychiatric disorders can act in the BG yet modulate activity in FC. The presence of a direct BG output to cortex extends the looped architecture through which the cortex-BG-thalamus control adaptive behavior and can become dysregulated to cause disease. Together our thesis results support the phenomenology of the BG pathway model, but suggest a major revision to the underlying circuitry.

Table of Contents

Title Page.....	i
Copyright.....	ii
Abstract.....	iii
Table of Contents.....	v
Acknowledgements.....	vi
List of Figures.....	ix
List of Tables.....	xiii
Dedication.....	xiv
Chapter 1: Introduction.....	1
Chapter 2: Novel recombinant adeno-associated viruses for Cre activated and inactivated transgene expression in neurons.....	33
Chapter 3: Recurrent network activity drives striatal synaptogenesis.....	69
Chapter 4: A direct GABAergic output of the basal ganglia to frontal cortex.....	134
Chapter 5. Conclusion and outlook.....	212
Appendices.....	222

Acknowledgments

My PhD work has been enabled by the guidance, friendship, and resourcefulness of my mentor, Bernardo Sabatini. Working with Bernardo has been one of the greatest privileges of an already very privileged life. Bernardo is a scientific catalyzer in every sense and I have benefitted tremendously from his experimental, managerial, and philosophical tutelage. I am greatly indebted to Bernardo and he has my highest respect. He is an inspirational scientist and runs an inspirational lab.

I would also like to thank the members of my dissertation advisory committee – Bob Datta, Wade Regehr and Rachel Wilson - for their collective insight and support. I always looked forward to our meetings. David Cordoza has been supportive friend and scientist over the years and his presence is so crucial for the stability of the Neuroscience community at Harvard Medical School.

Bernardo's lab has attracted a staggering number of inspired scientists that have taught me so much over the years: Fitz Sturgill, Andrew Giessel, Matt Banghart, Mike Higley, Helen Bateup, Hyung Bae Kwon, Nic Tritsch, Yao Chen, Kevin Takasaki, Helen Hou, Shay Neufeld, Aurelien Begue, Adam Granger and Rui Peixoto. I have received much technical assistance from Caroline Johnson, Nazia Wolters and Rachel Pemberton and am profoundly grateful for their experimental help and collective sense of humor in dealing with my neuroses.

I have a very special place in my heart for my colleagues Genia Kozorovitskiy and Ian Oldenburg. Genia was instrumental in my decision to join the lab and over the first three years, we worked side by side on the study described in Chapter 3. Genia is

brilliant, a total data animal and an inspiring, caring and lovely friend. Genia always gives back to her colleagues and friends, making academic science more fun and egalitarian. I cherish the time we spent together.

Ian and I joined the lab at virtually the same time and we have been cosmically linked in our paths through graduate school. Ian is a curious and adventurous scientist and I am so thankful we could work together and employ his recording set up to describe the *in vivo* function of the cortical projection system from the globus pallidus externus described in Chapter 4.

A handful of other collaborators had a profound impact on generating or analyzing the data that went into Chapter 4. One of my favorite epochs of graduate school was with Vladimir Berezovskii, designing and executing the *Macaque* anatomy experiment. We worked in the same lab where Mesulam – thirty years earlier - did his now seminal anatomy experiments that were the basis for our work. Chip Gerfen at the NIH sectioned and imaged the several mouse brains for three dimensional reconstruction and analysis. I had so much fun and learned a lot from Hunter Elliott and Tiao Xie at the Image Data Analysis Core, who wrote custom software to analyze axonal densities and array tomography data, respectively.

My research iron has been forged by a group of friends who mean more to me than I have words and have kept Swarthmore College, Missoula and Boston always feeling like exactly the right place. The sciency-ones include the unparalleled Ben Ewen-Campen (main man & compass bearer), unstoppable John Tuthill, unquenchable Aaron Strong and unforgivable James Crall. The pseudo-sciency include the unflappable Pennie

Taylor and uncanny Blake Roberts. In beantown, Max Geller, Maude Baldwin, Fenna Krienen, Jacob Kramer and Ben Jordan have been the fossil fuel to the Shell sign of this thesis. Meeting my classmate Mehmet Fişek has been a true-life blessing and left me with an old world friendship I'll never be able to shake. Thanks also to my graduate classmates Dave Strohlic, Monica Thanawala, Raj Poddar, Abhinav Grama, Willie Tobin, Allison Baker, Anna Chamber and Alex Wiltschko.

During the course of this thesis I fell in love with and married my life-partner, Dr. Nadine Piekarski. Not only has Nadine's love and patience enabled me to complete this thesis, but her intuition for biology research and aesthetics challenged me and directly improved my work. Lastly, to my family, especially my Mom and sister Alice, who have supported me in every conceivable way in pursuing research in general and this PhD. Being able to live so close and pursue my curiosities with reckless abandon has been an amazing life gift. Thank you.

List of Figures

(in published or submitted chapters, underlining denotes main Figures; non-underlined Figures are Supplemental)

Chapter 1

1.1 Anatomical schematic depicting accepted position of BG nuclei within the cortex-BG-thalamus loop.....	7
1.2 Cell type based synaptic connectivity within the BG.....	11
1.3 Anti-psychotic drugs target D2Rs in the striatum and implicate iSPNs and GP cell types in their mechanism of action.....	17

Chapter 2

<u>2.1</u> Strategies to achieve Cre-dependent rAAV transgene expression.....	43
<u>2.2</u> DIO and DO rAAVs achieve Cre-On and Cre-Off expression but exhibit interfering interactions when co-infected.....	47
<u>2.3</u> A single orientation switching transgene can mediate Cre-On and Cre-Off expression without spatial interference.....	51
<u>2.4</u> LoxFAS excision achieves efficient Cre-Off rAAV expression that does not interfere with DIO Cre-On expression.....	55
<u>2.5</u> Cre-Off infection with DO rAAV interferes with the expression of fluorescent Cre reporter allele whereas infection with FAS rAAV does not.....	59
<u>2.6</u> Co-infection with DIO or DO/FAS rAAVs drives co-expression without spatial interference.....	62

Chapter 3

3.1 Schematic of cortex-BG-thalamus circuitry illustrating the impact of perturbing GABA release in the direct or indirect pathway.....	73
<u>3.2</u> Conditional knock out of <i>Slc32a1</i> from direct or indirect pathway MSNs abolishes GABAergic output.....	78
3.3 Whole-brain anatomical mapping of D1- and D2-Cre expression in inhibitory neurons.....	80

3.4 D1-Cre is not expressed in the vast majority of parvalbumin positive neurons in the striatum.....	82
3.5 Phenotypes of mice with conditional knock out of <i>Slc32a1</i> in direct or indirect pathway MSNs.....	84
3.6 Optogenetic activation of MSNs of direct and indirect pathways.....	86
3.7 GABA release is not required for MSN survival.....	89
3.8. GABA release is not required for the development of long-range axonal projections.....	91
3.9 Spontaneous mEPSCs in direct and indirect pathway MSNs of mice with conditional knockout of <i>Slc32a1</i>	93
<u>3.10</u> Conditional knock out of <i>Slc32a1</i> in direct and indirect pathway MSNs results in opposing changes to excitatory synapse number.....	96
3.11 Sparse postnatal <i>Slc32a1</i> deletion does not alter the frequency of mEPSCs or density and morphology of dendritic spines in MSNs.....	99
<u>3.12</u> <i>In vivo</i> , developmentally-restricted postnatal manipulation of activity in direct and indirect pathway MSNs results in opposing changes to excitatory synapse number.....	103
3.13 Cno application reduces optogenetically evoked spiking in MSNs and cortico-striatal projection neurons expressing hM4D-mCherry.....	105
3.14. <i>In vivo</i> hM4D-based manipulation of neural activity does not influence the amplitudes of spontaneous miniature EPSCs in MSNs.....	107
3.15. <i>In vivo</i> inhibition of indirect pathway MSNs using the Adora2a-Cre BAC recapitulates the increase in excitatory synaptogenesis observed using the D2-Cre BAC.....	109
<u>3.16</u> Cortico-striatal activity drives synaptogenesis in MSNs.....	113
3.17. Calibration of the laser power used to trigger glutamate uncaging induced spinogenesis in young MSNs.....	115
3.18. <i>In vivo</i> hM4D-based manipulation of neural activity in cortico-striatal projection neurons does not influence locomotion.....	118

Chapter 4

<u>4.1</u> The Globus Pallidus (GP) and bordering nucleus Basalis (NB) contain two GABAergic cell types that project to frontal cortex (FC).....	139
4.2 Anatomical and molecular properties of GP-FC cells and ChAT ⁺ cells of the Substantia Innominata (SI) and Ventral Pallidum (VP).....	142
4.3 ChAT ⁺ and ChAT ⁻ GP-FC cells are present in a <i>rhesus macaque</i>	146
4.4 Validation of <i>ChAT</i> ^{i-Cre} knock-in mouse and rAAV strategy for Cre-On/Off labeling of GP-FC cells.....	149
<u>4.5</u> GP-FC cells are distinguished by cortical projection patterns and electrophysiological properties.....	153
4.6 ChAT ⁺ and ChAT ⁻ GP-FC cells target distinct but overlapping subcortical nuclei.....	155
4.7 GP-FC cells are distinguished by active and passive membrane properties.....	157
4.8 Optogenetic manipulations of GP-FC cells coupled with <i>in vivo</i> extracellular FC recordings in awake behaving mice.....	160
<u>4.9.</u> ChAT ⁺ GP-FC cells activate FC <i>in vivo</i>	162
<u>4.10.</u> GP-FC cells release GABA and ACh in FC.....	167
4.11. ChAT ⁺ GP-FC cells ramify local axon collaterals around the GP/NB border.....	169
4.12. ChR2-mediated activation of <i>ChAT</i> ^{i-Cre} axons following rAAV transduction or with a Cre-activated allele evokes ACh and GABA mediated currents.....	173
4.13. Synaptic connectivity and array tomography marker co-localization analysis of GP-FC cells in FC.....	177
4.14. GP-FC cells receive glutamatergic synapses from STN and GABAergic synapses from dorsal striatal iSPNs and dSPNs with different presynaptic properties.....	183
<u>4.15.</u> The GP-FC projection is a basal ganglia (BG) output sensitive to anti-psychotic drugs.....	187

Appendices (A, Chapter 3; B, Chapter 4)

A.1 rAAV rescue of *Slc32a1* in striatum restores MSN GABAergic transmission.....224

B.1 GABAergic transmission from ChAT^{i-Cre} expressing neurons in cortex is *Slc32a1* dependent.....226

B.Movie 1 Three-dimensional whole-brain reconstructions of axonal projections from ChAT+ (magenta) and ChAT- (green) GP-FC cells.....227

B.Movie 2 Three-dimensional whole-brain reconstructions of axonal projections from iSPNs (green) and dSPNs (magenta) from dorsal striatum into GP/dorsal NB.....227

List of Tables

Chapter 1

1.1 Complete list of transgenic mouse lines.....	3
1.2 Complete list of recombinant adeno-associated viruses.....	4

Chapter 2

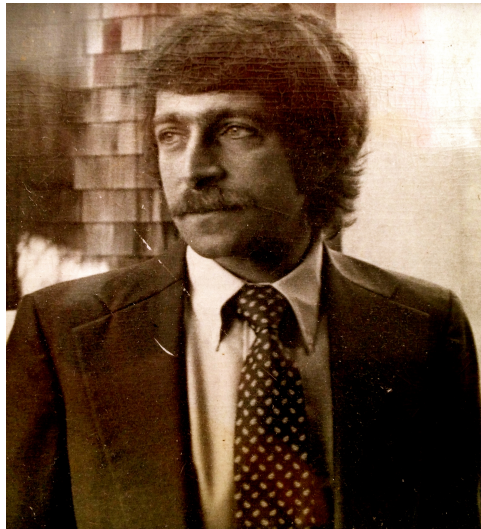
2.1 rAAV vectors and transgenes.....	41
--------------------------------------	----

Chapter 3

3.1 Transgenic mouse lines.....	124
3.2 Genotyping primers.....	124
3.2 Adeno-associated viruses.....	124

Dedication

This thesis is dedicated to my father, Arpiar George Saunders, in recognition of his love, kindness, humor and resilient strength. Thank you Dad for showing me you can make the world a better place by doing what you love.



Chapter 1

Introduction

Experimental framework

This thesis works toward a functional description of the brain circuits that interconnect the cortex and basal ganglia. The goal is to explain how individual circuit components interact to drive complex, emergent processes like behavior or post-natal development. My experimental framework focuses on four aspects of neural circuits and are generally applicable to the mammalian brain:

- 1. Cell types.** Brain circuits are composed of distinct cell types and that each type has plays a distinct role in circuit function. While no two cells are identical, cells can be functionally grouped based on anatomical location, morphology of the axon and dendrites, intrinsic physiological properties, released neurotransmitters, synaptic properties and molecular milieu, including transcriptional profile.
- 2. Synaptic connectivity.** Building a blueprint of synaptic connectivity between constituent cell types is necessary to understand how action potential firing in a given cell type affects the activity of other cell types and the circuit as a whole. Instances of ionotropic receptor signaling should be characterized by released neurotransmitters, post-synaptic receptors and short-term plasticity properties. Electrical synapses and their activity-dependent properties are also included.

3. **Modulatory sensitivity.** Neuromodulators affect circuit function by altering both intrinsic membrane and synaptic properties. To understand the net effect of a given modulator on a given circuit, it is necessary to define the sensitive cell type and synaptic components. This amounts to a “modulation layer” that overlays the synaptic blueprint of defined cell types.
4. **Monitoring emergent activity.** To relate how cell types interact through their synaptic and modulatory blueprints to produce complex processes, it is necessary to observe the circuit in action. *In vivo* recordings or imaging - especially where particular cell types or circuit components can be monitored or manipulated – are essential for mapping the mechanisms by which emergent circuit properties arise. For processes with longer time scales (e.g. post-natal development), experiments can be performed at various time points and these “snapshots” aligned to infer the state of the process.

Here we implement this framework using transgenic mice (Table 1.1) and recombinant viruses (Table 1.2) to label and manipulate genetically defined cell types. Chapter 2 describes novel recombinant adeno-associated viruses (rAAVs) - used in all subsequent chapters - that define the circuit function of one cell type with respect to its neighbors. Chapter 3 explores how activity in two known cell types of the striatum guide the wiring of the cortex and basal ganglia during post-natal development. Chapter 4 characterizes previously unappreciated cell types within the globus pallidus externus

Table 1.1. Complete list of transgenic mouse lines

Reference Name(s)	Locus (founder or line)	Transgene	Cell Type Targeted	Citation
Cell Type Driver Lines (type)				
D1-Cre or D1R-Cre (BAC)	Dopamine 1a receptor (EY262)	Cre	dSPNs	GENSAT Gong et al. 2003 ¹
D2-Cre or D2R-Cre (BAC)	Dopamine 2 receptor (ER43)	Cre	ISPNS	GENSAT Gong et al. 2003 ¹
D2-GFP or D2R-GFP (BAC)	Dopamine 2 receptor (S118)	EGFP	ISPNS	GENSAT Gong et al. 2003 ¹
GAD67-GFP (CDS Knock-In)	GAD67	GFP	GAD67+ cells in cortex and GP	Tamamaki et al. 2003 ²
ChAT-GFP (BAC)	Choline acetyltransferase	GFP	ChAT+ cells in GP, NB, and Cortex	Tallini et al. 2006 ³
Rbp4-Cre (BAC)	Retinol binding protein 4 (KL100)	Cre	Cortical-striatal deep layer pyramids	GENSAT Gerfen et al. 2013
Adora2a-Cre, A2AR-Cre (BAC)	Adenosine A2a receptor (KG139)	Cre	ISPNS	GENSAT Gong et al. 2007 ⁴
PV-Cre, PV-i-Cre (IRES Knock-In)	Parvalbumin	Cre	PV+ cells in GP and Cortex	Hippenmeyer et al. 2005 ⁵
ChAT-i-Cre (IRES Knock-In)	Choline acetyltransferase	Cre	ChAT+ cells in GP, NB, and Cortex	Rossi et al. 2011 ⁶
GAD2-i-Cre (IRES Knock-In)	GAD2/GAD65	Cre	GAD65+ cells in the GP and NB	Taniguchi et al. 2011 ⁷
Floxed Alleles				
Vgat (<i>Slc32a1</i>)	Vesicular GABA transporter			Tong et al. 2008 ⁸
Cre Reporter Lines				
Isl-tdTomato	Rosa26 (Ai14)	TdTomato		Madisen et al. 2010 ⁹
Isl-zsGreen	Rosa26 (Ai6)	ZsGreen		Madisen et al. 2010 ⁹
Isl-ChR2-YFP	Rosa (Ai32)	ChR2H134R-YFP		Madisen et al. 2012 ¹⁰

Table 1.2. Complete list of recombinant adeno-associated viruses

Reference Name	Promoter	Vector Name	Serotype	Titer (virus molecules / ml)	Citation
DIO-ChR2-mCherry	EF1 α	rAAV-DIO-hChr2(H134R)-mCherry-WPRE-pA	8	8 x 10 ¹²	Atasoy et al. 2008 ¹¹
DIO-mCherry	EF1 α	rAAV-DIO-mCherry-WPRE-pA	8	6 x 10 ¹²	Saunders, Johnson and Sabatini, 2013 ¹²
DIO-GFP	EF1 α	rAAV-DIO-EGFP-WPRE-pA	8	4 x 10 ¹²	Saunders, Johnson and Sabatini, 2013 ¹²
DIO-ChETA-tdTomato	EF1 α	rAAV-DIO-ChETA-tdTomato-WPRE-pA	8	1 x 10 ¹²	Saunders, Johnson and Sabatini, 2013 ¹²
DIO-ChETA-YFP	EF1 α	rAAV-DIO-ChETA-tdTomato-WPRE-pA	8	6 x 10 ¹²	Saunders, Johnson and Sabatini, 2013 ¹²
DIO-ArchT-tdTomato	CAG	rAAV-DIO-ArchT-tdTomato-WPRE-pA	5	6 x 10 ¹²	Han et al. 2011 ¹³
DIO-hM4D-mCherry	hSynapsin	AAV-DIO-hM4D-WPRE-pA	8	1.6 x 10 ¹³	Krashes et al. 2011 ¹⁴
DIO-GFP_DO-tdTomato	EF1 α	rAAV-DIO-EGFP_DO-tdTomato-WPRE-pA	8	2 x 10 ¹²	Saunders, Johnson and Sabatini, 2013 ¹²
DIO-VGAT	EF1 α	AAV-DIO-VGAT-WPRE-pA	8	3 x 10 ¹²	Tritsch, Ding and Sabatini, 2012
DO-ChR2-mCherry	EF1 α	rAAV-DO-hChr2(H134R)-mCherry-WPRE-pA	8	3x 10 ¹²	Saunders, Johnson and Sabatini, 2013 ¹²
DO-mCherry	EF1 α	rAAV-mCherry-WPRE-pA	8	5.7 x 10 ¹²	Saunders, Johnson and Sabatini, 2013 ¹²
DO-GFP	EF1 α	rAAV-DO-EGFP-WPRE-pA	8	4 x 10 ¹²	Saunders, Johnson and Sabatini, 2013 ¹²
DO-ChETA-YFP	EF1 α	rAAV-DIO-ChETA-YFP-WPRE-pA	8	6 x 10 ¹²	Saunders, Johnson and Sabatini, 2013 ¹²
DIO-NpHR3.0-YFP	EF1 α	rAAV-DIO-NpHR3.0-YFP-WPRE-pA	5	4 x 10 ¹²	Gradinaru, Thompson and Deisseroth, 2008 ¹⁵
FAS-tdTomato	EF1 α	rAAV-FAS-tdTomato-WPRE-pA	8	8 x 10 ¹²	Saunders, Johnson and Sabatini, 2013 ¹²
FAS-GFP	EF1 α	rAAV-FAS-EGFP-WPRE-pA	8	4 x 10 ¹²	Saunders, Johnson and Sabatini, 2013 ¹²
FAS-ChR2-mCherry	EF1 α	rAAV-FAS-hChr2(H134R)-mCherry-WPRE-pA	8	8 x 10 ¹²	Saunders, Johnson and Sabatini, 2013 ¹²
FAS-ChETA-tdTomato	EF1 α	rAAV-FAS-ChETA-tdTomato-WPRE-pA	8	1 x 10 ¹²	Saunders, Johnson and Sabatini, 2013 ¹²
FAS-NpHR3.0-YFP	EF1 α	rAAV-FAS-NpHR3.0-YFP-WPRE-pA	8	2 x 10 ¹²	Saunders, Johnson and Sabatini, 2013 ¹²
Cre-mCherry	CAG	rAAV-AM/CBA-mCherry-Cre-WPRE-BGH	1	1.2 x 10 ¹³	Lu et al. 2009 ¹⁶
Cre-GFP	CAG	rAAV-AM/CBA-EGFP-Cre-WPRE-BGH	1	8 x 10 ¹²	Lu et al. 2009 ¹⁶

(GP) and determine how activity in these cell types affect circuit function of the basal ganglia and cortex during adulthood.

The direct and indirect pathway model of the basal ganglia-cortex interactions

All animals must adapt their behaviors to changing environments to survive. Behavioral adaptation requires new thought and motor programs to be conceived, enacted and their outcomes evaluated. In humans, this process helps build the behaviors that constitute our make-up: on the timescale of seconds, our choices and reactions; and on longer timescales, our habits. This remarkable plasticity is a product of brain cell biology and the circuit architecture in which these brain cells reside.

Lesion studies in humans and growing experimental work in animals suggest the cerebral cortex generates behavioral programs, while the subcortical basal ganglia (BG) - a collection of highly interconnected forebrain nuclei - are responsible for evaluation. Enaction, however, depends on both the cortex and BG. This cooperativity is thought to arise because of closed-loop architecture: the cortex feeds into the BG while the BG feed back onto the cortex via the thalamus. This cortex-BG-thalamus loop is the accepted neural substrate for behavioral adaptations such as reinforcement learning^{17,18} and much anatomical work has built a working – albeit highly oversimplified – circuit model for how this process take place.

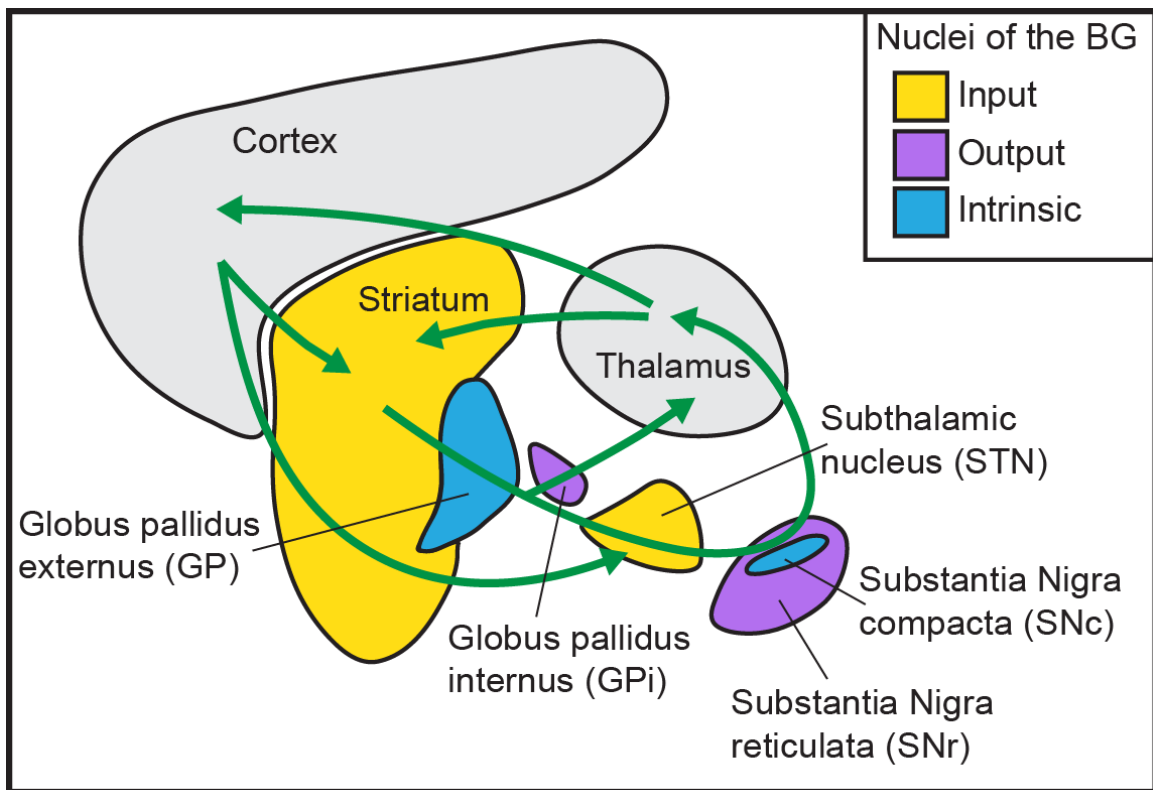
The basal ganglia consist of two input nuclei, two output nuclei and two nuclei that are intrinsic (Figure 1.1). The major input nucleus is the striatum. Dorsal striatum

Figure 1.1 Anatomical schematic depicting accepted position of BG nuclei within the cortex-BG-thalamus loop.

The accepted neural pathways that make up the loop are illustrated with green arrows.

Cortical inputs enter into the BG through the striatum or subthalamic nucleus. BG output nuclei target the thalamus. Thalamic nuclei can directly feed back into the BG via the striatum or indirectly via the cortex.

Figure 1.1 (Continued)



receives topographic glutamatergic input from the motor, sensory and associative areas of the cerebral cortex, as well as the thalamus, hippocampus and amygdala. The ventral striatum receives glutamatergic input from prefrontal and limbic cortices, thalamus, and amygdala¹⁹. The minor input nucleus is the subthalamic nucleus (STN), which receives glutamatergic input from the frontal cortex²⁰. The two output nuclei are the globus pallidus internus (GPi) (called the entopeduncular nucleus in rodents and much reduced in size) and the substantia nigra reticulata (SNr). The GPi and SNr provide tonic GABAergic inhibition to the thalamus, while the SNr projects additionally to the brainstem²¹. BG inhibition to thalamus directly and indirectly affects striatal-projecting and cortical-projecting glutamatergic thalamic nuclei²². Thalamo-cortical nuclei innervate multiple cortical areas²³, some of which have distinct axonal distributions across layers^{24,25}, suggesting BG feedback may differ by cortical area. The intrinsic BG nuclei are the globus pallidus externus (GP), which provides tonic GABAergic inhibition to the STN and SNr²⁶ and the substantia nigra compacta (SNc) and ventral tegmental area (VTA), which provide a large dopaminergic projection to the dorsal and ventral striatum respectively²⁷.

The long-standing direct and indirect pathway model provides a simplified circuit framework for understanding how the internal architecture of the BG affects activity within the cortex-BG-thalamic loop. The model posits that activity in two different types of spatially intermingled and equally abundant striatal GABAergic projection neurons results in opposite effects on BG output^{28,29}. The direct and indirect pathway spiny projection neurons (dSPNs/dMSNs and iSPNs/iMSNs) are distinguished by dopamine

receptor expression³⁰, expressed neuropeptides³¹, intrinsic excitability³² and most importantly, axonal projection patterns³³. dSPNs directly (monosynaptically) inhibit the output nuclei and the SNc, while iSPNs disinhibit the firing of the SNr and GPi via the GP (Figure 1.2a). The model suggests the net effect of dSPN activity is to promote cortical activity and drive behavior, while iSPN activity dampens cortical activity and inhibits behavior. Because both dSPNs and iSPNs receive topographic glutamatergic inputs from cortex³⁴, it has been theorized that groups of neighboring dSPNs and iSPNs act synergistically to select and terminate a given behavior or select a behavior and repress other unwanted behaviors^{35,36}.

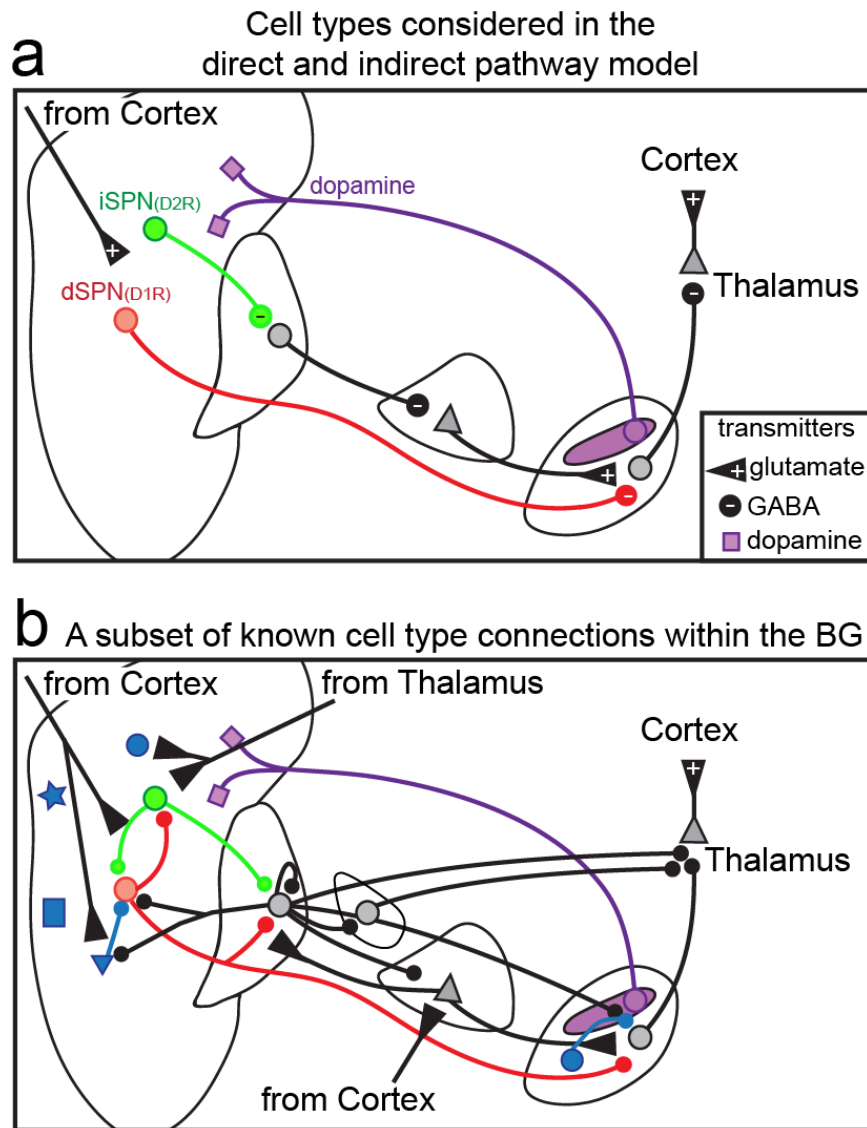
The model also posits that this push-pull synaptic organization is also engaged by behavioral outcome-dependent release of neuromodulator dopamine. dSPNs express $G_{\alpha_{olf/s}}$ coupled dopamine 1 receptors (D1Rs) which drive PKA activation and increase intrinsic excitability by regulating voltage dependent calcium channels and potentiating glutamatergic signaling. iSPNs express $G_{\alpha_{i/o}}$ coupled dopamine 2 receptors (D2Rs) which inhibit PKA (via G_{α_i}) and further decreasing excitability via voltage dependent calcium, sodium and potassium channels (via $G_{\beta\delta}$) and dampen glutamatergic signaling^{37,38}. Dopamine is thus thought to promote cortical activation by increasing dSPN activity and reducing iSPN activity. Since many diseases of the BG result in either hyperkinetic or hypokinetic movement disorders, the pathway model suggests the underlying pathologies could result from imbalances in dSPN vs. iSPN activity²⁸.

Figure 1.2. Cell type based synaptic connectivity within the BG.

a. The major cell types and synaptic connections considered in the direct and indirect pathway model of BG function. According to the model²⁸, direct pathway dSPNs directly inhibit tonically active BG output neurons via synaptic GABA release. Indirect pathway iSPNs indirectly activate BG output neurons by disinhibiting excitatory glutamatergic inputs from STN projection neurons. Dopaminergic feedback into striatum from SNc projection neurons excites dSPNs and inhibits iSPNs via D1R or D2R signaling respectively. The model predicts that dSPN activity should activate cortex while iSPN activity should inhibit cortex and dopamine should potentiate this functional antagonism.

b. An anatomically accurate depiction of a sub-set of known cell type connections within the BG that complicate the predictions of the direct and indirect pathway model. In striatum, dSPNs and iSPNs reciprocally inhibit each other and are innervated by a handful of functionally distinct classes of local interneurons (shown in blue). Moreover, both iSPNs and dSPNs project to the GP. GP neurons target all nuclei of the BG, making reciprocal synaptic loops with the striatum and the STN. GP neurons also project to thalamus. The cell types within the SNr and GPi are incompletely understood. Within the SNr, GABAergic neurons inhibit dopaminergic of the SNc in addition to the thalamus.

Figure 1.2 (Continued)



Indeed, Parkinsonian patients who lack dopamine tend to be hypokinetic and the nuclei controlled by the putatively dampened iSPNs (the GP and STN) exhibit pathological oscillations which are a hallmark of the disease³⁹.

Technical breakthroughs allowing genetically defined cell types to be manipulated by light⁴⁰, designer drugs^{41,42}, or selective toxins⁴³ have allowed the direct and indirect pathway model to be tested directly. As predicted by the model, optogenetic activation of dSPNs from dorsomedial striatum inhibits activity in the SNr and increases movement, while iSPN activation inhibits GP activity and decreases movement⁴⁴. Similar manipulations also lead to the predicted increases or decreases in activity in primary motor cortex⁴⁵. The functional opposition of dSPN and iSPN activity has also been extended to susceptibility of drugs of abuse, a well-studied type of habit formation that involves BG circuits^{17,46}. In both dorsal striatum⁴⁷ and ventral striatum⁴⁸, dampening dSPNs reduced the behavioral responses to drugs that increase dopamine signaling, while dampening iSPNs potentiated these responses.

Experiments monitoring dSPN and iSPN activity during behavior compliment large-scale gain or loss of function studies to refine our understanding of how both pathways are recruited to enact behaviors. In mice performing an operant task, both dSPN and iSPN activity preceded lever pressing, suggesting activity in both cell types are involved in initiating a motor sequence⁴⁹. Consistent with these results, in learned sequences of actions, individual dSPNs and iSPNs can discharge at the beginning, end or throughout the motor sequence. Interestingly, the proportions SPNs active during each stage of a sequence differs by pathway and these differences change during learning⁵⁰.

These manipulation and monitoring experiments suggest that dSPNs and iSPNs have opponent effects on basal ganglia activity, motor behavior and habit formation, but concomitant activity in both pathways is required for the learning or enacting behavior.

The explanatory power of the direct and indirect pathway model is almost miraculous when the simplified circuitry the model was based on (Figure 1.2a) is compared to the described anatomical complexity within the BG (Figure 1.2b). Some of these non-canonical features directly confound the classic model and may thus contribute to non-orthogonal function attributed to dSPNs and iSPNs^{51,52}. For example, dSPNs innervate the GP in addition to iSPNs^{33,53}. Additionally, GP neurons project widely throughout the BG⁵⁴, including into the striatum^{55,56}. Thus SPNs can feedback onto striatum through a single GP synapse, rather than the approximate 6 synapses predicted by the pathway model and the cortex-BG-thalamus loop. A complete understanding of BG circuits underlying behavior and disease necessitates incorporating these non-canonical circuit elements; a challenge heightened by the rich anatomical literature often overlooked by the field. Transgenic animals and viral reagents offer a chance to extend these anatomical observations in functional manipulations following the Experimental Framework outlined above.

The role of neural activity in developmental wiring

The structure of adult brain circuits arises from an interaction of genetic programs and neural activity. The role activity plays in shaping circuit structure is especially pronounced during post-natal development, when animals are first exposed

and must adapt to their external world. Our understanding of this process has been most informed by the sensory systems. Sensory epithelia can be lesioned and inputs controlled experimentally, allowing the resulting abnormalities in circuit structure to be studied. In contrast, little is known about how post-natal activity affects and is organized by the circuits in the central brain. This gap in knowledge has been due in large part to a lack of tools for cell type specific molecular lesions that affect neurotransmitter release.

The early visual system has provided a powerful model system for understanding how activity within a feed-forward, excitatory circuit refines synaptic development. Two prominent features of this circuit are profoundly activity dependent. Retinotopy, by which visual areas are endowed a map of visual space, is refined by spontaneous waves of activity generated in the retina before eye opening^{57,58}. Feed-forward glutamatergic synapses from the retina to the lateral geniculate nucleus (LGN) and from the LGN to primary visual cortex (V1) maintain the spatial co-activation of neighboring neurons that are strengthened through Hebbian mechanisms of long-term potentiation^{59,60}. The second is binocularity, where eye-specific activity contributes to the segregation, pruning and strengthening of retinogeniculate synapses⁶¹⁻⁶³ and to the response properties of V1 neurons⁶⁴⁻⁶⁶. Screening for genes involved in these striking refinements has led to the identification of many important signaling pathways engaged by activity to drive structural changes in synaptic organization⁶⁷⁻⁷¹.

Given their role in sculpting behavioral repertoire, the BG would be predicted to undergo dynamic changes as animals become independent. Indeed in songbirds, neural activity within the anterior forebrain pathway – the equivalent circuit to the BG in

mammals⁷² – is necessary for song learning during post-natal development^{73,74}. In adult birds, the AFP encodes the discrepancy between the perceived and target song, an instructional signal used to guide song modification⁷⁵. AFP activity likely plays a similar role in sensory-motor learning during development⁷⁶. Despite this behavioral relevance, how activity modifies or is sculpted by the underlying circuit architecture is unknown. Mammalian BG neurons are mostly GABAergic and recurrently connected, suggesting the principles of how activity controls synaptogenesis within BG and across the BG-thalamo-cortical circuit may be different from those of the early visual system.

Dopamine 2 receptor drugs and the circuitry of the globus pallidus externus

Anti-psychotic drugs used to treat the hallucinations and delusions of schizophrenia⁷⁷ and symptoms of other psychiatric disorders such as bipolar⁷⁸ and obsessive compulsive disorder⁷⁹ all antagonize D2Rs (Figure 1.3a)⁸⁰. This pharmacology is a cornerstone of the hypothesis that hyperactive dopamine signaling may contribute to schizophrenia^{81,82} and suggests a privileged role of D2R expressing cells in etiology and treatment of these psychiatric diseases. iSPNs are the most abundant class of D2R expressing neurons in the brain and, as predicted, the striatum is the major site of anti-psychotic binding⁸³ (Figure 1.3b). Since iSPNs exclusively innervate the GP and ventral pallidum (VP) (Figure 1.3c), the therapeutic effects of anti-psychotic drugs are likely mediated through GP/VP circuits. Indeed, GP lesions produce psychiatric symptoms in

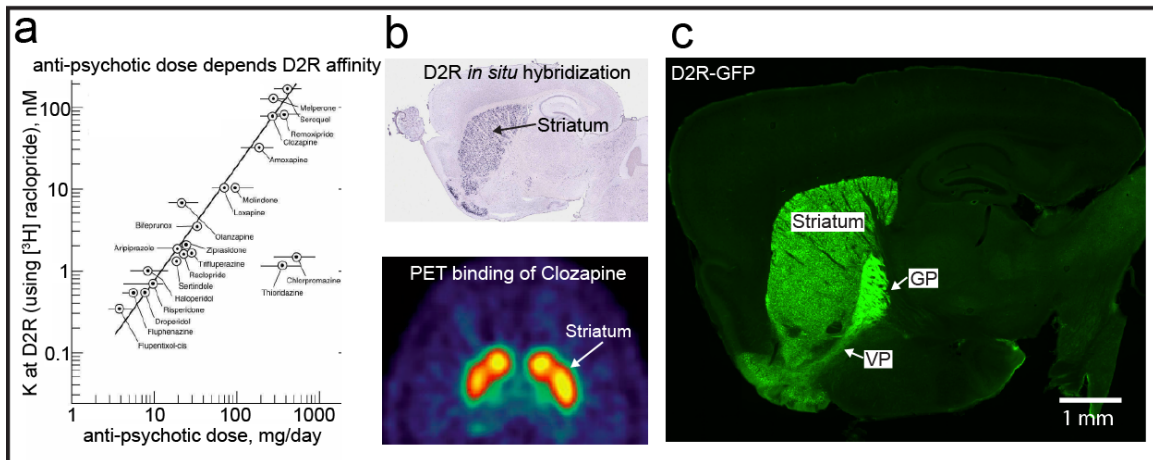
Figure 1.3. Anti-psychotic drugs target D2Rs in the striatum and implicate iSPNs and GP cell types in their mechanism of action.

a. Competitive binding assays of different anti-psychotic drugs demonstrate a striking linear relationship between D2R affinity and daily dose necessary to relieve symptoms (adapted from http://www.scholarpedia.org/article/Dopamine_and_schizophrenia).

b. The striatum has the highest levels of D2R expression and is the major location of anti-psychotic binding. *Top, in situ* hybridization on a sagittal section of mouse brain showing high levels of D2R mRNA expressed in the striatum (Allen Institute). *Bottom,* positron emission tomography image from a horizontal section of human brain showing reduced occupancy of striatal D2/3Rs after treatment with the anti-psychotic Clozapine⁸³.

c. Sagittal section from a BAC transgenic mouse where GFP is driven by D2R regulatory elements (D2R-GFP). Striatal iSPNs are the most abundant D2R expressing cell type in the brain and project exclusively to the GP and VP.

Figure 1.3 (Continued)



humans⁸⁴ and mice carrying mutations in cortico-striatal synapses⁸⁵ or overexpressing D2Rs in the striatum⁸⁶ exhibit analogous behavioral impairments.

While anti-psychotics target the striatum, converging evidence suggests alterations in prefrontal cortex (PFC) circuits are associated with schizophrenia. Disease onset occurs most often in late adolescence, a period associated with excitatory synaptic pruning⁸⁷ and inhibitory synaptic proliferation⁸⁸ in the PFC. Post-mortem analyses of the PFC have identified disease-associated changes in neural architecture and gene expression⁸⁹. These include pronounced deficits in dendritic spine morphology^{90,91} and reductions in GABA signaling in subsets of cortical interneurons⁹²⁻⁹⁴. Global analyses agnostic to cell type further suggest that genes involved in presynaptic release⁹⁵ and the neurotransmission of GABA^{96,97}, glutamate^{98,99} and acetylcholine¹⁰⁰ are also misregulated.

Importantly, anti-psychotics do not treat the cognitive and depressive symptoms which precede and persist through psychosis. This selectivity suggests these sets of symptoms arise from at least partially distinct neural substrates. To date, only the cognitive symptoms have been preliminary linked to PFC pathology¹⁰¹. Nevertheless, treating healthy rodents with anti-psychotics is sufficient to drive the opposite changes in genes that participate in disease-implicated pathways in frontal cortex^{102,103}. This suggests that subcortical D2Rs blockade by anti-psychotics induces therapeutic changes in frontal cortex, some of which may involve the same signaling molecules either directly or indirectly misregulated by the disease itself.

Despite 60 years of clinical use, the circuit mechanisms by which anti-psychotics target the striatum to affect frontal cortex are not understood. One limitation has been the dearth of knowledge concerning the cell types in the GP that iSPNs control. GP neurons tend to be GABAergic¹⁰⁴⁻¹⁰⁶, spontaneously active *in vitro*¹⁰⁷ and *in vivo*¹⁰⁸ and project throughout the BG, including the STN, GPi, SNr/SNc, and the striatum^{109,110}. GP neurons also project to the reticular^{111,112} and parafascicular¹¹³ nuclei of the thalamus. Thus the GP is thought to coordinate the timing of subcortical activity through inhibition^{26,114}. While the GP is one of the most transcriptionally distinctive regions of the human brain¹¹⁵, our understanding of how this molecular diversity maps onto distinct cell types is in its infancy.

Electrophysiological descriptions of GP neurons identified three distinct neuronal groups in acute slices^{116,117}. However this categorization must be interpreted with caution, as individual GP neurons can exhibit a large diversity of activity profiles¹¹⁸. The definition of GP cell types has been aided by correlating electrophysiological and anatomical properties with distinct molecular markers, including parvalbumin (PV), preproenkephalin (PPE) and the transcription factor Lhx6^{56,113,119}. PV⁺ GP neurons largely lack PPE and Lhx6 and tend to project STN, SNr, and reticular nucleus of the thalamus, while striatal-projecting GP neurons tend to express PPE⁺ and Lhx6⁺. Preliminary evidence from dopamine manipulations followed by anesthetized *in vivo* recordings¹²⁰ or gene expression assays¹²¹ suggest these two cell groups may be functionally distinct. Nevertheless these markers identify trends, not rules, in GP connectivity and no cell types have yet been linked to particular behaviors or circuit functions.

In many species including humans, neurons expressing choline acetyltransferase (ChAT) are present within and around the GP, especially concentrated at ventral and posterior borders¹²²⁻¹²⁵. These neurons have historically been considered the dorsal most extent of the nucleus Basalis, the tip of a nebulous, spiraling collection of neurons that project axons throughout the entire cortical mantle¹²⁶ and release the neurotransmitter acetylcholine. Anatomical work combining anterograde labeling with light and electron microscopy demonstrated that ChAT⁺ GP neurons did receive asymmetrical synaptic contacts from putative iSPNs of dorsal striatum^{127,128}. However, the relative sparseness of these synapses did not constitute the inclusion of ChAT⁺ cells into the BG circuits that process motor, sensory and cognitive. Instead, these cells have been functionally grouped with other ChAT⁺ cells of the basal forebrain cholinergic system, which confer limbic information to cortex¹²⁹, including attentional state^{130,131}, and have important roles in the synaptic plasticity of cortical circuits¹³²⁻¹³⁴.

References

1. Gong, S. *et al.* A gene expression atlas of the central nervous system based on bacterial artificial chromosomes. *Nature* **425**, 917–925 (2003).
2. Tamamaki, N. *et al.* Green fluorescent protein expression and colocalization with calretinin, parvalbumin, and somatostatin in the GAD67-GFP knock-in mouse. *J Comp Neurol* **467**, 60–79 (2003).
3. Tallini, Y. N. *et al.* BAC transgenic mice express enhanced green fluorescent protein in central and peripheral cholinergic neurons. *Phys Genomics* **27**, 391–397 (2006).

4. Gong, S. *et al.* Targeting Cre Recombinase to Specific Neuron Populations with Bacterial Artificial Chromosome Constructs. *J Neurosci* **27**, 9817–9823 (2007).
5. Hippenmeyer, S. *et al.* A Developmental Switch in the Response of DRG Neurons to ETS Transcription Factor Signaling. *Plos Biol* **3**, e159 (2005).
6. Rossi, J. *et al.* Melanocortin-4 Receptors Expressed by Cholinergic Neurons Regulate Energy Balance and Glucose Homeostasis. *Cell Metab* **13**, 195–204 (2011).
7. Taniguchi, H. *et al.* A Resource of Cre Driver Lines for Genetic Targeting of GABAergic Neurons in Cerebral Cortex. *Neuron* **71**, 995–1013 (2011).
8. Tong, Q., Ye, C.-P., Jones, J. E., Elmquist, J. K. & Lowell, B. B. Synaptic release of GABA by AgRP neurons is required for normal regulation of energy balance. *Nat Neuro* **11**, 998–1000 (2008).
9. Madisen, L. *et al.* A robust and high-throughput Cre reporting and characterization system for the whole mouse brain. *Nat Neuro* **13**, 133–140 (2010).
10. Madisen, L. *et al.* A toolbox of Cre-dependent optogenetic transgenic mice for light-induced activation and silencing. *Nat Neuro* 1–12 (2012). doi:10.1038/nn.3078
11. Atasoy, D., Aponte, Y., Su, H. H. & Sternson, S. M. A FLEX switch targets Channelrhodopsin-2 to multiple cell types for imaging and long-range circuit mapping. *J Neurosci* **28**, 7025–7030 (2008).
12. Saunders, A., Johnson, C. A. & Sabatini, B. L. Novel recombinant adeno-associated viruses for Cre activated and inactivated transgene expression in neurons. *Front Neural Circuits* **6**, 47 (2012).
13. Han, X. *et al.* A High-Light Sensitivity Optical Neural Silencer: Development and Application to Optogenetic Control of Non-Human Primate Cortex. *Front. Syst. Neurosci.* **5**, (2011).
14. Krashes, M. J. *et al.* Rapid, reversible activation of AgRP neurons drives feeding behavior in mice. *J. Clin. Invest.* **121**, 1424–1428 (2011).
15. Gradinaru, V., Thompson, K. R. & Deisseroth, K. eNpHR: a Natronomonas halorhodopsin enhanced for optogenetic applications. *Brain Cell Biol* **36**, 129–139 (2008).

16. Lu, W. *et al.* Subunit Composition of Synaptic AMPA Receptors Revealed by a Single-Cell Genetic Approach. *Neuron* **62**, 254–268 (2009).
17. Yin, H. H. & Knowlton, B. J. The role of the basal ganglia in habit formation. *Nat Rev Neurosci* **7**, 464–476 (2006).
18. Fee, M. S. & Goldberg, J. H. A hypothesis for basal ganglia-dependent reinforcement learning in the songbird. *Neuroscience* **198**, 152–170 (2011).
19. Groenewegen, H. J., Wright, C. I., Beijer, A. V. & Voorn, P. Convergence and segregation of ventral striatal inputs and outputs. *Ann N Y Acad Sci* **877**, 49–63 (1999).
20. Nambu, A. *et al.* Excitatory cortical inputs to pallidal neurons via the subthalamic nucleus in the monkey. *J Neurophysiol* **84**, 289–300 (2000).
21. Inglis, W. L. & Winn, P. The pedunculo-pontine tegmental nucleus: where the striatum meets the reticular formation. *Prog Neurobiol* **47**, 1–29 (1995).
22. McFarland, N. R. & Haber, S. N. Thalamic relay nuclei of the basal ganglia form both reciprocal and nonreciprocal cortical connections, linking multiple frontal cortical areas. *J Neurosci* **22**, 8117–8132 (2002).
23. Cappe, C., Morel, A., Barone, P. & Rouiller, E. M. The Thalamocortical Projection Systems in Primate: An Anatomical Support for Multisensory and Sensorimotor Interplay. *Cerebral Cortex* **19**, 2025–2037 (2009).
24. Rubio-Garrido, P., Perez-De-Manzo, F., Porrero, C., Galazo, M. J. & Clasca, F. Thalamic Input to Distal Apical Dendrites in Neocortical Layer 1 Is Massive and Highly Convergent. *Cerebral Cortex* **19**, 2380–2395 (2009).
25. Wimmer, V. C., Bruno, R. M., de Kock, C. P. J., Kuner, T. & Sakmann, B. Dimensions of a Projection Column and Architecture of VPM and POM Axons in Rat Vibrissal Cortex. *Cerebral Cortex* **20**, 2265–2276 (2010).
26. Kita, H. Globus pallidus external segment. *Prog Brain Res* **160**, 111–133 (2007).
27. in *Dopamine Handbook* (Iversen, L. L., Iversen, S. D., Dunnett, S. B. & Björklund, A.) (Oxford Univ Press 2XXX).
28. Albin, R. L., Young, A. B. & Penney, J. B. The functional anatomy of basal ganglia disorders. *Trends Neurosci* **12**, 366–375 (1989).

29. Smith, Y., Bevan, M. D., Shink, E. & Bolam, J. P. Microcircuitry of the direct and indirect pathways of the basal ganglia. *Neuroscience* **86**, 353–387 (1998).
30. Gerfen, C. R. The neostriatal mosaic: multiple levels of compartmental organization. *Trends Neurosci* **15**, 133–139 (1992).
31. Steiner, H. & Gerfen, C. R. Role of dynorphin and enkephalin in the regulation of striatal output pathways and behavior. *Exp Brain Res* **123**, 60–76 (1998).
32. Gertler, T. S., Chan, C. S. & Surmeier, D. J. Dichotomous Anatomical Properties of Adult Striatal Medium Spiny Neurons. *J Neurosci* **28**, 10814–10824 (2008).
33. Chang, H. T., Wilson, C. J. & Kitai, S. T. Single neostriatal efferent axons in the globus pallidus: a light and electron microscopic study. *Science* **213**, 915–918 (1981).
34. Parent, A. & Hazrati, L.-N. Functional anatomy of the basal ganglia. I. The cortico-basal ganglia-thalamo-cortical loop. *Brain Res Rev* **20**, 91–127 (1995).
35. Mink, J. W. & Thach, W. T. Basal ganglia intrinsic circuits and their role in behavior. *Curr Opin Neurobiol* **3**, 950–957 (1993).
36. Mink, J. W. The basal ganglia: focused selection and inhibition of competing motor programs. *Prog Neurobiol* **50**, 381–425 (1996).
37. Surmeier, D. J., Ding, J., Day, M., Wang, Z. & Shen, W. D1 and D2 dopamine-receptor modulation of striatal glutamatergic signaling in striatal medium spiny neurons. *Trends Neurosci* **30**, 228–235 (2007).
38. Tritsch, N. X. & Sabatini, B. L. Dopaminergic Modulation of Synaptic Transmission in Cortex and Striatum. *Neuron* **76**, 33–50 (2012).
39. Galvan, A. & Wichmann, T. GABAergic circuits in the basal ganglia and movement disorders. *Prog Brain Res* **160**, 287–312 (2007).
40. Zhang, F., Wang, L.-P., Boyden, E. S. & Deisseroth, K. Channelrhodopsin-2 and optical control of excitable cells. *Nat Methods* **3**, 785–792 (2006).

41. Conklin, B. R. *et al.* Engineering GPCR signaling pathways with RASSLs. *Nat Methods* **5**, 673–678 (2008).
42. Rogan, S. C. & Roth, B. L. Remote Control of Neuronal Signaling. *Pharmacological Reviews* **63**, 291–315 (2011).
43. Buch, T. *et al.* A Cre-inducible diphtheria toxin receptor mediates cell lineage ablation after toxin administration. *Nat Methods* **2**, 419–426 (2005).
44. Kravitz, A. V. *et al.* Regulation of parkinsonian motor behaviours by optogenetic control of basal ganglia circuitry. *Nature* **466**, 622–626 (2010).
45. Oldenburg, I. A. & Sabatini, B. L. Antagonistic but not opposite regulation of primary motor cortex by basal ganglia direct and indirect pathways. *In Preparation*
46. Thomas, M. J. & Malenka, R. C. Synaptic plasticity in the mesolimbic dopamine system. *Philos Trans R Soc Lond, B, Biol Sci* **358**, 815–819 (2003).
47. Ferguson, S. M. *et al.* Transient neuronal inhibition reveals opposing roles of indirect and direct pathways in sensitization. *Nat Neuroscience* **14**, 22–24 (2010).
48. Lobo, M. K. *et al.* Cell Type-Specific Loss of BDNF Signaling Mimics Optogenetic Control of Cocaine Reward. *Science* **330**, 385–390 (2010).
49. Cui, G. *et al.* Concurrent activation of striatal direct and indirect pathways during action initiation. *Nature* **494**, 238–242 (2014).
50. Jin, X., Tecuapetla, F. & Costa, R. M. Basal ganglia subcircuits distinctively encode the parsing and concatenation of action sequences. *Nat Neuro* (2013).
51. Freeze, B. S., Kravitz, A. V., Hammack, N., Berke, J. D. & Kreitzer, A. C. Control of Basal Ganglia Output by Direct and Indirect Pathway Projection Neurons. *J Neurosci* **33**, 18531–18539 (2013).
52. Hikida, T., Kimura, K., Wada, N., Funabiki, K. & Nakanishi, S. Distinct Roles of Synaptic Transmission in Direct and Indirect Striatal Pathways to Reward and Aversive Behavior. *Neuron* **66**, 896–907 (2010).
53. Cazorla, M. *et al.* Dopamine D2 Receptors Regulate the Anatomical and Functional Balance of Basal Ganglia Circuitry. *Neuron* **81**, 153–164 (2014).

54. Bevan, M. D., Booth, P. A., Eaton, S. A. & Bolam, J. P. Selective innervation of neostriatal interneurons by a subclass of neuron in the globus pallidus of the rat. *J Neurosci* **18**, 9438–9452 (1998).
55. Jayaraman, A. Topographic organization and morphology of peripallidal and pallidal cells projecting to the striatum in cats. *Brain Res* **275**, 279–286 (1983).
56. Kita, H. & Kita, T. Number, origins, and chemical types of rat pallidostriatal projection neurons. *J Comp Neurol* **437**, 438–448 (2001).
57. Meister, M., Wong, R. O., Baylor, D. A. & Shatz, C. J. Synchronous bursts of action potentials in ganglion cells of the developing mammalian retina. *Science* **252**, 939–943 (1991).
58. Schmidt, J. T. Formation of retinotopic connections: selective stabilization by an activity-dependent mechanism. *Cell Mol Neurobiol* **5**, 65–84 (1985).
59. Mooney, R., Madison, D. V. & Shatz, C. J. Enhancement of transmission at the developing retinogeniculate synapse. *Neuron* **10**, 815–825 (1993).
60. Butts, D. A., Kanold, P. O. & Shatz, C. J. A Burst-Based ‘Hebbian’ Learning Rule at Retinogeniculate Synapses Links Retinal Waves to Activity-Dependent Refinement. *Plos Biol* **5**, e61 (2007).
61. Shatz, C. J. & Stryker, M. P. Prenatal tetrodotoxin infusion blocks segregation of retinogeniculate afferents. *Science* **242**, 87–89 (1988).
62. Stellwagen, D. & Shatz, C. J. An instructive role for retinal waves in the development of retinogeniculate connectivity. *Neuron* **33**, 357–367 (2002).
63. Chen, C. & Regehr, W. G. Developmental remodeling of the retinogeniculate synapse. *Neuron* **28**, 955–966 (2000).
64. Wiesel, T. N. & Hubel, D. H. Single-cell responses in striate cortex of kittens deprived of vision in one eye. *J Neurophysiol* **26**, 1003–1017 (1963).
65. Antonini, A. & Stryker, M. P. Rapid remodeling of axonal arbors in the visual cortex. *Science* **260**, 1819–1821 (1993).
66. Katz, L. C. & Shatz, C. J. Synaptic activity and the construction of cortical

circuits. *Science* **274**, 1133–1138 (1996).

67. Corriveau, R. A., Huh, G. S. & Shatz, C. J. Regulation of class I MHC gene expression in the developing and mature CNS by neural activity. *Neuron* **21**, 505–520 (1998).
68. Stevens, B. *et al.* The Classical Complement Cascade Mediates CNS Synapse Elimination. *Cell* **131**, 1164–1178 (2007).
69. Sugiyama, S. *et al.* Experience-Dependent Transfer of Otx2 Homeoprotein into the Visual Cortex Activates Postnatal Plasticity. *Cell* **134**, 508–520 (2008).
70. Fagiolini, M. *et al.* Specific GABAA circuits for visual cortical plasticity. *Science* **303**, 1681–1683 (2004).
71. Datwani, A. *et al.* Classical MHCI Molecules Regulate Retinogeniculate Refinement and Limit Ocular Dominance Plasticity. *Neuron* **64**, 463–470 (2009).
72. Doupe, A. J., Perkel, D. J., Reiner, A. & Stern, E. A. Birdbrains could teach basal ganglia research a new song. *Trends Neurosci* **28**, 353–363 (2005).
73. Bottjer, S. W., Miesner, E. A. & Arnold, A. P. Forebrain lesions disrupt development but not maintenance of song in passerine birds. *Science* (1984).
74. Sohrabji, F., Nordeen, E. J. & Nordeen, K. W. Selective impairment of song learning following lesions of a forebrain nucleus in the juvenile zebra finch. *Behav. Neural Biol.* **53**, 51–63 (1990).
75. Brainard, M. S. & Doupe, A. J. Interruption of a basal ganglia-forebrain circuit prevents plasticity of learned vocalizations. *Nature* **404**, 762–766 (2000).
76. Brainard, M. S. Contributions of the anterior forebrain pathway to vocal plasticity. *Ann N Y Acad Sci* **1016**, 377–394 (2004).
77. Seeman, P. All Roads to Schizophrenia Lead to Dopamine Supersensitivity and Elevated Dopamine D2High Receptors. *CNS Neuroscience & Therapeutics* **17**, 118–132 (2011).

78. Tohen, M. & Vieta, E. Antipsychotic agents in the treatment of bipolar mania. *Bipolar Disord* **11**, 45–54 (2009).
79. Bloch, M. H. *et al.* A systematic review: antipsychotic augmentation with treatment refractory obsessive-compulsive disorder. *Mol Psychiatry* **11**, 622–632 (2006).
80. Kapur, S. & Mamo, D. Half a century of antipsychotics and still a central role for dopamine D2 receptors. *Prog. Neuropsychopharmacol. Biol. Psychiatry* **27**, 1081–1090 (2003).
81. Simpson, E. H., Kellendonk, C. & Kandel, E. A Possible Role for the Striatum in the Pathogenesis of the Cognitive Symptoms of Schizophrenia. *Neuron* **65**, 585–596 (2010).
82. Seeman, P. Dopamine receptors and the dopamine hypothesis of schizophrenia. *Synapse* **1**, 133–152 (2004).
83. Gründer, G., Hippus, H. & Carlsson, A. The ‘atypicality’ of antipsychotics: a concept re-examined and re-defined. *Nat Rev Drug Discov* **8**, 197–202 (2009).
84. Laplane, D. *et al.* Obsessive-compulsive and other behavioural changes with bilateral basal ganglia lesions. A neuropsychological, magnetic resonance imaging and positron tomography study. *Brain* **112 (Pt 3)**, 699–725 (1989).
85. Peca, J. *et al.* Shank3 mutant mice display autistic-like behaviours and striatal dysfunction. *Nature* **472**, 437–442 (2011).
86. Kellendonk, C. *et al.* Transient and Selective Overexpression of Dopamine D2 Receptors in the Striatum Causes Persistent Abnormalities in Prefrontal Cortex Functioning. *Neuron* **49**, 603–615 (2006).
87. Rakic, P., Bourgeois, J. P., Eckenhoff, M. F., Zecevic, N. & Goldman-Rakic, P. S. Concurrent overproduction of synapses in diverse regions of the primate cerebral cortex. *Science* **232**, 232–235 (1986).
88. Hashimoto, T. *et al.* Protracted Developmental Trajectories of GABA. *Biological Psychiatry* **65**, 1015–1023 (2009).
89. Insel, T. R. Rethinking schizophrenia. *Nature* **468**, 187–193 (2010).

90. Glantz, L. A. & Lewis, D. A. Decreased dendritic spine density on prefrontal cortical pyramidal neurons in schizophrenia. *Arch Gen Psychiatry* **57**, 65–73 (2000).
91. Glausier, J. R., Fish, K. N. & Lewis, D. A. Altered parvalbumin basket cell inputs in the dorsolateral prefrontal cortex of schizophrenia subjects. **19**, 30–36 (2013).
92. Woo, T., Whitehead, R. E., Melchitzky, D. S. & Lewis, D. A. A subclass of prefrontal γ -aminobutyric acid axon terminals are selectively altered in schizophrenia. *PNAS* **95**, 5341–5346 (1998).
93. Hashimoto, T. *et al.* Gene expression deficits in a subclass of GABA neurons in the prefrontal cortex of subjects with schizophrenia. *J Neurosci* **23**, 6315–6326 (2003).
94. Lewis, D. A., Hashimoto, T. & Volk, D. W. Cortical inhibitory neurons and schizophrenia. *Nat Rev Neurosci* **6**, 312–324 (2005).
95. Mirnics, K., Middleton, F. A., Marquez, A., Lewis, D. A. & Levitt, P. Molecular characterization of schizophrenia viewed by microarray analysis of gene expression in prefrontal cortex. *Neuron* **28**, 53–67 (2000).
96. Blum, B. P. & Mann, J. J. The GABAergic system in schizophrenia. *Int. J. Neuropsychopharma* **5**, 159–179 (2002).
97. Akbarian, S. & Huang, H. Molecular and cellular mechanisms of altered GAD1/GAD67 expression in schizophrenia and related disorders. *Brain Res Rev* **52**, 293–304 (2006).
98. Lewis, D. A., Glantz, L. A., Pierri, J. N. & Sweet, R. A. Altered cortical glutamate neurotransmission in schizophrenia. *Ann N Y Acad Sci* **1003**, 102–112 (2003).
99. Scarr, E., Beneyto, M., Meador-Woodruff, J. H. & Dean, B. Cortical Glutamatergic Markers in Schizophrenia. *Neuropsychopharmacology* **30**, 1521–1531 (2005).
100. Scarr, E., Gibbons, A. S., Neo, J., Udawela, M. & Dean, B. Cholinergic connectivity: it's implications for psychiatric disorders. *Front Cell Neurosci* **7**, 55 (2013).

101. Lewis, D. A. Inhibitory neurons in human cortical circuits: substrate for cognitive dysfunction in schizophrenia. *Curr Opin Neurobiol* **26**, 22–26 (2014).
102. MacDonald, M. L., Eaton, M. E., Dudman, J. T. & Konradi, C. Antipsychotic drugs elevate mRNA levels of presynaptic proteins in the frontal cortex of the rat. *Biological Psychiatry* **57**, 1041–1051 (2005).
103. Zink, M. *et al.* Differential Effects of Long-Term Treatment with Clozapine or Haloperidol on GABA Transporter Expression. *Pharmacopsychiatry* **37**, 171–174 (2004).
104. Smith, Y., Parent, A., Seguela, P. & Descarries, L. Distribution of GABA-immunoreactive neurons in the basal ganglia of the squirrel monkey (*Saimiri sciureus*). *J Comp Neurol* **259**, 50–64 (1987).
105. Sadek, A. R., Magill, P. J. & Bolam, J. P. A single-cell analysis of intrinsic connectivity in the rat globus pallidus. *J Neurosci* **27**, 6352–6362 (2007).
106. Falls, W. M., Park, M. R. & Kitai, S. T. An intracellular HRP study of the rat globus pallidus. II. Fine structural characteristics and synaptic connections of medially located large GP neurons. *J Comp Neurology* **221**, 229–245 (1983).
107. Chan, C. S. HCN2 and HCN1 Channels Govern the Regularity of Autonomous Pacemaking and Synaptic Resetting in Globus Pallidus Neurons. *J Neurosci* **24**, 9921–9932 (2004).
108. DeLong, M. R. Activity of pallidal neurons during movement. *J Neurophysiol* **34**, 414–427 (1971).
109. Sato, F., Lavallée, P., Lévesque, M. & Parent, A. Single-axon tracing study of neurons of the external segment of the globus pallidus in primate. *J Comp Neurology* **417**, 17–31 (2000).
110. Smith, Y. & Bolam, J. P. The output neurones and the dopaminergic neurones of the substantia nigra receive a GABA-containing input from the globus pallidus in the rat. *J Comp Neurol* **296**, 47–64 (1990).
111. Cornwall, J., Cooper, J. D. & Phillipson, O. T. Projections to the rostral reticular thalamic nucleus in the rat. *Exp Brain Res* **80**, 157–171 (1990).

112. Gasca-Martinez, D. *et al.* Dopamine inhibits GABA transmission from the globus pallidus to the thalamic reticular nucleus via presynaptic D4 receptors. *Neuroscience* **169**, 1672–1681 (2010).
113. Mastro, K. J., Bouchard, R. S., Holt, H. A. K. & Gittis, A. H. Transgenic Mouse Lines Subdivide External Segment of the Globus Pallidus (GPe) Neurons and Reveal Distinct GPe Output Pathways. *J Neurosci* **34**, 2087–2099 (2014).
114. Bevan, M. D., Magill, P. J., Terman, D., Bolam, J. P. & Wilson, C. J. Move to the rhythm: oscillations in the subthalamic nucleus-external globus pallidus network. *Trends Neurosci* **25**, 525–531 (2002).
115. Hawrylycz, M. J. *et al.* An anatomically comprehensive atlas of the adult human brain transcriptome. *Nature* **489**, 391–399 (2012).
116. Nambu, A. & Llinás, R. Electrophysiology of globus pallidus neurons in vitro. *J Neurophysiol* **72**, 1127–1139 (1994).
117. Cooper, A. J. & Stanford, I. M. Electrophysiological and morphological characteristics of three subtypes of rat globus pallidus neurone in vitro. *J Physiol (Lond)* **527 Pt 2**, 291–304 (2000).
118. Deister, C. A., Dodla, R., Barraza, D., Kita, H. & Wilson, C. J. Firing rate and pattern heterogeneity in the globus pallidus arise from a single neuronal population. *J Neurophysiol* **109**, 497–506 (2013).
119. Hoover, B. R. & Marshall, J. F. Population characteristics of preproenkephalin mRNA-containing neurons in the globus pallidus of the rat. *Neurosci Lett* **265**, 199–202 (1999).
120. Mallet, N. *et al.* Dichotomous Organization of the External Globus Pallidus. *Neuron* **74**, 1075–1086 (2012).
121. Hoover, B. R. & Marshall, J. F. Further characterization of preproenkephalin mRNA-containing cells in the rodent globus pallidus. *Neuroscience* **111**, 111–125 (2002).
122. Mesulam, M. M., Mufson, E. J., Levey, A. I. & Wainer, B. H. Cholinergic innervation of cortex by the basal forebrain: cytochemistry and cortical connections of the septal area, diagonal band nuclei, nucleus basalis (substantia innominata), and hypothalamus in the rhesus monkey. *J Comp Neurol* **214**, 170–197 (1983).

123. McKinney, M., Coyle, J. T. & Hedreen, J. C. Topographic analysis of the innervation of the rat neocortex and hippocampus by the basal forebrain cholinergic system. *J Comp Neurol* **217**, 103–121 (1983).
124. Saper, C. B. & Chelimsky, T. C. A cytoarchitectonic and histochemical study of nucleus basalis and associated cell groups in the normal human brain. *Neuroscience* **13**, 1023–1037 (1984).
125. Irle, E. & Markowitsch, H. J. Basal forebrain efferents reach the whole cerebral cortex of the cat. *Brain Res Bull* **12**, 493–512 (1984).
126. Zaborszky, L., Pang, K., Somogyi, J., Nadasdy, Z. & Kallo, I. The basal forebrain corticopetal system revisited. *Ann N Y Acad Sci* **877**, 339–367 (1999).
127. Grove, E. A., Domesick, V. B. & Nauta, W. J. Light microscopic evidence of striatal input to intrapallidal neurons of cholinergic cell group Ch4 in the rat: a study employing the anterograde tracer Phaseolus vulgaris leucoagglutinin (PHA-L). *Brain Res* **367**, 379–384 (1986).
128. Chang, H. T., Penny, G. R. & Kitai, S. T. Enkephalinergic-cholinergic interaction in the rat globus pallidus: a pre-embedding double-labeling immunocytochemistry study. *Brain Res* **426**, 197–203 (1987).
129. Mesulam, M. M., Mufson, E. J., Levey, A. I. & Wainer, B. H. Atlas of cholinergic neurons in the forebrain and upper brainstem of the macaque based on monoclonal choline acetyltransferase immunohistochemistry and acetylcholinesterase histochemistry. *Neuroscience* **12**, 669–686 (1984).
130. Sarter, M. & Bruno, J. P. Abnormal regulation of corticopetal cholinergic neurons and impaired information processing in neuropsychiatric disorders. *Trends Neurosci* **22**, 67–84 (1999).
131. Parikh, V. & Sarter, M. Cholinergic Mediation of Attention. *Ann N Y Acad Sci* **1129**, 225–235 (2008).
132. Kilgard, M. P. Cortical Map Reorganization Enabled by Nucleus Basalis Activity. *Science* **279**, 1714–1718 (1998).
133. Prakash, N. Basal Forebrain Cholinergic System Is Involved in Rapid Nerve Growth Factor (NGF)-Induced Plasticity in the Barrel Cortex of Adult Rats. *J Neurophysiol* **91**, 424–437 (2003).

134. Ramanathan, D., Tuszynski, M. H. & Conner, J. M. The Basal Forebrain Cholinergic System Is Required Specifically for Behaviorally Mediated Cortical Map Plasticity. *J Neurosci* **29**, 5992–6000 (2009).

Chapter 2

Novel recombinant adeno-associated viruses for Cre activated and inactivated transgene expression in neurons

Arpiar Saunders, Caroline A. Johnson, and Bernardo L. Sabatini

This chapter is based on our published work:

Saunders, A., Johnson, C. and Sabatini, B.L. Novel recombinant adeno-associated viruses for Cre activated and inactivated transgene expression. *Front. in Neural Circuits* 6:47.

Author Contributions A.S. and B.L.S. designed the experiments and wrote the paper.

A.S. performed the experiments and analyzed the data. C.A.J performed a subset of the immunostaining experiments and assisted in genotyping.

Abstract

Understanding the organization of the nervous system requires methods for dissecting the contributions of each component cell type to circuit function. One widely used approach combines genetic targeting of Cre recombinase to specific cell populations with infection of recombinant adeno-associated viruses (rAAVs) whose transgene expression is activated by Cre (“Cre-On”). Distinguishing how the Cre-expressing neurons differ functionally from neighboring Cre-negative neurons requires rAAVs that are inactivated by Cre (“Cre-Off”) and can be used in tandem with Cre-On viruses. Here we introduce two rAAV vectors that are inactivated by Cre and carry different fluorophore and optogenetic constructs. We demonstrate single and dual rAAV systems to achieve Cre-On and Cre-Off expression in spatially-intermingled cell populations of the striatum. Using these systems, we uncovered cryptic genomic interactions that occur between multiple Cre-sensitive rAAVs or between Cre-sensitive rAAVs and somatic Cre-conditional alleles and devised methods to avoid these interactions. Our data highlight both important experimental caveats associated with Cre-dependent rAAV use as well as opportunities for the development of improved rAAVs for gene delivery.

Introduction

Labeling and manipulating genetically-defined neurons *in vivo* is essential for understanding how specific cell types contribute to brain function, but requires methods to accurately introduce and potently express transgenes. One such method combines transgenic animals in which site-specific recombinases (SSRs) expressed in specific cell populations trigger transgene expression by activating DNA-based recombinant adeno-associated virus (rAAV) vectors¹⁻³.

Cre recombinase, like all SSRs, excises or recombines DNA depending on the relative orientation of short, directional DNA sequences⁴. The 34 bp lox sites, recognized by Cre, consist of two 13 base pair (bp) palindromic regions and an intervening non-palindromic 8 bp spacer that determines the orientation of the site. When two lox sites are oriented in the same direction, Cre excises the DNA flanked by the lox sites, leaving a single lox site behind. Conversely, when the lox sites are oriented in the opposite direction, Cre flips the flanked DNA into the antisense orientation. Both reactions involve the exchange of DNA between the two lox sites and are normally reversible⁵.

Differences in palindromic or spacer regions of lox sites, either naturally occurring⁶ or randomly mutated⁷, can confer specificity to Cre recognition. Exploiting lox variants that undergo variant-specific recombination has enabled strategies for making Cre recombination effectively irreversible⁸⁻¹⁰. The FLEEx system, first used as a Cre-reporter¹¹ and then applied to rAAV transgenes^{2,8}, uses recombination between

two pairs of like loxP and lox2272 sites to confer a permanent recombination event. Expression in the presence of Cre (“Cre-On”) is achieved by FLEx recombination of a transgene that changes the orientation of the coding sequence with respect to the promoter from the anti-sense to sense. Conversely, inactivation of expression in the presence of Cre (“Cre-Off”) can be achieved by simply starting the transgene in the sense orientation.

Cre-On rAAVs have been used widely to study the function of Cre-expressing neuron populations¹²⁻¹⁴, whereas Cre-Off rAAVs, despite their experimental value, have received only minor attention^{8,15}. In brain regions of transgenic Cre animals with intermingled cell types, Cre-Off rAAVs can be used to compare morphology, physiological properties, or behavioral function with that of Cre-expressing populations. Whereas transgenic Cre reporter animals that differentially label cells with and without Cre expression are of great utility¹⁶⁻¹⁸, these reporters are of limited use for comparing cell populations from defined brain regions at specific stages of development, since Cre reporting is permanent and occurs throughout the whole animal. Co-infection of Cre-On and Cre-Off rAAVs would allow such comparisons to be made in the same animal. However, due to our incomplete understanding of the AAV life cycle in cells, it is unclear how transduction of multiple rAAVs with engineered genetic elements may interact with each other and with engineered sites in the host cell genome.

Here we show that the presence of the same lox site variants in the Cre-On and Cre-Off rAAVs prevents their use to simultaneously target two cell populations. To circumvent this problem, new rAAVs were developed for the simultaneous manipulation

of multiple cell-populations via Cre-On and Cre-Off expression of transgenes. Using the FLEEx system and a third alternative lox site, we created a panel of Cre-Off rAAVs carrying genetically-encoded fluorophores or optogenetic constructs (Table 2.1) and validated two systems for simultaneous Cre-On and Cre-Off expression. In addition, we identify important caveats of using Cre sensitive rAAVs with genomic Cre conditional alleles and demonstrate how these can be avoided with the new tools.

Methods

rAAV cloning and production

Cloning of Double-floxed Inverted Orientation (DIO) Cre-On and Double-floxed Orientation (DO) / FAS Cre-Off vectors was based on the pAAV-Ef1a-DIO-hChR2(H134R)-mCherry-WPRE-pA vector from the Deisseroth Lab (http://www.stanford.edu/group/dlab/optogenetics/sequence_info.html). Cloning and sequence confirmation was done either in house or outsourced (Genscript). DIO and DO vectors were cloned using the Asc1 and Nhe1 restriction sites, introduced at the ends of transgenes through transgene-specific primers and PCR amplification. All transgenes were amplified from existing vectors except for ChETA-TdTomato, which was custom synthesized (Genscript). For DIO cloning, the Asc1 site was N-Terminal and the Nhe1 site C-Terminal with respect to the transgene; for DO cloning, the sites were reversed. All N-Terminal sites included a Kozak sequence (GCCACC) directly preceding the start codon. To generate FAS vectors, a custom insert was synthesized to replace the FLEEx insert and sub-cloned into the original pAAV-Ef1a-DIO-hChR2(H134R)-mCherry-WPRE-pA backbone using BamHI and EcoRI sites. The FAS insert preserves the original multiple cloning site

of the FLEEx insert and contains Asc1 and Nhe1 sites within the FAS sites which were used to subclone the other FAS transgenes. Full maps and clones are available on Addgene (<http://www.addgene.org/>).

All vectors were amplified with recombination deficient bacteria (OneShot Stbl3, Invitrogen) and tested functionally for Cre-On and Cre-Off expression by calcium phosphate transfection (Invitrogen) into HEK 293 cells, HEK 293 cells constitutively expressing Cre¹⁹, or HEK 293 cells co-transfected with fluorophore tagged Cre. After 2-6 days of expression, fluorescence was compared across conditions to ensure that transgene expression was Cre sensitive. Functional vectors were packaged as serotype 8 by a commercial vector core facility (University of North Carolina).

Stereotaxic injections

For intracranial injections, post-natal day 14 - 40 mice were anesthetized with isoflurane and placed into a stereotaxic apparatus. For co-injections, viruses were mixed at ratios that were adjusted empirically to achieve approximately equal expression levels of GFP and mCherry/TdTomato fluorophores. Virus was delivered at 100 nl/minute using a Microinject system (WPI). Striatum was targeted by directing the needle approximately 0.9 mm anterior and 2.4 mm lateral from Bregma and 2.1 mm from the pial surface. Cortical injections were targeted using the same anterior-posterior and medial-lateral coordinates, but the needle was directed 0.4 mm from the pial surface. Coordinates were adjusted slightly by age and 300-1000 nl were injected bilaterally. Following injections and wound closure, mice received ketoprofen (10mg/kg)

for analgesia and were returned to home cages for 3-4 weeks. All surgical procedures, animal handling, and euthanasia were carried out in accordance with federal guidelines and were approved by the Harvard Medical School Institutional Animal Care and Use Committee.

Fixed tissue preparation, immunostaining and imaging

Isoflorane anesthetized mice were transcardially perfused with 4% paraformaldehyde and the brains were post-fixed for 1-7 days. Brains were sectioned coronally or sagittally at 40-50 μm thickness using a Vibratome. No immune-enhancement was used to increase the signal of native fluorophores. For Cre immunohistochemistry, slices were incubated overnight at 4°C with mouse anti-Cre antibody (1:250, Millipore) in 1x PBS containing 5% normal goat serum (GIBCO) and 0.3% TritonX-100. The following day, tissue was rinsed in PBS, reacted with goat anti-mouse Alexa 647 (1:500, Molecular Probes) for 1 hour at room temperature in the same blocking buffer as for the primary antibody reaction. Slices were rinsed, mounted onto superfrost slides, dried and coverslipped under ProLong antifade reagent with DAPI (Molecular Probes). Whole-slide images were acquired with a VS110 slice scanning microscope (Olympus). To determine fluorophore co-expression, confocal stacks were taken with a Zeiss LSM 150 or Olympus FV1000 and analyzed using ImageJ.

Results

We used the Double-floxed Inverted Orientation (DIO) Cre-On vector pAAV-Ef1a-DIO-hChR2(H134R)-mCherry-WPRE-pA² as the parent vector to generate Double-floxed Orientation (DO) Cre-Off vectors by cloning fluorophores and optogenetic constructs in the forward orientation with respect to the Ef1a promoter (Figure 2.1). These DO vectors (Table 2.1) express the encoded protein until Cre-mediated recombination reverses the orientation of the transgene, leading to the transcription of non-functional mRNA (Figure 2.1A). In addition, we generated Cre-Switch vectors in which the coding sequences for two proteins are inserted with inverted orientations relative to each other such that Cre-mediated recombination and inversion switches which protein is expressed (Figure 2.1A). Lastly, the alternative lox site “FAS”⁶ was used to generate an independent FAS Cre-Off vector in which the coding sequence of the protein of interest is flanked by two FAS sites and is excised by Cre recombinase, turning off expression (Figure 2.1B). All vectors generated for this study, as well as additional Cre-On and Cre-Off viruses of similar design (Table 2.1), are available from Addgene (<http://www.addgene.org/>).

To test the Cre-Off vectors, we took advantage of the anatomy of the striatum. The vast majority (> 95%) of striatal neurons are medium spiny neurons (MSNs), which provide the only striatal output. MSNs come in two types which can be grouped by axonal projection pattern and dopamine receptor expression²⁰. Indirect pathway (iMSNs) express the dopamine receptor 2 (D2) and project exclusively to the Globus Pallidus (GP). Direct pathway MSNs (dMSNs) express the dopamine receptor 1 (D1) and project primarily to the Substantia Nigra reticulata (SNr) as well as a

Table 2.1. rAAV vectors and transgenes

DIO	DO	FAS	Cre-Switch (DO-DIO)
mCherry (37083)	mCherry (37119)	TdTomato (37092)	TdTomato-eGFP (37120)
eGFP (37084)	eGFP (37085)	eGFP (37091)	
ChETA-TdTomato (37755)	ChR2(H134R)-mCherry (37082)	ChR2(H134R)-mCherry (37090)	
	ChETA-eYFP (37086)	ChETA-TdTomato (37089)	
	ChETA-TdTomato (37756)	NpHR3.0-eYFP (37088)	
	NpHR3.0-eYFP (37087)		

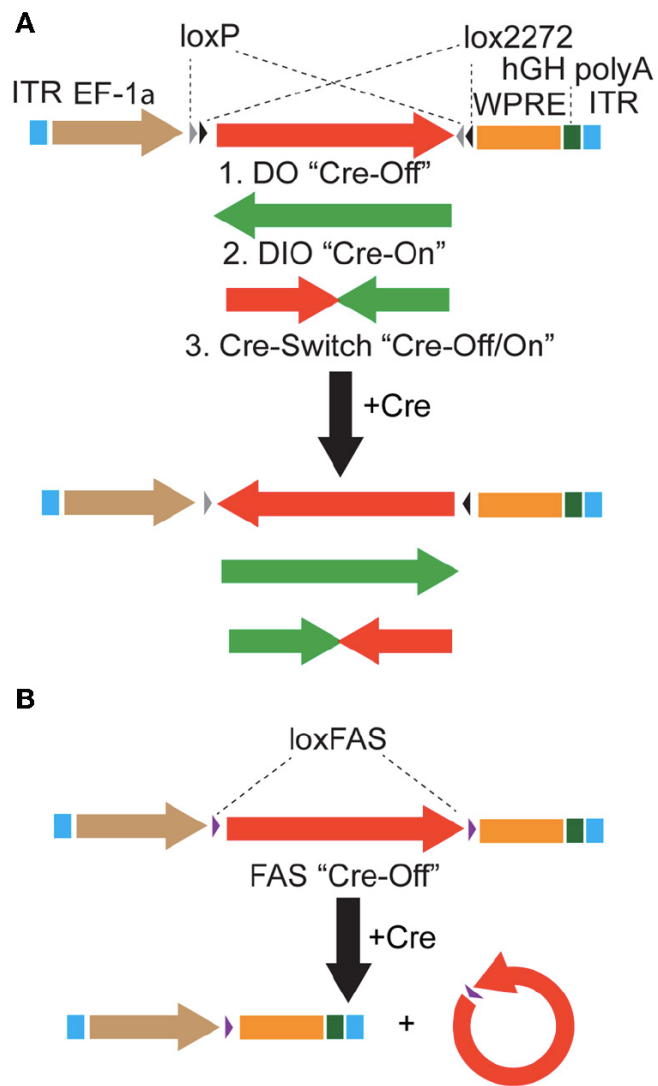
Addgene accession numbers are listed for each vector.

Figure 2.1. Strategies to achieve Cre-dependent rAAV transgene expression

A. Oppositely oriented loxP (grey triangle) and lox2272 (black triangle) sites permit Cre-mediated recombination and inversion of the flanked transgene with respect to the EF-1 α promoter. Downstream sequences stabilize the mRNA (woodchuck polyresponse element, WPRE) and trigger polyadenylation (human growth hormone polyadenylation, hGH polyA). After recombination, the transgene is flanked by one loxP and one lox2272 site, which do not recombine efficiently, effectively locking the transgene into position. The starting orientation of the transgene determines the Cre dependence of expression. The double-floxed orientation (1, DO) configuration, in which the open reading frame (ORF) of the transgene begins in the functional orientation with respect to the promoter, maintains expression only in cells lacking Cre (Cre-Off). In the opposite starting orientation, the double-floxed inverted (2, DIO) ORF must be recombined to be functional and expression is achieved only in Cre expressing cells (Cre-On). A single transgene containing two ORFs oriented oppositely with respect to each other and separated by stop codons (3, Cre-Switch) switches expression between the two ORFs depending on Cre expression. For Cre-Switch transgenes, the first, forward orientated ORF is expressed in Cre negative cells whereas the second, inverted ORF is activated in Cre positive cells. ITR = inverted terminal repeats.

B. Cre-Off control of transgene expression can also be achieved by Cre-based excision of the ORF using alternative lox FAS sites. loxFAS sites flank the ORF and are oriented in the same direction such that the flanked sequence is excised by Cre.

Figure 2.1 (Continued)



more minimal axon collateral in the GP²¹. Since dMSNs and iMSNs are equal in number, spatially intermingled, and selectively targetable for Cre expression using BAC transgenes²², the anatomy of the striatum provides an ideal test system for Cre-On and Cre-Off rAAVs.

Using transgenic mice in which Cre expression is driven by the dopamine receptor 2 regulatory sequences (D2-Cre)²² and thus restricted to iMSNs, we infected the striata with DIO-GFP or DO-mCherry rAAVs and compared the GFP/mCherry⁺ projections in sagittal slices of fixed tissue 3-4 weeks post-infection. As expected, DIO-GFP expression was restricted to projections to the GP, the sole innervation zone of iMSNs ([Figure 2.2A](#)). Conversely, DO-mCherry expression was restricted to projections that provided a very minimal arbor in the GP but a large arbor in the SNr, the main innervation zone of dMSNs ([Figure 2.2B](#)). These anatomical results suggest that DO-GFP expression was excluded from Cre-expressing iMSNs.

To quantify the efficiency with which stable, transgenic Cre expression turns off DO rAAV expression, Cre-expressing (Cre⁺) neurons in the striatum of D2-Cre mice infected with DO-GFP were identified with an antibody against Cre. Confocal imaging of the infection zone and quantification of the number of cells positive for Cre and/or GFP revealed that of 692 Cre⁺ and 496 GFP⁺ cells (N=4 infections) only 1 cell was double-positive ([Figure 2.2C](#)). Similarly, to quantify the ability of virally introduced Cre to turn off DO expression, we infected the striata of wild-type mice simultaneously with rAAVs carrying Cre-mCherry and DO-GFP at titers that resulted in roughly equal numbers of cells expressing Cre-mCherry and GFP ([Figure 2.2D](#)). After 3-4 weeks of infection, of 295

Figure 2.2. DIO and DO rAAVs achieve Cre-On and Cre-Off expression but exhibit interfering interactions when co-infected.

A. Sagittal section through a D2-Cre mouse infected with DIO-GFP in the striatum. GFP⁺ axons emanating from the striatal infection innervate the globus pallidus (GP), the target of indirect pathway medium spiny neurons (iMSNs). No GFP⁺ expression is observed in the substantia nigra reticulata (SNr, inset). COR = cortex, STR = striatum.

B. Sagittal section through a D2-Cre mouse infected with DO-mCherry in the striatum such that mCherry expression is excluded from iMSNs. mCherry⁺ axons leaving the striatum innervate the SNr (inset), consistent with expression in direct pathway MSNs (dMSNs).

C. Antibody staining against Cre in D2-Cre striatum infected with DO-mCherry reveals that Cre efficiently turns off mCherry expression, indicative of Cre-Off behavior. *top*, a single confocal plane showing mCherry expression excluded from cells with Cre⁺ nuclei. *bottom*, Quantification of co-expression of Cre and mCherry (N=4 infections, N=1,187 cells) reveals that mCherry expression (N=495 cells) was almost completely excluded from Cre⁺ cells (N=1/691 cells double-positive for mCherry and Cre).

D. Co-infection of rAAVs encoding a Cre-mCherry fusion and DO-GFP into the striatum of a wild type (WT) mouse efficiently prevents GFP expression in Cre-mCherry expressing cells. *top*, a single confocal plane containing interspersed mCherry⁺ and GFP⁺ cells. Note that the mCherry expression is nuclear due to nuclear targeting of Cre. The arrowhead indicates a cell co-expressing mCherry and GFP. *bottom*, confocal imaging of infected tissue (N=2 infections, N=521 cells) reveals that cells expressing Cre-mCherry (N=237)

Figure 2.2 (Continued)

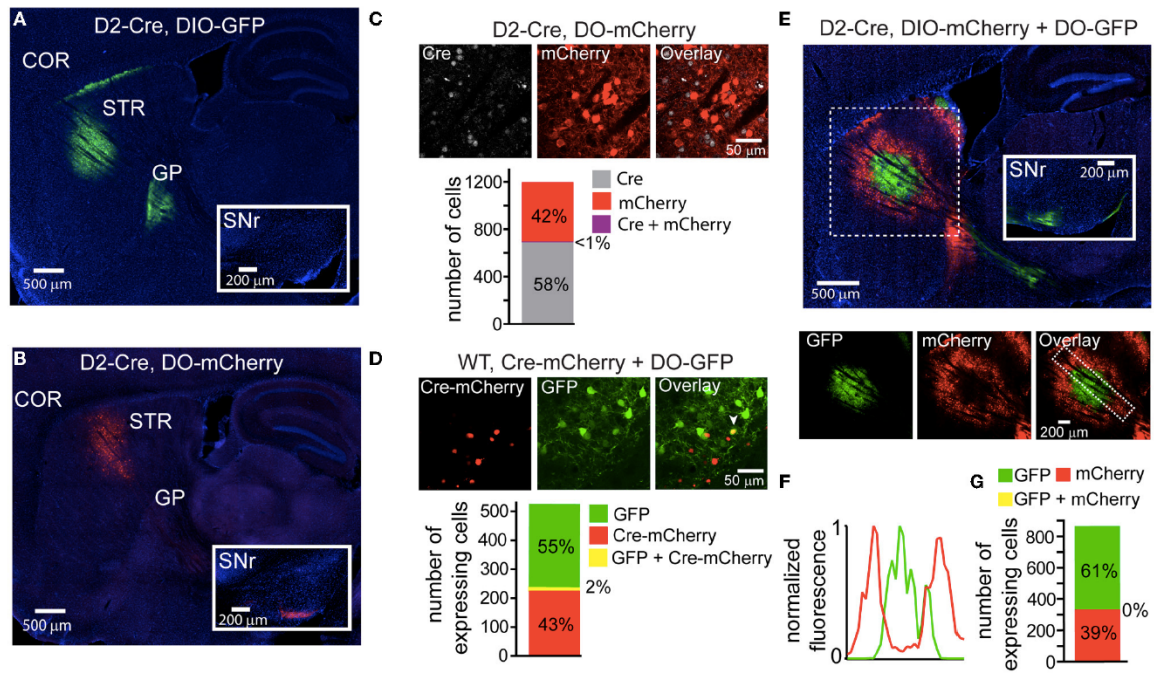
and cells expressing GFP (N=284) are largely non-overlapping (N=11/521 cells were double-positive for both fluorophores).

E. Sagittal section through a D2-Cre mouse infected with DIO-mCherry and DO-GFP in the striatum. Despite the physical intermixing of Cre positive and negative neurons in the striatum, the resulting GFP and mCherry expression is spatially segregated. *below*, separate visualization of the green and red fluorescence channels demonstrates that mCherry is excluded from of the striatal volume expressing GFP.

F. Normalized mean fluorescent values for GFP and mCherry quantified from boxed inset in E, *bottom right*.

G. Confocal imaging around the border regions (N=2 infections, N=865 cells) containing both GFP⁺ (N=529) and mCherry⁺ (N=336) cells revealed no overlap in expression.

Figure 2.2 (Continued)



Cre-mCherry⁺ and 237 GFP⁺ cells, 11 cells were double positive (N=4 infections). Thus, either constitutive expression of Cre from a BAC or simultaneous viral introduction of Cre efficiently turns off expression of DO rAAVs.

Interference of expression with co-infection of DIO and DO viruses

Many experiments would benefit from simultaneous expression of different transgenes in Cre-expressing and non-Cre expressing cell populations. We tested whether DIO and DO rAAVs can be used to target expression to distinct cell populations by simultaneously infecting the striata of D2-Cre mice with DIO-mCherry and DO-GFP (Figure 2.2E). While both mCherry⁺ and GFP⁺ cells were observed in striatum, their fluorescent signals were not intermingled: GFP expression dominated around the injection site, whereas mCherry expression was strongest on the edges of the infection volume. This mutually exclusive expression pattern was quantified by comparing the GFP and mCherry fluorescence signals in the infected area (Figure 2.2F). Despite the lack of intermingled expression, the Cre dependence of the Cre-On and Cre-Off rAAVs was maintained, as GFP⁺ and mCherry⁺ axons were restricted to the GP and SNr respectively, and confocal imaging in the small border areas containing intermingled GFP and mCherry expressing cells demonstrated non-overlapping expression at the cellular level (Figure 2.2G): of 336 mCherry⁺ cells and 529 GFP⁺ cells, none expressed both fluorophores (N=4 infections).

Cre-Switch and alternative Cre-Off systems

We hypothesized that the lack of DIO Cre-On expression in striatal volumes with strong DO Cre-Off expression was due to the presence of loxP and lox2272 sites in both vectors. We therefore designed two new Cre-sensitive rAAV vectors to achieve simultaneous Cre-On and Cre-Off expression. We tested whether differential Cre-On and Cre-Off expression could be achieved using Cre-mediated inversion of a single transgene¹¹. This “Cre-Switch” transgene encodes two open reading frames positioned back-to-back but in inverted orientations such that the coding sequence located next to the promoter is in the sense orientation ([Figure 2.1A](#)). We synthesized a Cre-Switch transgene encoding Cre-Off TdTomato and Cre-On GFP, and injected the rAAV containing this construct into the striata of mice where Cre is expressed behind the dopamine receptor 1 regulatory sequences (D1-Cre) and is thus restricted to dMSNs. ([Figure 2.3](#))²². GFP and TdTomato expressing cells were intermingled within the striatum ([Figure 2.3A](#), top left) and quantification of normalized average GFP and TdTomato signals revealed no spatial interference ([Figure 2.3B](#)). Consistent with differential Cre expression, Cre-On GFP⁺ projections were observed in the SNr, while Cre-Off TdTomato⁺ projections were visible in the GP ([Figure 2.3A](#)). Confocal microscopy revealed that of 494 GFP⁺ cells, and 307 TdTomato⁺ cells, only 5 cells were double-positive (N=3 infections). Since TdTomato is expressed in the absence of Cre, the larger proportion of GFP⁺ vs. TdTomato⁺ cells likely reflects undetectably low levels of TdTomato expression rather than inefficient recombination. Thus Cre-Switch transgenes

Figure 2.3. A single orientation switching transgene can mediate Cre-On and Cre-Off expression without spatial interference.

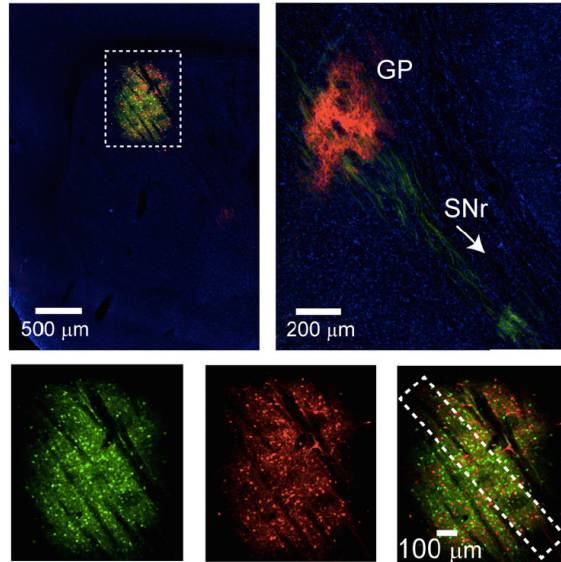
A. *Left*, Sagittal section through a D1-Cre mouse infected with a Cre-Switch transgene encoding Cre-Off TdTomato and Cre-On GFP in the striatum. *Right*, more medial section containing the GP and both TdTomato⁺ and GFP⁺ projections. *Bottom*, GFP and TdTomato fluorescence is spatially intermingled.

B. Normalized mean fluorescent values for GFP and TdTomato quantified from boxed inset in A, *bottom right*.

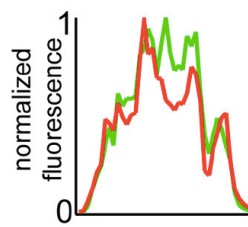
C. Confocal imaging through the infection volume (N=3 infections, N=796 cells) revealed that GFP (N=489 cells) and TdTomato (N=302 cells) were expressed in largely non-overlapping cell populations (N=7/791 cells were double-positive for GFP and TdTomato).

Figure 2.3 (Continued)

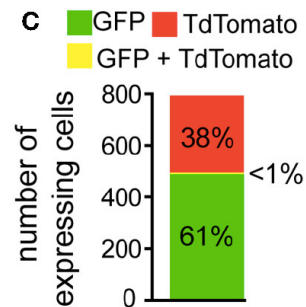
A D1-Cre, Cre-Switch (TdTomato-GFP)



B



C



efficiently target the expression of different transgenes to Cre-expressing and non-expressing cell populations.

Cre-Switch transgenes are limited both by the small packaging capacity of rAAVs and the cost associated with building unique rAAVs to achieve the desired combinations of transgenes for expression targeting. We therefore designed an alternative Cre-Off rAAV vector that could be co-infected with DIO Cre-On vectors without spatial interference. Based on our hypothesis that spatial interference results from shared lox sites on the Cre-On and Cre-Off vectors, we designed a set of Cre-Off rAAVs that uses the FAS lox site variant (Table 2.1). LoxFAS sites do not undergo efficient recombination with either loxP or lox2272 in bacteria ⁶. To achieve Cre-Off expression, the sense oriented rAAV transgene was flanked by loxFAS sites oriented in the same direction ([Figure 2.1B](#)), leading to Cre-mediated excision of the flanked transgene. The Cre-Off FAS vector, henceforth called FAS, was tested by injecting FAS-tdTomato into the striata of D2-Cre and D1-Cre mice and examining the labeled projections ([Figure 2.4](#)). Cre expression in iMSNs resulted in large TdTomato⁺ arborizations to the SNr but only minor arborizations in GP ([Figure 2.4A](#)) whereas Cre expression in dMSNs resulted in a large arborization in GP and no expression in SNr ([Figure 2.4B](#)), indicating that Cre efficiently eliminates FAS rAAV transgene expression.

The efficiency of stable transgenic Cre expression in turning off FAS expression was quantified in fixed slices of striatum of D2-Cre mice infected with FAS-TdTomato

Figure 2.4. LoxFAS excision achieves efficient Cre-Off rAAV expression that does not interfere with DIO Cre-On expression.

A. Sagittal section through a D2-Cre mouse infected with FAS-TdTomato in the striatum. TdTomato is excluded from iMSNs. TdTomato⁺ axons arborize in the SNr (inset) but only minimally in the GP, consistent with expression in dMSNs.

B. Sagittal section through a D1-Cre mouse infected with FAS-TdTomato in the striatum. TdTomato expression is excluded from dMSNs. TdTomato⁺ axons leaving the striatum target the GP, but not the SNr (inset), consistent with exclusion from dMSNs.

C. Antibody staining against Cre in D2-Cre striatum infected with FAS-TdTomato reveals efficient Cre-Off expression in the presence of Cre. *top*, a single confocal plane showing Cre⁺ nuclei excluded from interspersed TdTomato⁺ cells. *bottom*, confocal imaging through infected and stained tissue volumes (N=4 infections, N=929 cells) revealed that TdTomato expression (N=477 cells) was completely absent in Cre⁺ cells (N=452).

D. Co-infection of rAAVs Cre-GFP and FAS-TdTomato into the striatum of a wild type (WT) mouse leads to efficient exclusion of TdTomato in Cre-GFP expressing cells. *top*, a single confocal plane containing interspersed GFP⁺ and TdTomato⁺ cells. Note that the GFP expression is nuclear due to the targeting of Cre. The arrowheads indicate cells co-expressing GFP and TdTomato. *bottom*, confocal imaging of volumes of infected tissue (4 infections, N=1,258 cells) reveal that a small fraction of the total GFP⁺ expressing cells (N=948) also expressed TdTomato (N=40 cells). Conversely, the majority of TdTomato⁺ cells (N=610) did not express Cre-GFP.

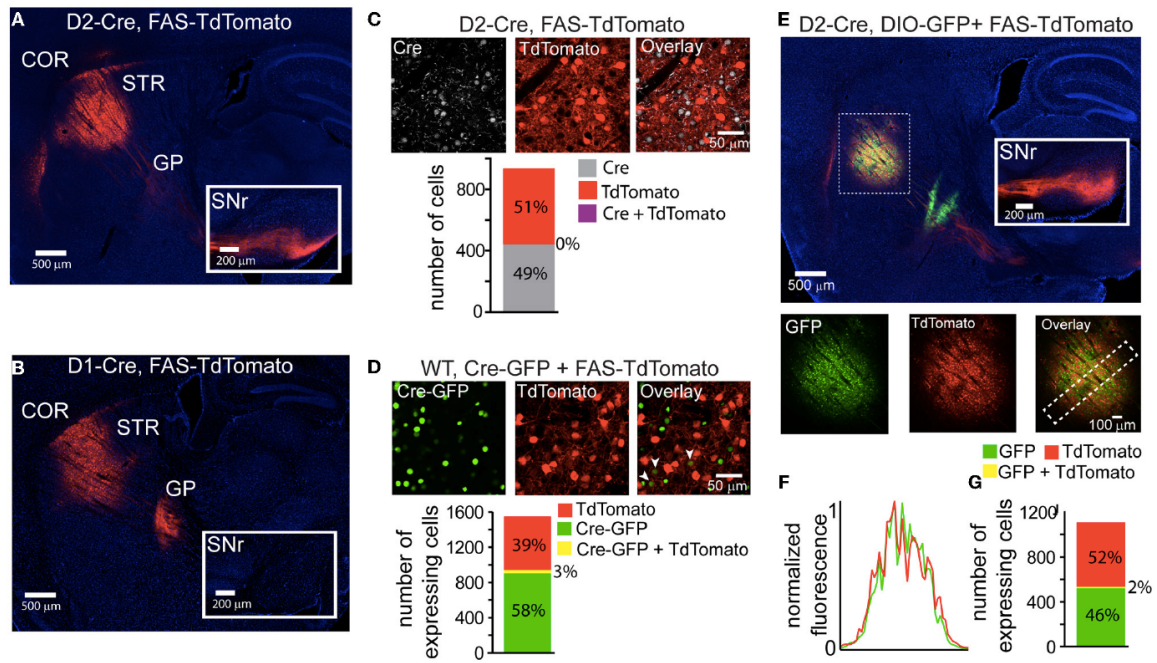
Figure 2.4 (Continued)

E. Sagittal section through a D2-Cre mouse infected with DIO-GFP and FAS-TdTomato in the striatum. GFP⁺ axons arborize in the GP, whereas TdTomato⁺ axons pass through GP en route to the SNr. *bottom*, GFP and TdTomato signals exhibit spatially intermingled expression patterns.

F. Normalized mean fluorescent values for GFP and TdTomato quantified from boxed inset in E, *bottom right*. GFP and TdTomato expression levels mirror each other throughout the infection area.

G. Confocal imaging through infected volumes (N=3 infections, N=1116 cells) revealed that DIO and FAS co-infection targeted expression to mostly non-overlapping cell populations (FAS-TdTomato, N= 578 cells; DIO-GFP, N=519; FAS-TdTomato and DIO-GFP, N=19).

Figure 2.4 (Continued)



and immunostained for Cre ([Figure 2.4C](#)). Of 477 TdTomato⁺ cells and 452 Cre⁺ cells, no cells were double-positive (N=4 infections). Thus stable transgenic Cre expression efficiently eliminates FAS rAAV transgene expression, leading to undetectable fluorophore expression within 3-4 weeks.

To quantify the efficiency of virally introduced Cre to turn off FAS expression, we infected the striata of wild-type mice simultaneously with rAAVs carrying Cre-GFP and FAS-TdTomato at titers where approximately equal numbers of cells expressed Cre-mCherry and GFP ([Figure 2.4D](#)). We used confocal microscopy to image areas of the infection zone with interspersed Cre-GFP and TdTomato expressing cells and quantified the number of cells positive for Cre-GFP, TdTomato, or double-positive for both. Of 948 Cre-GFP⁺ and 650 TdTomato⁺ cells, 40 were double-positive (N=4 infections). Thus viral introduction of Cre efficiently turns off expression of simultaneously infected FAS rAAVs.

To test whether Cre-Off FAS and Cre-On DIO rAAVs could be co-infected without spatial interference, FAS-TdTomato and DIO-GFP were injected into the striatum of D2-Cre mice ([Figure 2.4E](#)). GFP⁺ and TdTomato⁺ cells were intermingled in the striatum and did not exhibit interference ([Figure 2.4F](#)). GFP⁺ but not TdTomato⁺ projections were observed in the GP and only TdTomato⁺ were observed en route to the SNr, consistent with Cre-On GFP expression in iMSNs and Cre-Off TdTomato expression in dMSNs. Confocal microscopy revealed that of 519 GFP⁺ cells, and 578 TdTomato⁺ cells, 19 cells were double-positive ([Figure 2.4G](#)) (N=4 infections). Thus co-infection of FAS and DIO rAAVs targets efficient Cre-Off and Cre-On expression without spatial interference.

Cre-On/Off viral use in mice with Cre-conditional alleles

Cre-reporter alleles are used to visualize the spatial distribution of cells that have expressed Cre at any point in development. Cre activates the reporter by excising a stop cassette flanked by loxP sites and located between the promoter and the reporter gene²³. Many anatomical or physiological experiments would benefit from simultaneous labeling of a Cre-reporter and Cre-On or Cre-Off rAAVs. We used a mouse in which Cre expression is driven under the regulatory control of Parvalbumin and reported by TdTomato fluorescence (PV-Cre;Ai9-lsl-tdTomato) to test whether Cre-Off rAAV labeling could be used in conjunction with a Cre reporter allele²³. Injection of DO-GFP into the cortex of PV-Cre;Ai9-lsl-tdTomato mouse, resulted in a robust drop in TdTomato reporter fluorescence in the infection area ([Figure 2.5A](#)), indicating shut-down of the previously active genomic allele. Quantification of normalized average GFP and TdTomato signals illustrates this inverse relationship between expression levels of the two fluorophores ([Figure 2.5B](#)). In contrast, when Cre-Off FAS-GFP was injected, no reduction in TdTomato reporter fluorescence was observed ([Figure 2.5C](#)).

Quantification of normalized average GFP and TdTomato signals illustrates no spatial interference between the two fluorophores in this case ([Figure 2.5D](#)).

Confocal microscopy demonstrated that fluorophore expression from DO- and FAS-based Cre-off viruses was efficiently excluded from PV-Cre cortical interneurons. Of 527 DO-GFP⁺ cells and 43 TdTomato⁺ cells, none were double positive (N=2 infections) ([Figure 2.5E](#)).

Figure 2.5. Cre-Off infection with DO rAAV interferes with the expression of fluorescent Cre reporter allele whereas infection with FAS rAAV does not.

A. Coronal section through the cortex of PV-Cre;Ai9-IsI-TdTomato mouse after infection with DO-GFP. Separate GFP and TdTomato fluorescent channels demonstrate that Cre reporter fluorescence is drastically reduced in the area of DO-GFP infection.

B. Normalized mean fluorescent values for GFP and TdTomato quantified from boxed inset in A.

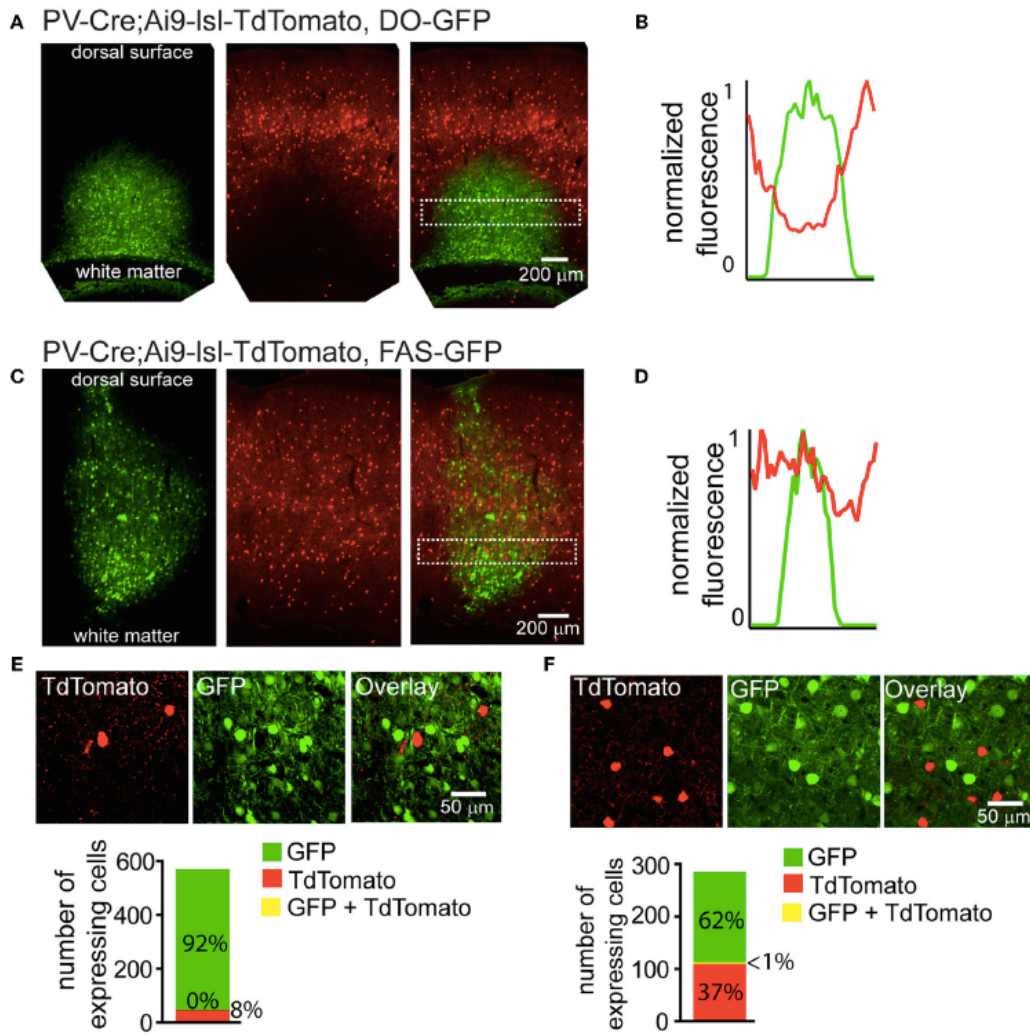
C. Coronal section through the cortex of PV-Cre; Ai9-IsI-TdTomato mouse after infection with FAS-GFP. Separate GFP and TdTomato fluorescent channels demonstrate that Cre reporter fluorescence is not reduced in the area of FAS-GFP infection.

D. Normalized mean fluorescent values for GFP and TdTomato quantified from boxed inset in C.

E. DO-GFP expression is excluded from remaining TdTomato⁺ cells in the conditions shown in (A). *top*, a single confocal plane at the border region of the infection containing both TdTomato⁺ and GFP⁺ cells. *bottom*, confocal imaging of volumes of infected tissue (N=2 infections, N=527 GFP⁺ cells, N=43 TdTomato⁺ cells) reveal GFP expression is excluded from TdTomato⁺ cells.

F. FAS-GFP expression is excluded from TdTomato⁺ cells in the conditions shown in (C). *top*, a single confocal plane of the infection containing both TdTomato⁺ and GFP⁺ cells. *bottom*, confocal imaging of volumes of infected tissue (N=2 infections, N=177 GFP⁺ cells, N=105 TdTomato⁺ cells) reveal GFP expression is almost completely excluded from TdTomato⁺ cells (N=1/282 cells double-positive for GFP and TdTomato).

Figure 2.5 (Continued)



Of 177 FAS-GFP⁺ cells and 105 TdTomato⁺ cells, 1 was double-positive (N=2 infections) ([Figure 2.5F](#)). Exclusion of GFP from TdTomato⁺ cells suggests that Cre was present in these cortical PV-Cre cells at the time of infection and efficiently recombines or excises the transgene to turn off GFP expression.

Co-expression of multiple rAAV transgenes

Due to the limited packaging capacity of rAAVs, infecting multiple Cre-On or Cre-Off rAAVs may be an effective way to introduce more than one transgene in the same cell populations. We tested whether multiple Cre-On or Cre-Off rAAVs could be co-infected without spatial interference of transgene expression by infecting the striatum and quantifying GFP and mCherry/TdTomato fluorescence. Co-infection of the striatum of D2-Cre mice with DIO-mCherry and DIO-GFP resulted in similar levels of mCherry and GFP expression ([Figure 2.6A](#)) without spatial interference. Co-infection of the striatum from wild type mice with 3 different Cre-Off rAAV combinations (DO+DO, DO+FAS, and FAS+FAS) also resulted in expression patterns lacking spatial interference ([Figure 2.6B-D](#)).

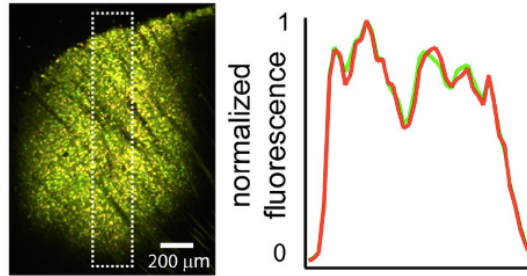
Figure 2.6. Co-infection with DIO or DO/FAS rAAVs drives co-expression without spatial interference.

A. Infection of multiple DIO Cre-On rAAVs results in co-expression of transgenes without interference. *left*, a sagittal section of a D2-Cre mouse infected with DIO-GFP and DIO-mCherry in the striatum. *right*, normalized mean fluorescent values for GFP and mCherry quantified from boxed inset in A.

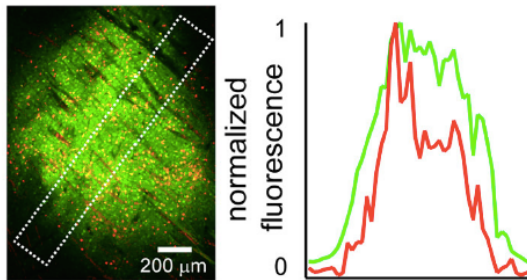
B-D. Infection of multiple Cre-Off rAAVs results in co-expression of transgenes without spatial interference. *left*, sagittal sections from wild type mice infected with B. DO-mCherry + DO-GFP, C. DO-mCherry + FAS-GFP or D. FAS-TdTomato + FAS-GFP in the striatum. *right*, normalized mean fluorescent values for GFP and mCherry/TdTomato quantified from boxed inset in to the left.

Figure 2.6 (Continued)

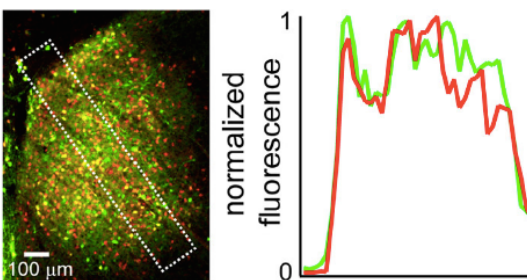
A D2-Cre, DIO-GFP + DIO-mCherry



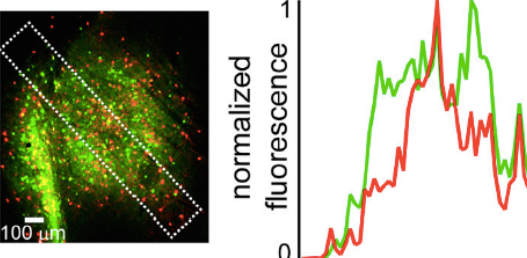
B WT, DO-mCherry + DO-GFP



C WT, DO-mCherry + FAS-GFP



D WT, FAS-TdTomato + FAS-GFP



Discussion

Achieving Intermingled Cre-On and Cre-Off rAAV expression

We designed rAAV expression vectors that allow different transgenes to be simultaneously targeted to spatially intermingled cell populations with and without Cre. Although the FLEEx system is widely used to achieve Cre-On (DIO) expression, Cre-Off rAAVs are not readily available. Therefore, we used the FLEEx system to generate Cre-Off rAAVs (DO) and confirmed the efficacy of this design using striatal injections. High efficiency Cre-On and Cre-Off expression when each system is used in isolation was confirmed both for constitutive genomic Cre expression as well as for acute virally-induced Cre expression.

Whereas DIO and DO rAAVs achieve the expected Cre-On and Cre-Off expression when injected individually, when co-infected, DIO expression was absent in areas with DO expression. This data suggests that many cells within the infection volume were transduced by both DIO and DO rAAV particles, yet expression failed to occur only in Cre expressing cells. However, the presence of Cre and multiple FLEEx rAAVs is not sufficient for interference, since DIO/DIO rAAV co-infection led to robust expression from both vectors. The absence of DO expression at the periphery of the example infection was not present in all DIO and DO combinations and thus likely represents a lack of DO rAAV spread and infection rather than Cre-independent interference. Therefore the interference we describe requires Cre and FLEEx rAAVs with oppositely oriented transgenes.

Although the exact nature of the destructive, Cre-dependent interference occurring between DIO and DO rAAVs present in the same cell is unknown, we hypothesize that it resulted from intermolecular recombination involving loxP and lox2272 sites. Intermolecular recombination between rAAVs is well documented²⁴. rAAV genomes are single stranded but most undergo second strand synthesis in the nucleus before becoming competent for transgene expression. Double strand synthesis is initiated through self-priming DNA hairpins formed by the inverted terminal repeats (ITRs). These single stranded rAAVs are subject to other types of folding based on DNA complementarity and these interactions can mediate both intra- and inter-molecular recombination^{24,25} and can be exploited to fuse two independent rAAV genomes into a single expression system²⁶⁻²⁸. Lox sites could therefore be a feasible substrate for Cre-dependent intermolecular interactions in the nucleus. Alternatively, inter-molecular recombination could result in the transcription of double-stranded RNAs that alter protein translation by many mechanisms²⁹⁻³¹.

We describe two solutions for simultaneous Cre-On and Cre-Off expression that are consistent with this idea. First, Cre-Switch rAAVs avoid recombination across heterogeneous rAAV vectors since only a single rAAV type is present. Second, rAAVs which use the loxFAS site to achieve Cre-Off expression avoid recombination with DIO rAAVs, since the loxFAS site does not efficiently recombine with loxP or lox2272.

rAAV and somatic genome interactions involving loxP

Fluorescent Cre-reporter alleles are routinely used to visualize cells that express Cre. The Ai9 reporter uses a loxP flanked stop cassette to prevent TdTomato transcription driven by a CAG promoter²³. Cre-mediated recombination excises the stop cassette allowing TdTomato transcription. This process leaves behind a single loxP site. In mice in which this reporter is used to visualize cells expressing Cre under control of the parvalbumin regulatory sequence, cortical injections of DO-GFP rAAV produced a striking drop in TdTomato fluorescence in the infection area. Similar effects have been observed with DIO rAAVs and in other cell types throughout the brain (A.S., unpublished observation). Thus, FLEEx rAAVs should be used with caution in animals with loxP-dependent conditional alleles and the status of the genomic allele must be examined in infected tissue. In contrast, injections with FAS-GFP do not affect reporter fluorescence, indicating that reduced reporter fluorescence with FLEEx viruses is not due to rAAV infection or over-expression, but is due to elements, such as the loxP sites, that differ between the FAS and DO/DIO viral genomes.

One intriguing possibility is that the single loxP sites remaining in each of the rAAV and somatic genomes following Cre mediated recombination may mediate integration of rAAV DNA between the CAG promoter and TdTomato coding sequence. Integration of even a single DO rAAV genome (~4.5 kb) might be sufficient to interfere with transcription and be considered, in effect, insertion of an exogenous rAAV-based stop cassette. Since loxFAS sites do not efficiently recombine with loxP, this putative integration would be inefficient in FAS rAAVs⁶.

AAV integration into somatic genomes is well documented³² and Cre-lox can mediate integration reversibly with excision⁴. The robust drop in reporter fluorescence suggests a highly efficient and irreversible process, but how DO-GFP integration could become permanent is unclear. Regardless of the mechanism, FLEx rAAVs may interact cryptically with other genomic loxP sites, such as those left behind by conditionally deleted alleles. Once understood, these interactions may be useful for introducing DNA back into targeted genomic sites using somatic loxP and rAAVs.

References

1. Kuhlman, S. J. & Huang, Z. J. High-resolution labeling and functional manipulation of specific neuron types in mouse brain by Cre-activated viral gene expression. *PLoS ONE* **3**, e2005 (2008).
2. Sohal, V. S., Zhang, F., Yizhar, O. & Deisseroth, K. Parvalbumin neurons and gamma rhythms enhance cortical circuit performance. *Nature* 1–5 (2009). doi:10.1038/nature07991
3. Betley, J. N. & Sternson, S. M. Adeno-Associated Viral Vectors for Mapping, Monitoring, and Manipulating Neural Circuits. *Hum Gene Ther* **22**, 669–677 (2011).
4. Tronche, F., Casanova, E., Turiault, M., Sahly, I. & Kellendonk, C. When reverse genetics meets physiology: the use of site-specific recombinases in mice. *FEBS Lett.* **529**, 116–121 (2002).
5. Van Duyne, G. D. A structural view of cre-loxp site-specific recombination. *Annu Rev Biophys Biomol Struct* **30**, 87–104 (2001).
6. Siegel, R. W., Jain, R. & Bradbury, A. Using an in vivo phagemid system to identify non-compatible loxP sequences. *FEBS Lett.* **505**, 467–473 (2001).
7. Sheren, J., Langer, S. J. & Leinwand, L. A. A randomized library approach to identifying functional lox site domains for the Cre recombinase. *Nucleic Acids Res* **35**, 5464–5473 (2007).

8. Atasoy, D., Aponte, Y., Su, H. H. & Sternson, S. M. A FLEX switch targets Channelrhodopsin-2 to multiple cell types for imaging and long-range circuit mapping. *J Neurosci* **28**, 7025–7030 (2008).
9. Araki, K., Araki, M. & Yamamura, K. Targeted integration of DNA using mutant lox sites in embryonic stem cells. *Nucleic Acids Res* **25**, 868–872 (1997).
10. Albert, H., Dale, E. C., Lee, E. & Ow, D. W. Site-specific integration of DNA into wild-type and mutant lox sites placed in the plant genome. *The Plant Journal* **7**, 649–659 (1995).
11. Schnütgen, F. *et al.* A directional strategy for monitoring Cre-mediated recombination at the cellular level in the mouse. *Nat Biotechnol* **21**, 562–565 (2003).
12. Cardin, J. A. *et al.* Driving fast-spiking cells induces gamma rhythm and controls sensory responses. *Nature* 1–6 (2009). doi:10.1038/nature08002
13. Kravitz, A. V. *et al.* Regulation of parkinsonian motor behaviours by optogenetic control of basal ganglia circuitry. *Nature* **466**, 622–626 (2010).
14. Cohen, J. Y., Haesler, S., Vong, L., Lowell, B. B. & Uchida, N. Neuron-type-specific signals for reward and punishment in the ventral tegmental area. *Nature* **482**, 85–88 (2012).
15. Zhao, T. *et al.* mGRASP enables mapping mammalian synaptic connectivity with light microscopy. *Nat Methods* 1–9 (2011). doi:10.1038/nmeth.1784
16. Lobe, C. G. *et al.* Z/AP, a double reporter for cre-mediated recombination. *Dev Biol* **208**, 281–292 (1999).
17. Novak, A., Guo, C., Yang, W., Nagy, A. & Lobe, C. G. Z/EG, a double reporter mouse line that expresses enhanced green fluorescent protein upon Cre-mediated excision. *genesis* **28**, 147–155 (2000).
18. Muzumdar, M. D., Tasic, B., Miyamichi, K., Li, L. & Luo, L. A global double-fluorescent Cre reporter mouse. *genesis* **45**, 593–605 (2007).
19. Langer, S. J., Ghafoori, A. P., Byrd, M. & Leinwand, L. A genetic screen identifies novel non-compatible loxP sites. *Nucleic Acids Res* **30**, 3067–3077 (2002).
20. Smith, Y., Bevan, M. D., Shink, E. & Bolam, J. P. Microcircuitry of the direct and indirect pathways of the basal ganglia. *Neuroscience* **86**, 353–387 (1998).

21. Kawaguchi, Y., Wilson, C. J. & Emson, P. C. Projection subtypes of rat neostriatal matrix cells revealed by intracellular injection of biocytin. *J Neurosci* **10**, 3421–3438 (1990).
22. Gong, S. *et al.* A gene expression atlas of the central nervous system based on bacterial artificial chromosomes. *Nature* **425**, 917–925 (2003).
23. Madisen, L. *et al.* A robust and high-throughput Cre reporting and characterization system for the whole mouse brain. *Nat Neuro* **13**, 133–140 (2010).
24. Yang, J. *et al.* Concatamerization of adeno-associated virus circular genomes occurs through intermolecular recombination. *J Virol* **73**, 9468–9477 (1999).
25. Mccarty, D. M. *et al.* Adeno-associated virus terminal repeat (TR) mutant generates self-complementary vectors to overcome the rate-limiting step to transduction in vivo. *Gene Ther* **10**, 2112–2118 (2003).
26. Sun, L., Li, J. & Xiao, X. Overcoming adeno-associated virus vector size limitation through viral DNA heterodimerization. *Nat Med* **6**, 599–602 (2000).
27. Duan, D., Yue, Y., Yan, Z. & Engelhardt, J. F. A new dual-vector approach to enhance recombinant adeno-associated virus-mediated gene expression through intermolecular cis activation. *Nat Med* **6**, 595–598 (2000).
28. Nakai, H., Storm, T. A. & Kay, M. A. Increasing the size of rAAV-mediated expression cassettes in vivo by intermolecular joining of two complementary vectors. *Nat Biotechnol* **18**, 527–532 (2000).
29. Alvarez, V. A., Ridenour, D. A. & Sabatini, B. L. Retraction of synapses and dendritic spines induced by off-target effects of RNA interference. *J Neurosci* **26**, 7820–7825 (2006).
30. Blum, R., Kafitz, K. W. & Konnerth, A. Neurotrophin-evoked depolarization requires the sodium channel NaV 1.9. *Nature* **419**, 687–693 (2002).
31. Sledz, C. A. & Williams, B. R. G. RNA interference and double-stranded-RNA-activated pathways. *Biochem Soc Trans* **32**, 952–956 (2004).
32. Smith, R. H. Adeno-associated virus integration: virus versus vector. *Gene Ther* **15**, 817–822 (2008).

Chapter 3

Recurrent network activity drives striatal synaptogenesis

Yevgenia Kozorovitskiy*, Arpiar Saunders*, Caroline A. Johnson, Bradford B. Lowell &
Bernardo L. Sabatini

*equal contribution

This chapter is based on our published work:

Kozorovitskiy, Y. *, Saunders, A. *, Johnson, C., Lowell, B.B. & Sabatini, B.L. Recurrent network activity drives striatal synaptogenesis. *Nature* 485: 646-650.

Author Contributions Y.K., A.S. and B.L.S. designed the experiments. Y.K. and A.S. performed experiments and analysed data. C.A.J. assisted in experiments and genotyping. B.B.L. generated the conditional *Slc32a1* mouse. Y.K., A.S. and B.L.S. wrote the paper with contributions from C.A.J. and B.B.L

Abstract

Neural activity during development critically shapes postnatal wiring of the mammalian brain. This is best illustrated by the sensory systems, in which the patterned feed-forward excitation provided by sensory organs and experience drives the formation of mature topographic circuits capable of extracting specific features of sensory stimuli^{1,2}. In contrast, little is known about the role of early activity in the development of the basal ganglia, a phylogenetically ancient group of nuclei fundamentally important for complex motor action and reward-based learning^{3,4}. These nuclei lack direct sensory input and are only loosely topographically organized^{5,6}, forming interlocking feed-forward and feed-back inhibitory circuits without laminar structure. Here we use transgenic mice and viral gene transfer methods to modulate neurotransmitter release and neuronal activity *in vivo* in the developing striatum. We find that the balance of activity between the two inhibitory and antagonist pathways in the striatum regulates excitatory innervation of the basal ganglia during development. These effects indicate that the propagation of activity through a multi-stage network regulates the wiring of the basal ganglia, revealing an important role of positive feedback in driving network maturation.

Introduction, Results & Discussion

Excitatory input from the cortex and thalamus enters the basal ganglia through the striatum, where it is locally processed and transformed into two inhibitory, GABAergic outputs called the direct and indirect pathways⁷. Each pathway arises from a distinct class of spatially intermixed medium spiny neurons (MSNs) with differing projections and molecular characteristics⁸. These projection patterns suggest opponent effects on basal ganglia output: direct pathway MSNs form synapses in substantia nigra reticulata (SNr), the basal ganglia output nucleus, whereas indirect pathway MSNs form synapses in globus pallidus (GP), which in turn inhibits the SNr⁹. Because the SNr provides GABAergic inhibition to the thalamus, which subsequently activates cortex through glutamatergic synapses, the interactions of basal ganglia, thalamus and cortex can be simplified as a closed loop, differentially controlled by the direct and indirect pathways (Figure 3.1). Anatomical evidence supports this model^{10,11} and the opponent roles of the two pathways on motor behaviour have been recently demonstrated in adult rodents^{12,13}. In addition, *in vivo* recordings and circuit tracing indicate that different cortico-striatal inputs are processed through segregated, parallel networks^{6,10,11,14}. Given this organization, establishing correct wiring of the cortex-basal ganglia–thalamus circuitry poses a significant developmental challenge, requiring that functional interactions be maintained over polysynaptic networks comprised of mixed inhibitory and excitatory projections.

Figure 3.1. Schematic of cortex-BG-thalamus circuitry illustrating the impact of perturbing GABA release in the direct or indirect pathway.

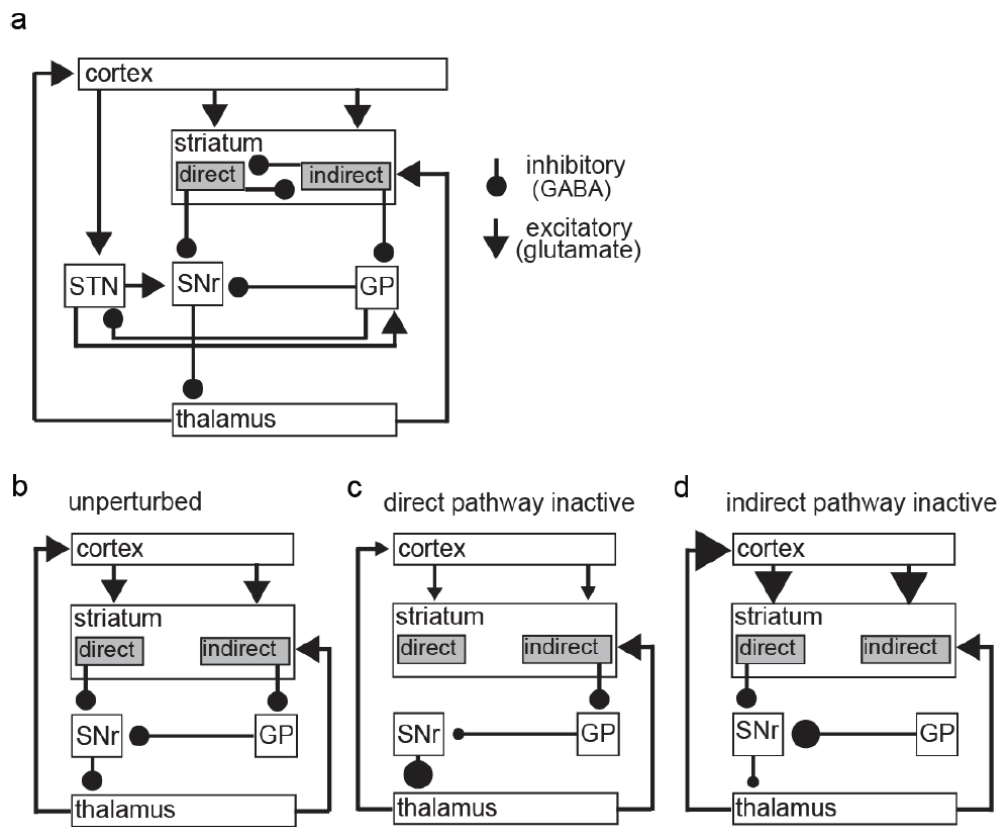
a. Diagram showing basic inhibitory and excitatory connections intrinsic to the basal ganglia nuclei and the major inputs and outputs to/from the cortex and thalamus. For simplicity, only the reciprocal inhibitory connections between direct and indirect pathway MSNs are shown, omitting the many reciprocal feedback connections between nuclei. Inhibitory synapses are indicated by circles, excitatory synapses are marked by arrows.

b. A highly simplified BG circuit model based on canonical connections shown in **(a)**. Activity of direct pathway MSNs inhibits the SNr and hence disinhibits the thalamus and cortex. In contrast, activity of the indirect pathway inhibits the GP, which disinhibits the SNr, hence decreasing activity of thalamus and cortex.

c. Circuit models of BG predict that silencing the direct pathway output increases inhibition of the thalamus, consequently decreasing excitation of cortex and striatum.

d. In contrast, silencing the indirect pathway is expected to decrease inhibition of the thalamus, increasing excitation of cortex and striatum. Although the diagrams in **b-d** are highly over-simplified, consideration of additional elements such as the STN does not alter the signs of the predicted effects on cortico-striatal activity.

Figure 3.1 (Continued)



To investigate how striatal activity contributes to circuit development, we generated mice incapable of releasing GABA from direct or indirect pathway MSNs through conditional knockout of *Slc32a1*, which encodes the vesicular GABA transporter (VGAT) (Figure 3.2)¹⁵. GABAergic neurons lacking VGAT are unable to package GABA into synaptic vesicles for release^{16,17}. Pathway specificity was conferred by bacterial artificial chromosome (BAC) transgenic mice that express Cre recombinase under the control of the type 1a or type 2 dopamine receptors¹⁸. In *Drd1a* Cre (D1-Cre) mice, Cre expression in GABAergic neurons is largely limited to direct pathway MSNs, although Cre is also found in non-GABAergic cortical neurons (Figures 3.2a, 3.3 and 3.4). In *Drd2* Cre (D2-Cre) mice, Cre expression is largely limited to indirect pathway MSNs (Figures 3.2a and 3.3). Mice with *Slc32a1* deletion in direct or indirect pathway MSNs showed opposing locomotor phenotypes and survived until weaning (Figure 3.5), a time of increasing reliance on reward-based complex motor actions.

To test the efficacy of silencing of GABA release we relied on optogenetic analysis of MSN-to-MSN collateral synapses¹⁹. Channelrhodopsin2–mCherry fusion protein (ChR2–mCherry) was expressed in Cre-positive MSNs by injecting an adeno-associated virus (AAV) containing a double floxed inverted ChR2–mCherry transgene into the striatum at postnatal (P) days 3–5 (Figure 3.2b)²⁰. Whole-cell voltage-clamp recordings of ChR2-negative MSNs demonstrated light-evoked GABAergic currents in acute brain slices from P13–18 *D1-cre;Slc32a1^{f/+}* mice ($-1,477 \pm 352$ pA, $n = 20$) and *D2-cre;Slc32a1^{f/+}* mice ($-1,319 \pm 221$ pA, $n = 12$); these currents were absent in littermate

Slc32a1^{ff} mice (*D1-cre;Slc32a1^{ff}*, -2.19 ± 1.6 pA, $n = 7$; *D2-cre;Slc32a1^{ff}*, -9.91 ± 2.4 pA, $n = 7$) (Figures 3.2c and 3.6).

Figure 3.2 Conditional knock out of *Slc32a1* from direct or indirect pathway MSNs abolishes GABAergic output.

a. Cre expression driven by *Drd1a* (D1-Cre, *top*) and *Drd2* (D2-Cre, *bottom*) BACs was visualized via activation of TdTomato in a reporter mouse. Red fluorescence reveals expression throughout striatum and in axons in expected target nuclei of direct and indirect pathway MSNs (SNr and GP, respectively). Green fluorescence reflects expression of a GAD67-GFP that reports GABAergic neurons. As seen in the red channel, there is diffuse cortical expression of Cre in the D1-Cre mice; however, this occurs in non-GABAergic neurons as noted by the lack of overlap with GFP fluorescence (see Figure 3.3 for complete analysis). Scale bar: 500 μm .

b. AAV DIO-ChR2-mCherry injected into the striatum of a mouse carrying D2-Cre and D2-GFP transgenes shows ChR2-mCherry labeling in GFP⁺ cells, indicating pathway specific conditional expression of the virally encoded protein. ChR2-mCherry-expressing somata are marked with an asterisk and represent over 2/3 of the GFP⁺ MSNs in the area of dense infection. ChR2-mCherry was never observed in D2-GFP⁻ MSNs in these mice. Scale bar: 10 μm .

c. Voltage-clamp recordings from ChR2-mCherry⁻ MSNs demonstrate GABAergic synaptic currents evoked by 2 ms-long pulses of 473 nm light that stimulates neighboring ChR2-mCherry⁺ MSNs. Example currents from MSNs in D1-Cre (*left*) and D2-Cre (*right*) mice that were either homozygous (gray, *Slc32a1^{ff}*) or heterozygous (black, *Slc32a1^{ff/+}*) for the *Slc32a1* conditional allele are shown. GABAergic currents are inward due to high intracellular Cl⁻ concentration. *Insets*, graphs of average peak current

Figure 3.2 (Continued)

amplitudes evoked in animals of each genotype. * indicates $p < 0.05$ for comparison of *Slc32a1*^{f/+} and *Slc32a1*^{f/f} data.

Figure 3.2 (Continued)

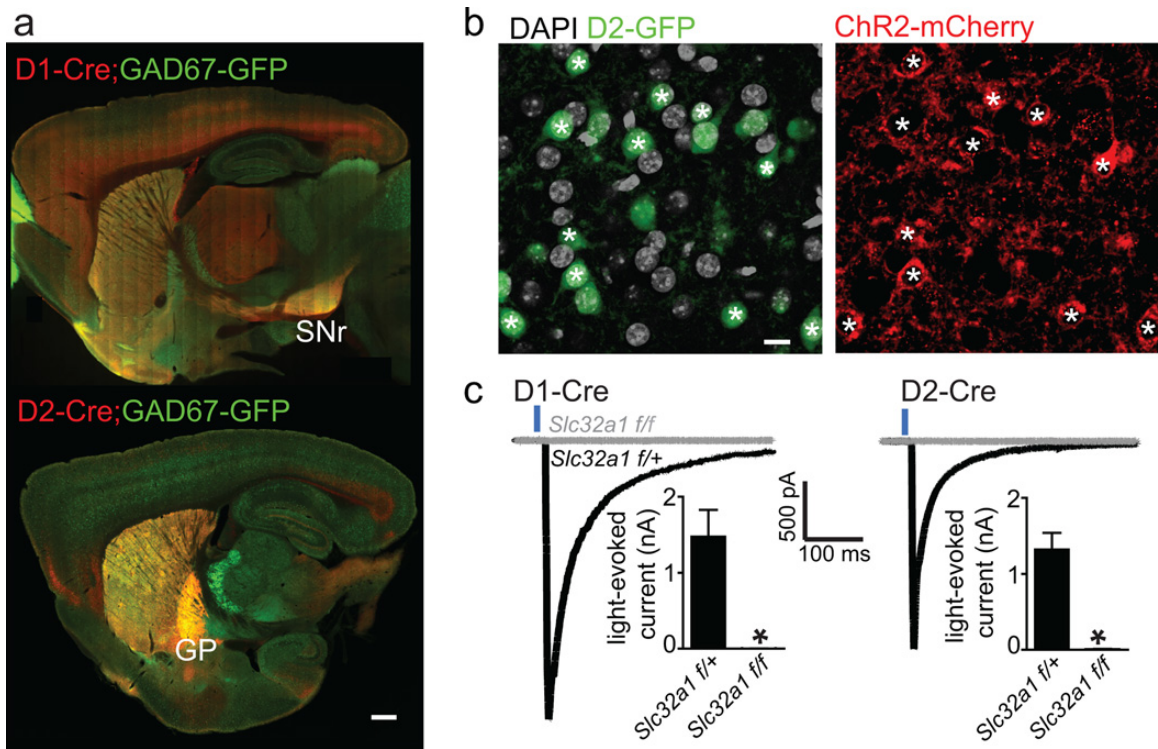


Figure 3.3. Whole-brain anatomical mapping of D1- and D2-Cre expression in inhibitory neurons.

a. Triple transgenic mice were generated carrying the D1- or D2-Cre transgene, a red fluorescent Cre reporter allele (*Ai14-*Isl*-tdTomato*), and a *GAD67-GFP* knock-in allele to label GABAergic neurons in green and Cre-expressing neurons in red³⁷. Example shows a sagittal section from a *D1-Cre; Ai14-*Isl*-tdTomato; GAD67-GFP* brain.

b. D1-Cre is expressed predominantly in the striatum and to a lesser extent in the cerebral cortex. Striatal Cre expression (inset 1) occurs in GABAergic cells, consistent with D1-Cre expression in direct pathway MSNs. Cortical Cre expression is largely restricted to non-GABAergic cells, as shown for medial prefrontal (inset 2) and somatosensory cortex (inset 3).

c. A single sagittal section from a *D2-Cre; Ai14-*Isl*-tdTomato; GAD67-GFP* brain.

d. D2-Cre is expressed predominantly in striatum and to a lesser extent in cerebellum. Striatal Cre expression occurs in GABAergic cells, consistent with D2-Cre expression in indirect pathway MSNs. Cerebellar Cre is expressed mainly in a subset of GABAergic Purkinje neurons (inset 2). Scale bars: whole brain images, 500 μm ; insets, 50 μm .

Figure 3.3 (Continued)

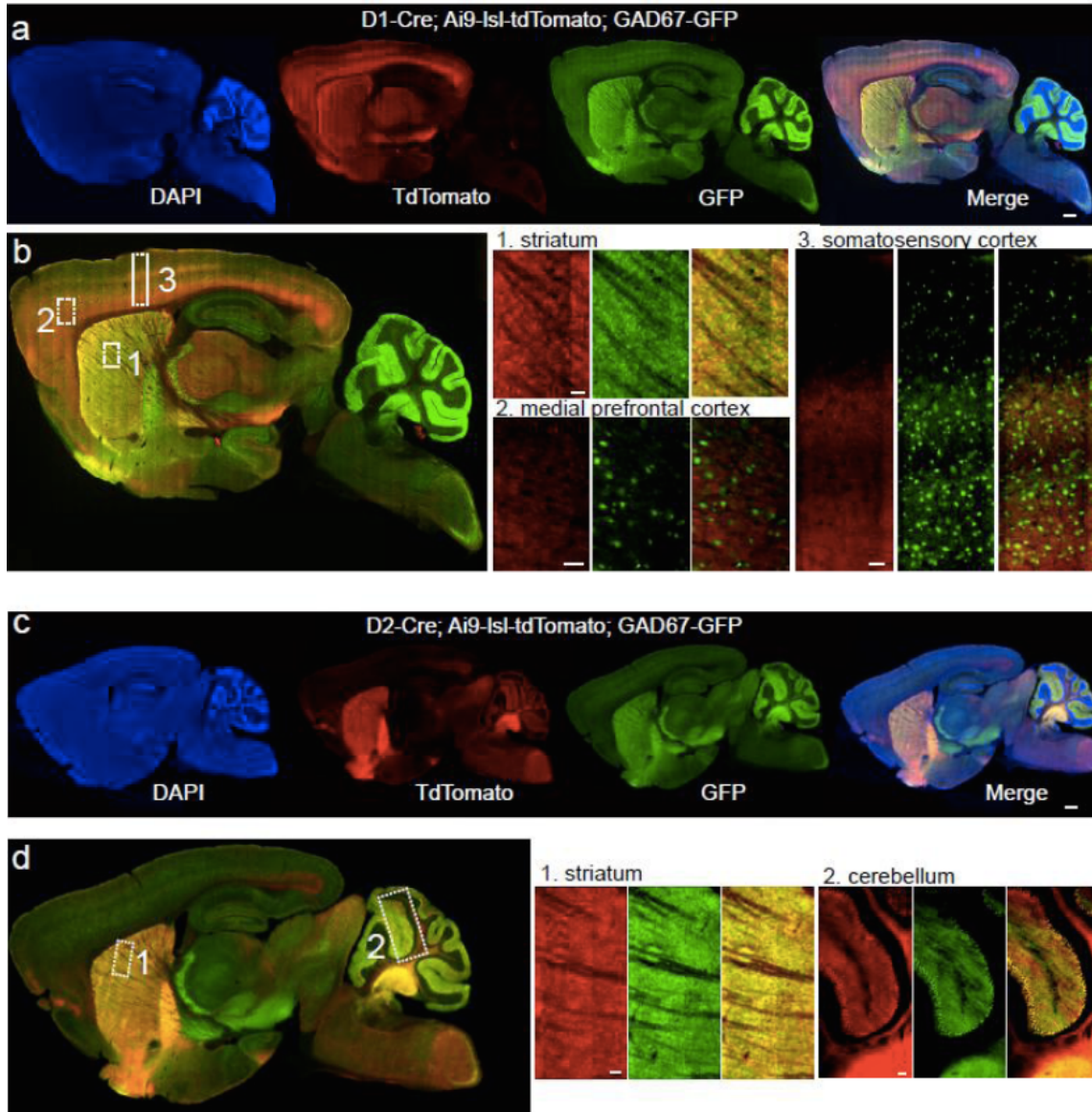


Figure 3.4. D1-Cre is not expressed in the vast majority of parvalbumin positive neurons in the striatum.

a. A single sagittal section from a *D1-Cre;Ai14-IsI-tdTomato* animal immunostained for Parvalbumin.

b. A single confocal plane illustrating the lack of co-expression of Parvalbumin and D1-Cre. Confocal imaging of 339 Parvalbumin positive neurons from 4 animals revealed only 1 that expressed TdTomato. Scale bars: whole brain images, 500 μm ; confocal images, 50 μm . * indicates three representative cells that are clearly PV positive and TdTomato negative.

Figure 3.4 (Continued)

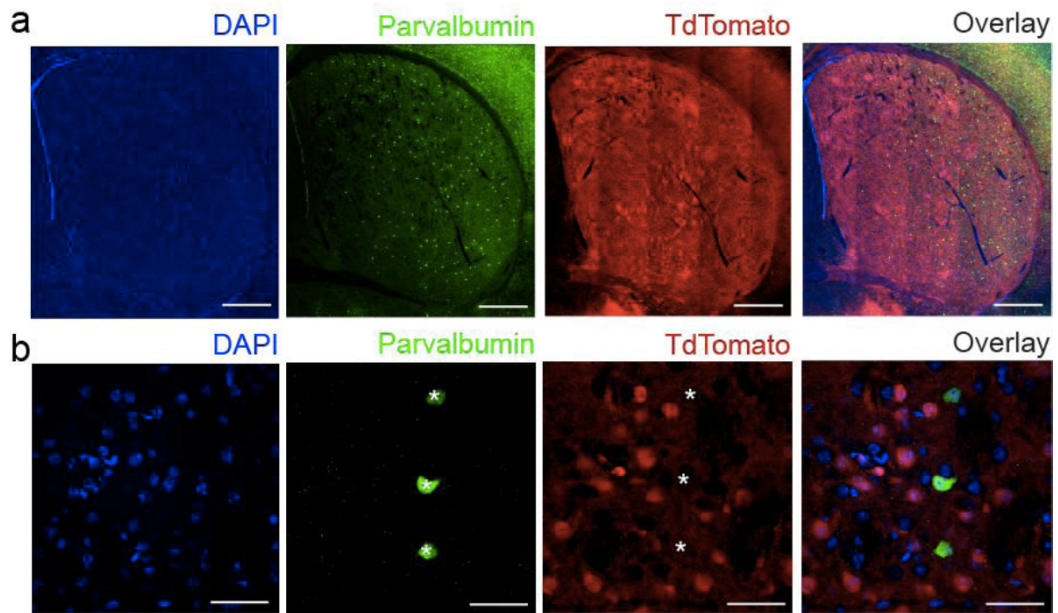


Figure 3.5. Phenotypes of mice with conditional knock out of *Slc32a1* in direct or indirect pathway MSNs.

a. Photographs of P12 siblings from crosses of D1- or D2-Cre mouse lines with a floxed *Slc32a1* mouse line. Arrows point to *Slc32a1*^{ff} littermates.

b. Weight curves for postnatal week 2-3 mice. Both *D1-Cre; Slc32a1*^{ff} and *D2-Cre; Slc32a1*^{ff} mice fail to gain weight starting in postnatal week 2 (n=6-8 mice/group). * indicates $p < 0.05$ for main effects and post hoc comparisons across genotypes.

c. *left*, survival curves for *D1-Cre* and *D2-Cre; Slc32a1*^{ff} mice. *Slc32a1*^{f/+} controls survived at 100% during this period (not shown). *D1-Cre; Slc32a1*^{ff} mice died earlier than *D2-Cre; Slc32a1*^{ff} mice. *right*, average survival in days for direct and indirect pathway silenced mice (n=5-8 mice/group). * indicates $p < 0.05$ for comparison of direct and indirect pathway *Slc32a1* nulls.

d. View from the top of the arena (gray) used to test locomotor activity with examples of tracks for individual mice of each genotype (red).

e. Average distance traveled in 1 hr is shorter in direct pathway *Slc32a1* null mice compared to paired littermate controls. In contrast, indirect pathway *Slc32a1* null mice travelled a longer distance compared to respective controls (n=6-8 mice/group).

Figure 3.5 (Continued)

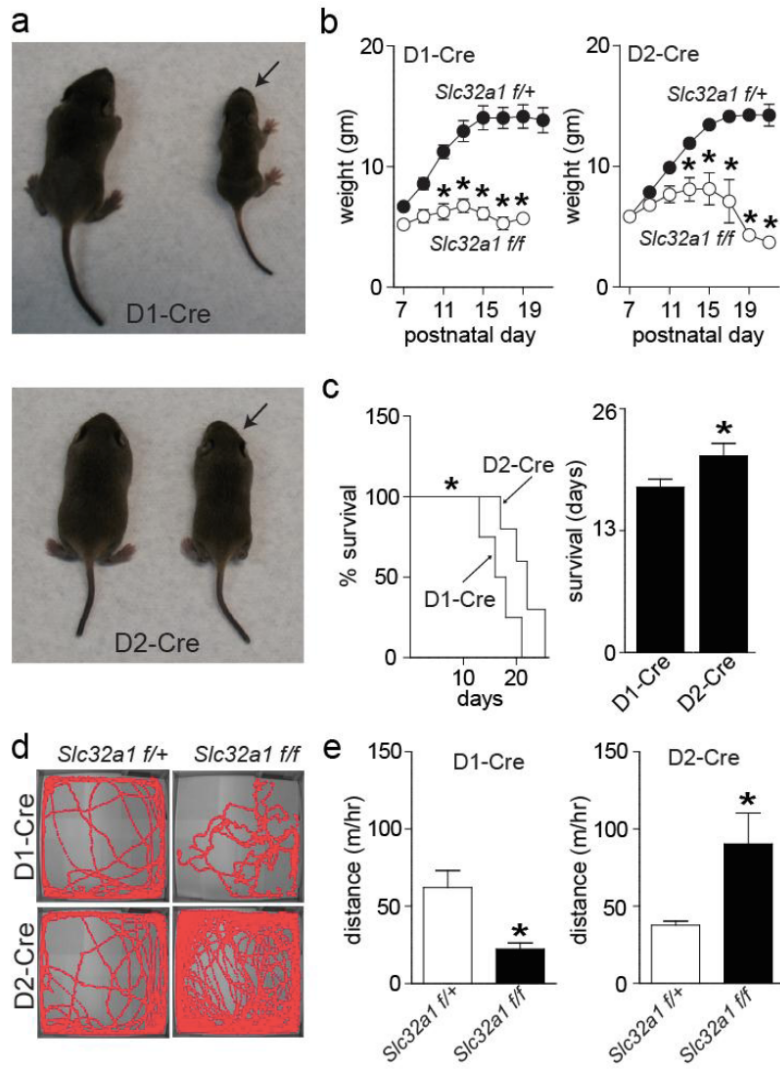


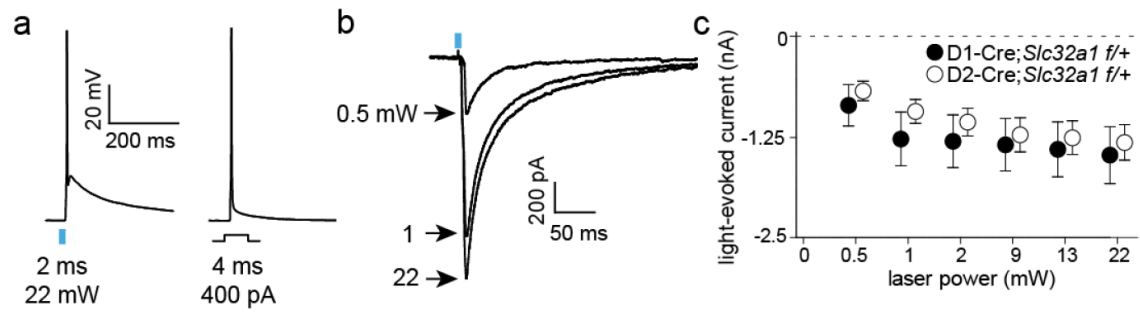
Figure 3.6. Optogenetic activation of MSNs of direct and indirect pathways.

a. ChR2-mCherry was introduced into direct or indirect pathway MSNs through infection of D1-Cre or D2-Cre mice with AAV DIO-ChR2-mCherry. A ChR2⁺ MSN produces a single time-locked action potential in response to optical activation (2 ms-long pulse at 20 mW of whole-field 473 nm light illumination) or a 400 pA 4 ms-long somatic current injection. Note the typical after-spike depolarization characteristic of ChR2-induced firing.

b. Voltage-clamp recordings ($V_{\text{hold}} = -70$ mV) with high-Cl internal ($E_{\text{Cl}} \sim 0$ mV) and CPP, NBQX and scopolamine in the bath were made from ChR2⁻ MSNs neighboring ChR2⁺ MSNs. An example recording demonstrates inhibitory postsynaptic currents evoked by stimulation with different light intensities.

c. Average peak current amplitudes from *D1-Cre; Slc32a1^{f/+}* and *D2-Cre; Slc32a1^{f/+}* MSNs (n=20 and 12). Evoked synaptic currents reach their maximal amplitudes by 2-9 mW.

Figure 3.6 (Continued)



We examined whether GABA release from MSNs is required for cell survival and long-range axonal projections. The proportion of Cre⁺ cell nuclei was 45–48% in D1-Cre and D2-Cre mice and independent of the number of conditional *Slc32a1* alleles (Figure 3.7). MSNs lacking GABA release form qualitatively normal long-range axonal projections, on the basis of examination of ChR2–mCherry fluorescence in the SNr and GP (SNr, 18–19%; GP, 15–16% fractional area coverage) (Figure 3.8). These observations confirm that MSNs lacking GABA release are maintained in normal numbers and extend grossly normal axons.

In contrast, silencing GABA release had profound consequences on the number of excitatory synapses received, which are typically associated with dendritic spines^{21,22}. In the rodent striatum, inhibitory synapse density is relatively constant throughout postnatal development, whereas excitatory synapse density rises markedly between P10 and P21²³. Therefore, we restricted analyses to pairs of littermate control and *Slc32a1* null mice at P14–15. We identified MSNs of each pathway using ChR2–mCherry expression delivered by either Cre-On or Cre-Off AAVs (Figure 3.9a)²⁴. Even within this narrow developmental window, we detected an increase in miniature excitatory postsynaptic current (mEPSC) frequencies, but not amplitudes, among littermates of the same genotype (frequency: P14, 0.14 ± 0.06 Hz; P15, 0.34 ± 0.1 Hz; amplitude: P14, 14.4 ± 1.0 pA; P15, 13.9 ± 0.4 pA) (Figure 3.9b). In mice lacking GABA release in direct pathway MSNs, mEPSC frequency was reduced in both direct and indirect pathway MSNs compared to heterozygous sibling controls

Figure 3.7. GABA release is not required for MSN survival.

a. Confocal photomicrographs illustrating the pattern of Cre immunolabeling in the indicated genotypes (Cre, green; DAPI, blue). Scale bar: 20 μm .

b. The proportion of Cre⁺ and Cre⁻ DAPI nuclei matches the expectation for D1 and D2 MSNs (~40-50%) and does not depend on the presence of a functional *Slc32a1* allele (n=3-4 mice/group, 6-7 brain sections and >600 cell bodies examined in each mouse).

Figure 3.7 (Continued)

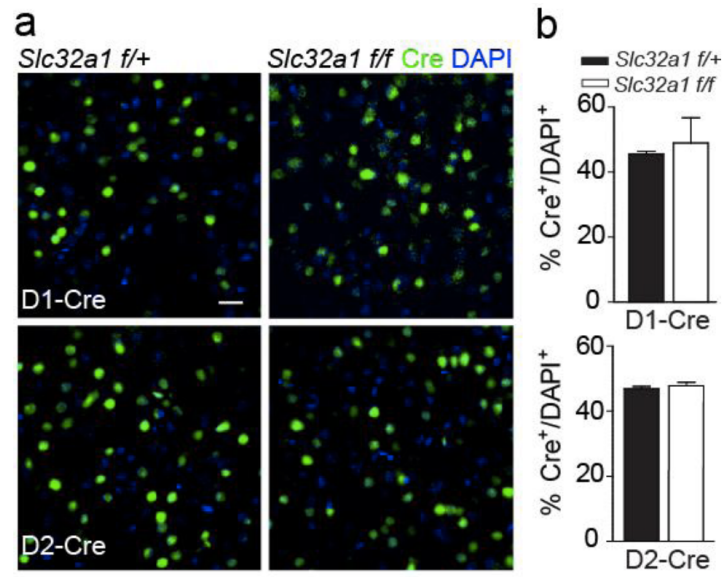


Figure 3.8. GABA release is not required for the development of long-range axonal projections.

a. ChR2-mCherry was introduced into direct or indirect pathway MSNs through infection of AAV DIO-ChR2-mCherry. Schematic illustrates the injection location and expected projections.

b. Low magnification images show fluorescence in the expected target nuclei for *Slc32a1* null mice and respective controls (SNr for direct pathway MSNs, GP for indirect pathway MSNs). Scale bar: 250 μm .

c. Confocal photomicrographs of ChR2-mCherry⁺ axonal puncta in the expected target nuclei. Scale bar: 20 μm .

d. Area fraction fluorescence, estimated based on binarized confocal images, did not differ across genotypes (n=9-18 brain sections from 3-4 mice/group).

Figure 3.8 (Continued)

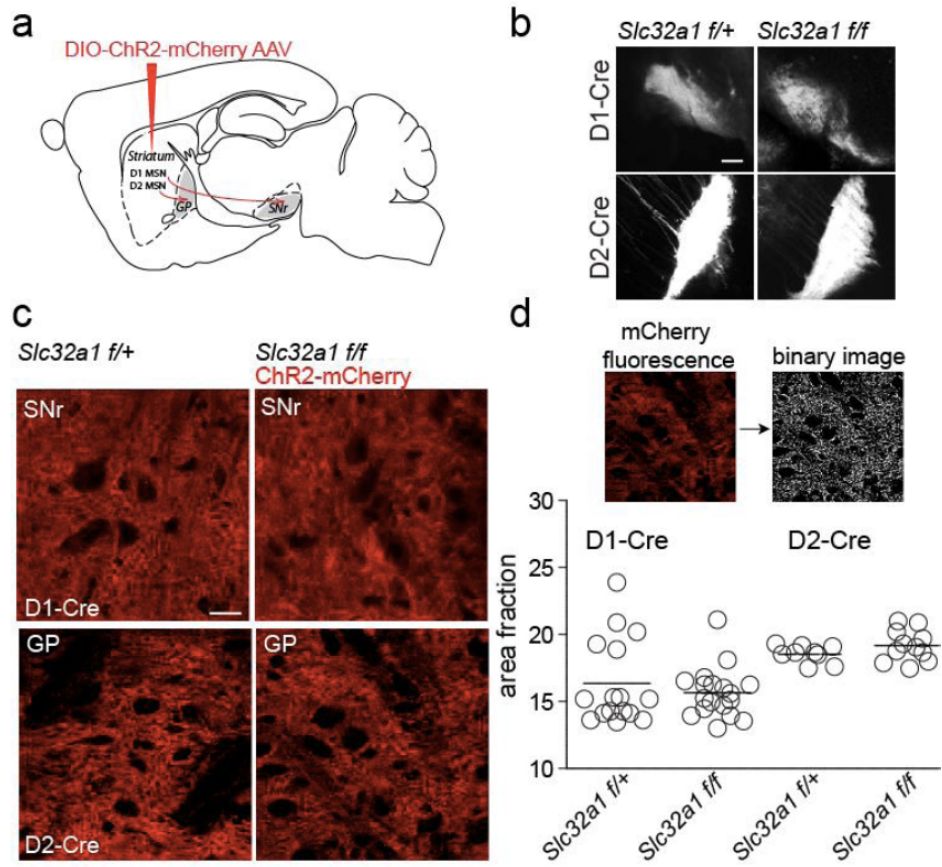


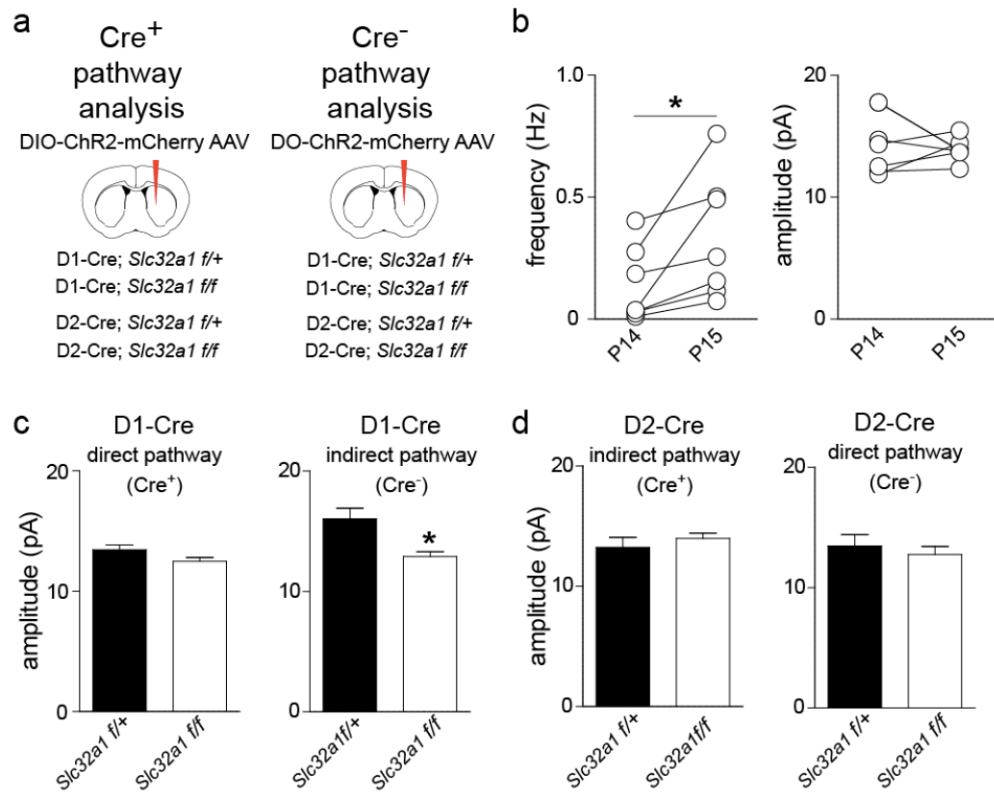
Figure 3.9. Spontaneous mEPSCs in direct and indirect pathway MSNs of mice with conditional knockout of *Slc32a1*.

a. Chr2-mCherry was selectively introduced into direct or indirect medium spiny neurons through infection of AAV DIO-ChR2-mCherry. For examining Cre⁻ pathway, Cre-Off DO-ChR2-mCherry AAV was used instead. A schematic for the analyses of direct and indirect pathway in animals with 0 or 1 functional copy of *Slc32a1* allele is shown.

b. For several experiments, data from different siblings of the same genotype and experimental group were compared on P14 and P15, controlling for MSN class and experiment type. Each data point reflects an averaged parameter from several cells of the same class recorded in the same animal. mEPSC frequency rates are significantly increased at P15 relative to P14 (* indicates $p < 0.05$ for comparison of P14 and P15 mEPSC frequencies, $n = 7$ experiments), implying increased number of excitatory synapses, while amplitudes of currents remain unchanged. Because of this pronounced change within a narrow 24 hr developmental window, mEPSC frequency data are presented normalized to respective controls.

c. For direct pathway manipulated mice, the amplitude of mEPSCs in direct pathway MSNs did not significantly differ between siblings with 1 or 0 functional copy of *Slc32a1* in the direct pathway MSN ($n = 14-17$ cells/group), but was decreased in the indirect pathway of direct pathway *Slc32a1* null MSNs (* indicates $p < 0.05$ for comparison of Cre⁻ pathway in D1-Cre mice, $n = 16-18$ cells/group). For indirect pathway manipulated mice, the amplitudes of mEPSCs did not differ across genotypes ($n = 5-14$ cells/group).

Figure 3.9 (Continued)



(direct pathway MSNs: *D1-cre;Slc32a1^{f/+}*, 0.22 ± 0.04 Hz, $n = 18$; *D1-cre;Slc32a1^{f/f}*, 0.08 ± 0.02 Hz, $n = 16$; indirect pathway MSNs: *D1-cre;Slc32a1^{f/+}*, 0.32 ± 0.07 Hz, $n = 14$; *D1-cre;Slc32a1^{f/f}*, 0.1 ± 0.03 Hz, $n = 15$) (Figure 3.10a,c). Conversely, mEPSC frequency was increased in MSNs of mice with output-silenced indirect pathway (direct pathway MSNs: *D2-cre;Slc32a1^{f/+}*, 0.11 ± 0.04 Hz, $n = 9$; *D2-cre;Slc32a1^{f/f}*, 0.28 ± 0.07 Hz, $n = 6$; indirect pathway MSNs: *D2-cre;Slc32a1^{f/+}*, 0.15 ± 0.06 Hz, $n = 5$; *D2-cre;Slc32a1^{f/f}*, 0.37 ± 0.04 Hz, $n = 14$) (Figure 3.10b,d). mEPSC amplitudes were largely unaffected by either manipulation (Figure 3.9c,d).

Changes in mEPSC rates were paralleled by alterations in dendritic spine density, indicating concurrent changes in structural and functional correlates of excitatory synapse number. Dendritic spine density of all MSNs was decreased by silencing the direct pathway (direct pathway MSNs: *D1-cre;Slc32a1^{f/+}*, 0.84 ± 0.03 spines per μm , $n=6$; *D1-cre;Slc32a1^{f/f}*, 0.45 ± 0.05 spines per μm , $n = 7$; indirect pathway MSNs: *D1-cre;Slc32a1^{f/+}*, 0.68 ± 0.05 spines per μm , $n = 5$; *D1-cre;Slc32a1^{f/f}*, 0.41 ± 0.02 spines per μm , $n = 5$) and increased by silencing the indirect pathway (direct pathway MSNs: *D2-cre;Slc32a1^{f/+}*, 0.41 ± 0.02 spines per μm , $n = 6$; *D2-cre;Slc32a1^{f/f}*, 0.63 ± 0.08 spines per μm , $n = 6$; indirect pathway MSNs: *D2-cre;Slc32a1^{f/+}*, 0.56 ± 0.03 spines per μm , $n = 5$; *D2-cre;Slc32a1^{f/f}*, 1.02 ± 0.05 spines per μm , $n = 6$) (Figure 3.10). Together these data show that the degree of excitatory innervation of MSNs is determined by striatal output, such that excitatory hypo- or hyper-innervation is triggered by silencing the direct or indirect pathway, respectively.

Figure 3.10. Conditional knock out of *Slc32a1* in direct and indirect pathway MSNs results in opposing changes to excitatory synapse number.

a. *left*, 2PLSM image of a direct pathway *Slc32a1^{f/+}* MSN filled with Alexa Fluor 594 through the recording pipette during whole-cell voltage-clamp analysis of mEPSCs. *right*,

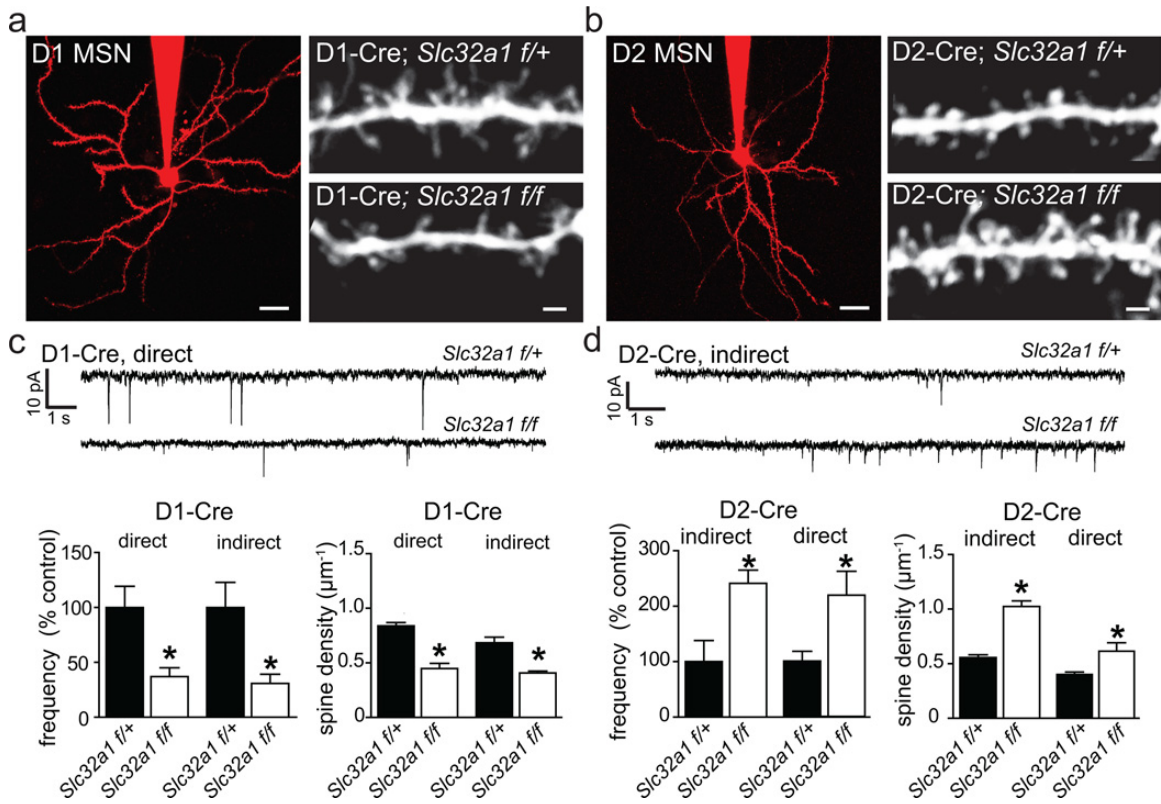
At a higher magnification, dendritic spines are visible. Examples of a dendrite from a control direct pathway MSN (*top*) and of a less spiny dendrite from a direct pathway MSN of a *Slc32a1* null sibling (*bottom*) are shown. Scale bars: 20 μm , 2 μm .

b. As in (**a**), but illustrating the increase in dendritic spine density seen with silencing of indirect pathway MSNs.

c. Examples and summary of frequencies of mEPSCs in direct pathway *Slc32a1* null mice and their heterozygous sibling controls. Preventing GABA release from direct pathway MSNs reduced mEPSCs frequency, compared to direct pathway MSNs in *Slc32a1^{f/+}* sibling controls (*top*). Summary graph illustrates the decrease in direct and indirect pathway MSNs that were paralleled by differences in the density of dendritic spines. * indicates $p < 0.05$ for comparison of *Slc32a1^{f/+}* and *Slc32a1^{f/f}* data.

d. As in (**c**) for indirect pathway mutants indicating that preventing GABA release from indirect pathway MSNs increased mEPSC frequency and dendritic spine density in indirect and direct pathway MSNs. * indicates $p < 0.05$ for comparison of *Slc32a1^{f/+}* and *Slc32a1^{f/f}* data.

Figure 3.10 (Continued)



Complementary, pathway-dependent effects on excitatory input could be due to cell-intrinsic differences in direct and indirect pathway MSNs. Alternatively, common activity-dependent wiring rules could be differentially activated by each perturbation of basal ganglia output. For example, a net increase in SNr inhibitory output, caused by silencing direct pathway MSNs, could diminish thalamic and cortical activity, decreasing glutamate release and glutamatergic synapse formation in the striatum. In contrast, silencing the indirect pathway could have the converse set of effects (Figure 3.1b–d). The observation that direct or indirect pathway MSNs show similar perturbations despite selective deletion of *Slc32a1* only in MSNs of the Cre-expressing pathway (Figure 3.10) provides support for the circuit-level model.

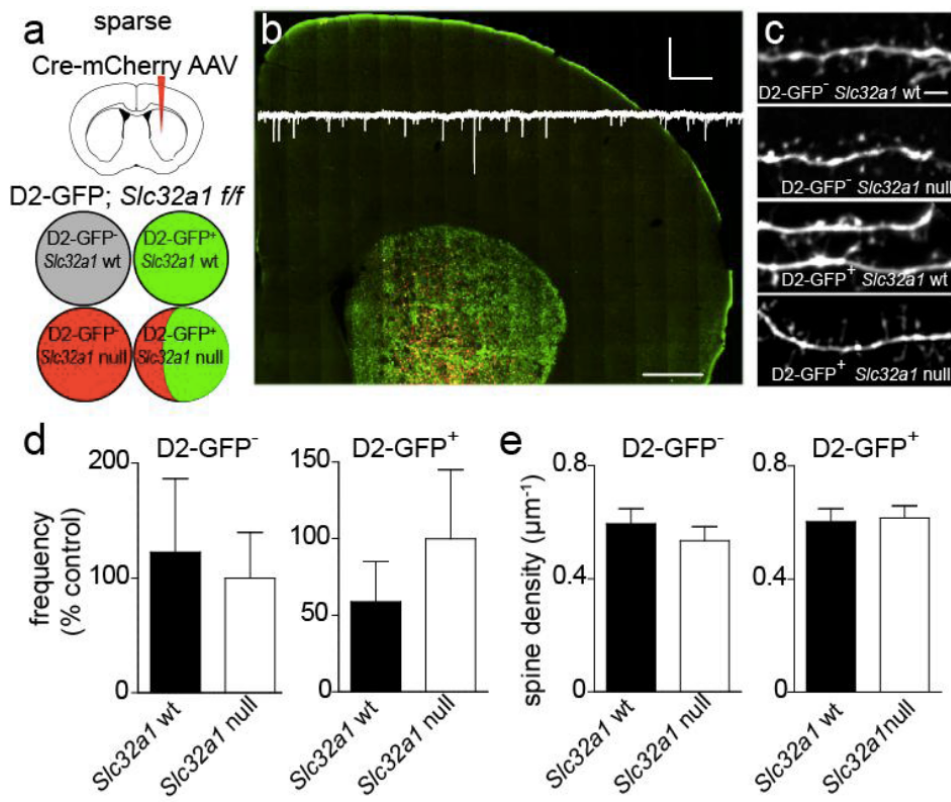
To test for cell-autonomous, *Slc32a1*-dependent regulation of glutamatergic innervation, we deleted *Slc32a1* in a small and sparse subpopulation of striatal neurons by injecting small quantities of AAV encoding Cre–mCherry into *D2-GFP;Slc32a1^{ff}* mice at P0–1 (Figure 3.11a, b). Analysis of mEPSCs and dendritic spines in neighbouring Cre⁺ and Cre⁻ MSNs (identified by nuclear mCherry fluorescence) belonging to the direct and indirect pathway (identified by GFP expression) revealed no changes in mEPSC frequency or dendritic spine density (Figure 3.11c–e). Thus, *Slc32a1*-dependent, cell-intrinsic mechanisms are unlikely to contribute to differential effects on glutamatergic innervation seen with silenced direct or indirect pathways.

We examined the consequences of manipulating striatal activity specifically during the period of striatal excitatory synaptogenesis²³ using the RASSL (G-protein-coupled receptor activated solely by a synthetic ligand) hM4D^{25,26} in direct or indirect

Figure 3.11. Sparse postnatal *Slc32a1* deletion does not alter the frequency of mEPSCs or density and morphology of dendritic spines in MSNs.

- a.** Schematic of the experiment. To examine the possibility that *Slc32a1* has cell-type-intrinsic functional implications for direct and indirect pathway MSNs, we postnatally deleted *Slc32a1* in small populations of both pathway MSNs in *Slc32a1^{fl/fl}* animals through low titer Cre-mCherry AAV infection at P0-1.
- b.** Coronal section through a brain hemisphere showing the spread of mCherry-Cre infection in the D2-GFP striatum. Inset shows a representative mEPSC trace recorded in a D2-GFP⁻, Cre-mCherry⁻ control direct pathway MSN. Scale bar: image, 500 μ m; mEPSC trace, 200 pA and 1 sec.
- c.** 2PLSM of dendrites confirms the identity of recorded neurons as MSNs and enables the estimation of dendritic spine density and shape. Scale bar: 2 μ m.
- d.** Recordings of spontaneous mEPSCs in mCherry fluorescent regions of striatum were performed in nearby Cre⁺ and Cre⁻ neurons in the same slice. There were no differences in frequency or amplitude of mEPSCs in direct or indirect pathway MSNs when only a small population of neurons were prevented from releasing GABA (n=6-7 cells/group).
- e.** This lack of difference in mEPSCs was paralleled by absence of differences in dendritic spine density for direct or indirect pathway MSNs that were *Slc32a1* floxed or *Slc32a1* null, when large-scale circuit activity was relatively unperturbed (n=5 cells/group).

Figure 3.11 (Continued)



pathway MSNs ([Figure 3.12](#)). hM4D is activated by a blood–brain barrier permeable molecule clozapine-*n*-oxide (cno), allowing non-invasive *in vivo* manipulation of neural activity. hM4D couples to the $G_{i/o}$ pathway, which reduces action potential firing in many cell types ([Figure 3.13](#)) by activating K^+ channels¹³. AAV carrying the double floxed inverted hM4D–mCherry transgene²⁶ was injected in D1-Cre or D2-Cre mice at P0–1 and, starting at P8, cno (1 mg kg^{-1}) or saline was administered subcutaneously twice per day to littermate pups. Consistent with our hypothesis, animals with large bilateral injections of AAV to dampen activity of many direct or indirect pathway MSNs, respectively, down- or upregulated mEPSC frequency and dendritic spine density, relative to saline-injected littermates (*D1-cre*, direct pathway MSNs: frequency, saline $0.8 \pm 0.1 \text{ Hz}$, $n = 18$; cno $0.36 \pm 0.07 \text{ Hz}$, $n = 25$; spine density, saline 0.96 ± 0.04 spines per μm , $n = 5$; cno 0.49 ± 0.05 spines per μm , $n = 5$; *D2-cre*, indirect pathway MSNs: frequency, saline $0.04 \pm 0.01 \text{ Hz}$, $n = 7$; cno, $0.27 \pm 0.09 \text{ Hz}$, $n = 8$; spine density, saline 0.54 ± 0.05 spines per μm versus, $n = 5$; cno 0.98 ± 0.06 spines per μm , $n = 5$) ([Figure 3.12a–c](#) and [Figure 3.14a](#)). Similar results were observed with the *Adora2a-cre* mouse, based on the adenosine 2A receptor promoter, another Cre driver line for indirect pathway MSNs ([Figure 3.15](#)).

In contrast, sparse, unilateral hM4D delivery, designed to have a minimal impact on circuit dynamics, did not alter mEPSC frequency and dendritic spine density in hM4D-expressing neurons relative to uninfected neighbouring MSNs of the same pathway ([Figure 3.12d–f](#) and [3.14b](#)). These data also indicate that hM4D-mediated

Figure 3.12. *In vivo*, developmentally-restricted postnatal manipulation of activity in direct and indirect pathway MSNs results in opposing changes to excitatory synapse number.

a. Schematic of experimental design and hypotheses for changes in excitatory synapse number induced by extensive and bilateral expression of hM4D in direct or indirect pathway MSNs and subsequent injections of cno or saline. Widespread inhibition of direct pathway MSN firing with cno is expected to decrease excitatory synapse number, whether circuit level or cell-intrinsic mechanisms dictate cortico-striatal synaptogenesis.

The converse is expected for widespread inhibition of indirect pathway MSNs.

b. *left*, hM4D-mCherry⁺ MSNs in tissue densely infected with hM4D-encoding AAV (mCherry, red; DAPI, blue). Scale bar: 20 μ m. ***right***, Summary data demonstrate that *in vivo* manipulation of neuronal activity in direct or indirect pathway MSNs in the time window of excitatory synaptogenesis led to opposing changes in excitatory synapse number. Decreased mEPSC frequency was observed in cno-treated D1-Cre mice, whereas mEPSC frequency was enhanced in cno-treated D2-Cre mice, compared to respective saline-injected controls. * indicates $p < 0.05$ for the comparison of same pathway MSNs from saline and cno-injected mice.

c. *left top*, 2PLSM images of a dendrite from a direct pathway MSN in a saline-injected mouse and a less spiny dendrite from a cno-injected sibling. Scale bar: 2 μ m. ***left bottom***, Images showing an example of increased spine density in indirect pathway MSNs of cno-treated animals compared to saline controls. ***right***, Summaries of spine density in cno- and saline-treated animals demonstrating the opposite sign changes

Figure 3.12 (Continued)

resulting from inhibition of the direct or indirect pathway. * indicates $p < 0.05$ for the comparison of same pathway MSNs from saline and cno-injected mice.

d. Schematic of experimental design and hypotheses for possible changes in excitatory synapse number induced by sparse and unilateral expression of hM4D in direct or indirect pathway MSNs and subsequent injections of cno. Manipulation of activity in a small subset of neurons is not expected to engage circuit-wide mechanisms regulating synapse numbers. In contrast, unknown cell-intrinsic mechanisms could regulate the number of synapses formed onto the manipulated neurons, compared to same pathway uninfected MSNs.

e. *left*, Confocal image showing an hM4D-mCherry expressing MSN in a sparse injection configuration (mCherry, red; DAPI, blue). Scale bar: 20 μm . *right*, With sparse activity manipulations, no differences in mEPSC frequency were observed in either direct or indirect pathway infected, compared to uninfected, MSNs.

f. *left top*, 2PLSM images of a dendrite from control or neighboring hM4D-expressing direct pathway MSN. Scale bar: 2 μm . *left bottom*, Images of spiny dendrites from control or neighboring hM4D-expressing indirect pathway MSN. *right*, Summary graph shows that inhibiting activity of a sparse subset of MSNs does not alter dendritic spine density in manipulated direct or indirect pathway neurons.

Figure 3.12 (Continued)

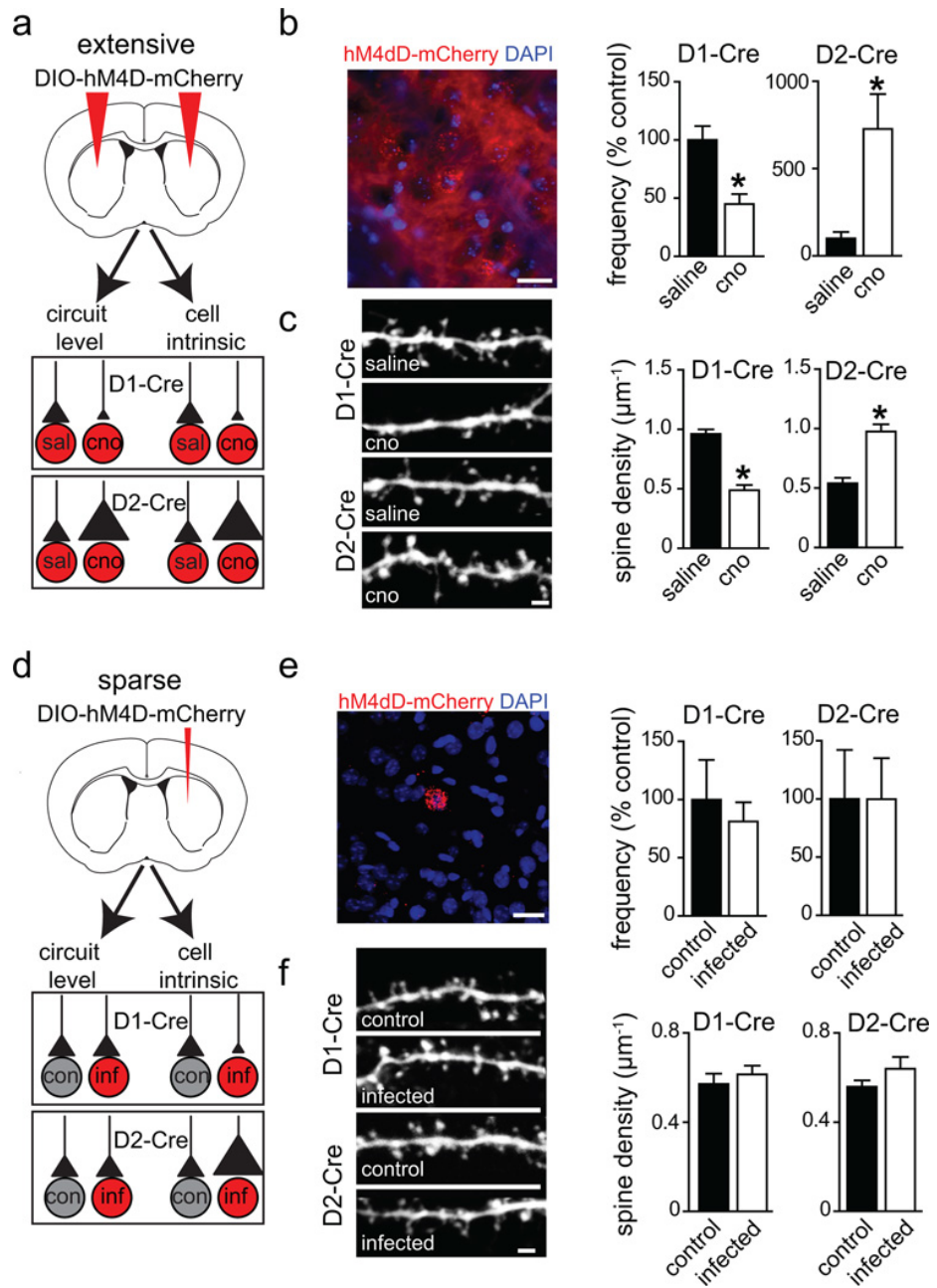


Figure 3.13. Cno application reduces optogenetically evoked spiking in MSNs and cortico-striatal projection neurons expressing hM4D-mCherry.

a. DIO Chr2-YFP and DIO-hM4D AAVs at approximately equal titers were injected into the striata of P1-3 mice carrying the D1-Cre or D2-Cre BAC transgenes or into the cortex of mice carrying the Rbp4-Cre BAC transgene. *right*, cell attached recordings were made from neurons of each class expressing both hM4D-mCherry and Chr2-YFP.

b. A 500 ms pulse of 473 nm laser light was delivered through a 60x objective. The strength of the laser light was slowly increased to achieve firing rates of 4 – 20 Hz. Laser light pulses were delivered every 20 or 30 seconds. After steady baselines were achieved (~5 minutes), cno (10 μ M) was added into the bath and firing rates were monitored in response to the same 500 ms laser pulse until no further changes in spiking were observed (~5– 20 minutes). In a subset of experiments, as illustrated, laser power was subsequently increased to examine if spiking could be returned to baseline levels even in the presence of cno.

c. *left*, Summary data for optogenetically evoked firing during the baseline and after cno was applied. For all three classes of neurons expressing hM4D, 10 μ M cno reduced firing rates (average of 5 baseline and cno trials) and this reduction was not significantly different across cell classes (*right*).

Figure 3.13 (Continued)

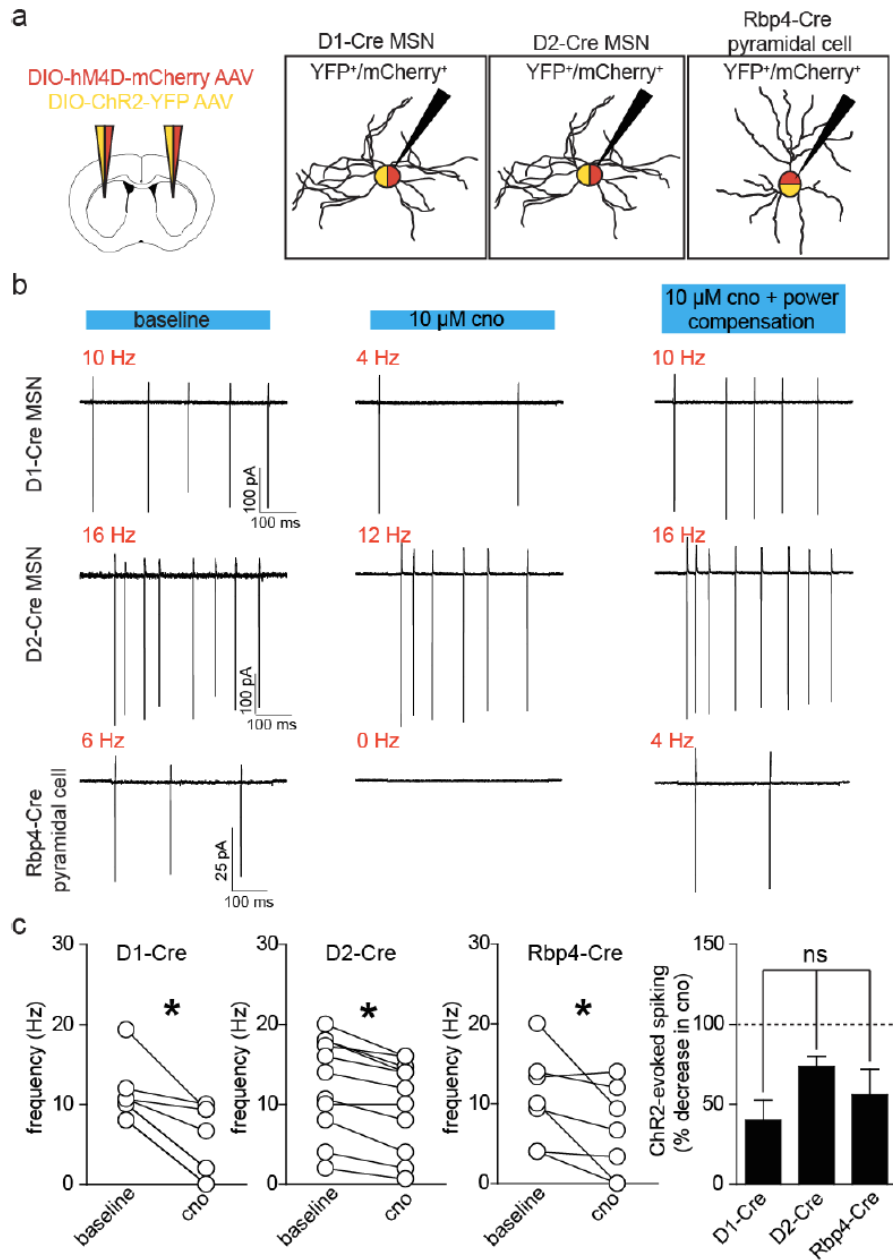


Figure 3.14. *In vivo* hM4D-based manipulation of neural activity does not influence the amplitudes of spontaneous miniature EPSCs in MSNs.

a. Sagittal brain section showing a dense infection of AAV DIO-hM4D-mCherry in the striatum of a D1-Cre; D2-GFP mouse. *Left and center*, DAPI and D2-GFP fluorescence allow for easy visualization of boundaries between the cortex, striatum and other major brain structures. *Right*. hM4d-mCherry expression is confined to the striatum. Despite Cre expression in cortex, 14 days after injection into the striatum of P2 mouse pup, little or no mCherry signal is observed in cortex. Scale bar: 500 μ m.

b. High-dose bilateral (extensive) or low-dose unilateral (sparse) injections of DIO-hM4D-mCherry AAV were delivered at P0-1. Recordings of spontaneous mEPSCs were carried out as described before. Amplitudes of mEPSCs of hM4D⁺ direct or indirect MSNs did not differ between saline and cno-injected siblings with extensive striatal hM4D expression (n=18 and 25; 7 and 8).

c. Amplitudes of mEPSCs of hM4D⁺ MSNs in mice sparsely infected with DIO-hM4D-mCherry AAV did not differ between mCherry⁺ and mCherry⁻ MSNs of either pathway (n=7-9 cells/group).

Figure 3.14 (Continued)

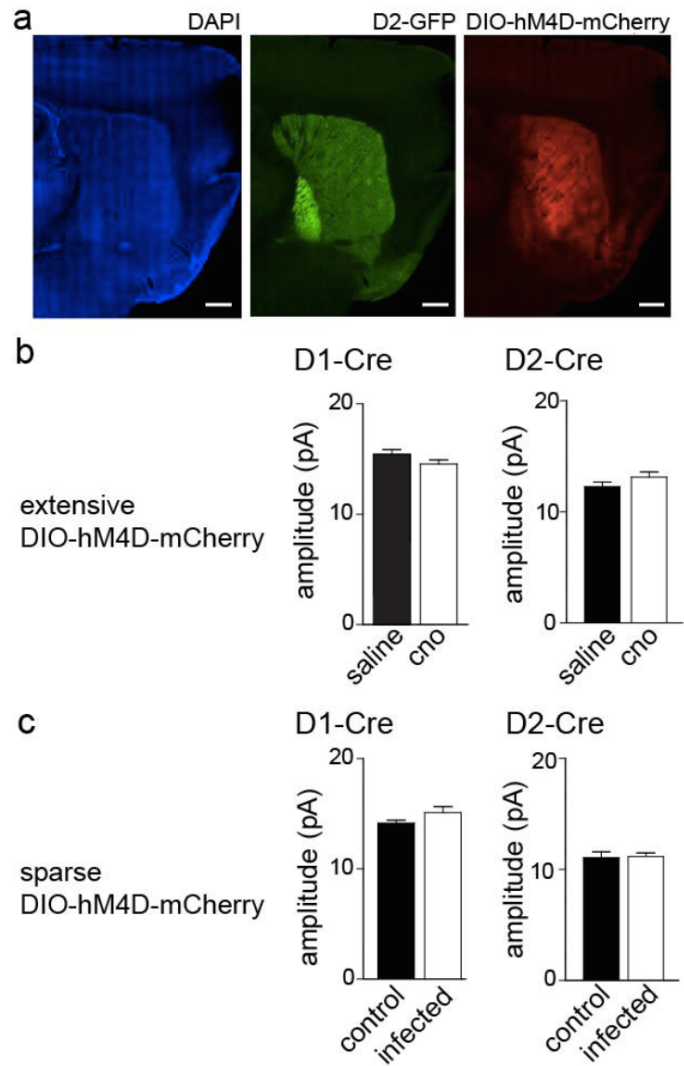
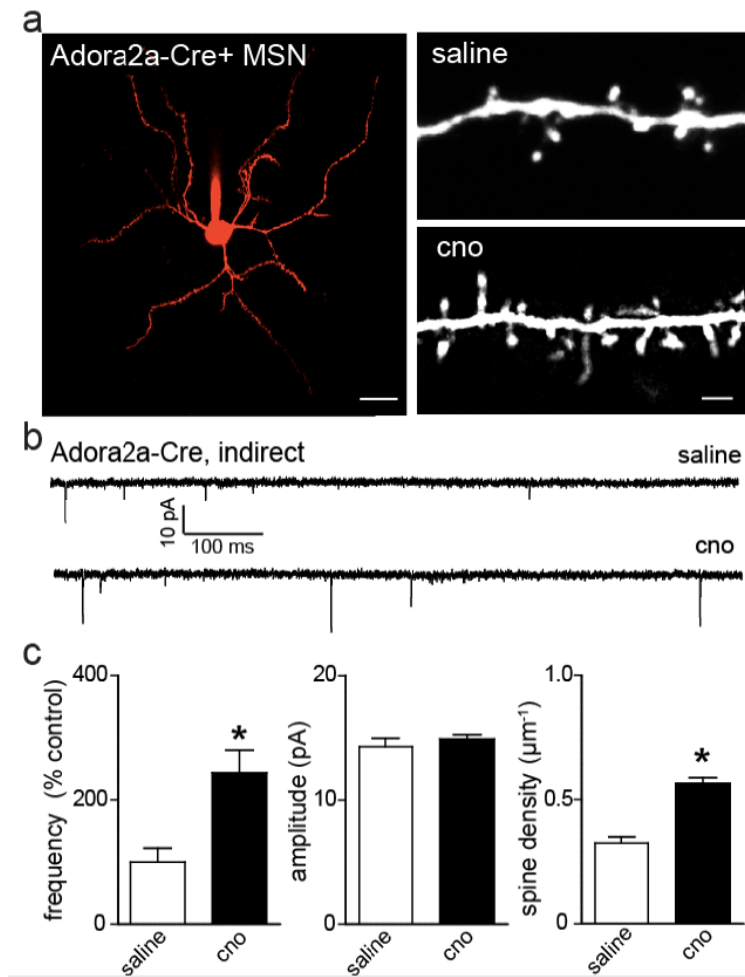


Figure 3.15. *In vivo* inhibition of indirect pathway MSNs using the Adora2a-Cre BAC recapitulates the increase in excitatory synaptogenesis observed using the D2-Cre BAC.

- a.** Mice carrying the Adora2a-Cre transgene were injected with AAV DIO hM4D-mCherry between P1-3 to achieve dense infection of indirect pathway MSNs. After administering cno or saline between P8-P15, acute slices were taken from sibling pairs on P14 or P15. *left*, indirect pathway MSNs expressing hM4D-mCherry were targeted for recording and imaging. Scale bar: 20 μm . *right*, 2PLSM of dendrites of MSNs from sibling animals treated with either cno or saline. Scale bar: 2 μm .
- b.** Representative voltage clamp traces of mEPSC recordings from MSNs of sibling animals treated with either cno or saline.
- c.** Summary data demonstrating that hM4D-mediated inhibition of indirect pathway MSNs using the Adora2a-Cre transgene, as with the D2-Cre transgene, increases indirect MSN mEPSC frequency (*left*) and spine density (*right*), without a change in mEPSC amplitude (*center*) (n=20 and 18; n=8/group) * indicates $p < 0.05$ for the comparison of hM4D-mCherry⁺ MSNs from saline and cno-injected mice.

Figure 3.15 (Continued)



perturbation of G-protein-coupled intracellular signalling pathways is not responsible for the changes in excitatory synapses.

Three lines of evidence—analyses of non-manipulated MSNs in pathway-specific conditional *Slc32a1* knockouts, of sparse *Slc32a1* null MSNs, and of the effects of widespread versus sparse hM4d manipulation of neural activity—support the hypothesis that circuit-level patterns of activity, rather than cell-intrinsic mechanisms, determine the degree of glutamatergic innervation of striatal MSNs. Inherent to this proposed mechanism is the assumption that the basal ganglia output modulates cortico-striatal or thalamo-striatal glutamatergic activity, which, in turn, regulates excitatory synaptogenesis in the striatum. To probe this mechanism, we directly tested the ability of glutamate exposure to drive spinogenesis in the striatum, and the effect of manipulating cortico-striatal activity on striatal spinogenesis and synaptogenesis.

To test whether glutamate release in the striatum is sufficient to induce spinogenesis, we focally stimulated non-spiny segments of P8–11 MSN dendrites with two-photon laser uncaging of glutamate²⁷. Sparse viral delivery of Cre was used to activate tdTomato reporter fluorescence in a small subset of MSNs in *D2-GFP;Ai14-*Isl*-tdTomato* mice. Two-photon laser-scanning microscopy was used to monitor dendritic structure during glutamate stimulation (Figure 3.16a,b). Stimulation power was calibrated to evoke moderate ~7 pA currents from existing spines (Figure 3.17). Using protocols that robustly induce synaptogenesis in layer 2/3 pyramidal neurons of developing cortex²⁷, we observed growth of a new dendritic spine at the glutamate

Figure 3.16. Cortico-striatal activity drives synaptogenesis in MSNs.

- a.** Focal release of glutamate is sufficient to trigger *de novo* spinogenesis in MSNs. 2PLSM image of a tdTomato (red) and GFP (green) expressing MSNs in a *D2-GFP*; *tdTomato*^{ff} mouse sparsely injected with Cre-mCherry encoding AAV at P0. Imaging was performed in an acute slice of striatum at P10. Scale bar: 20 μm . *right*, higher magnification image of a dendrite before (*top*) and after (*bottom*) triggering new spine growth. Scale bar: 2 μm . The stimulation protocol consisted of 40 uncaging pulses directed at the indicated spot (arrow) with 15 mW of 720 nm light measured at the objective back aperture.
- b.** Summary graph demonstrating ~50% success rate in generating new spines with glutamate uncaging in direct and indirect pathway MSNs at P8-11.
- c.** *left*, Cre expression driven by an *Rbp4* BAC (*Rbp4*-Cre) targets Cre to cortico-striatal projection neurons. Red fluorescence from a TdTomato reporter allele is present in deep layer cortical neurons and densely labels axons throughout striatum. Scale bar: 500 μm . *middle*, AAV DIO hM4D-mCherry injected into the cortex of a mouse carrying *Rbp4*-Cre and *D2-GFP* transgenes shows strong red fluorescence in deep layer somata in cortex and green fluorescence in striatum. Scale bar: 500 μm . *right*, Red channel, higher magnification view of boxed area in the center panel shows extensive hM4D-mCherry labeling of cortico-striatal axons.
- d and e.** *In vivo* inhibition of *Rbp4*-Cre neurons expressing hM4D during the window of excitatory synaptogenesis leads to a decrease in excitatory synapse number for both direct and indirect pathway MSNs. **d.** 2PLSM images of a dendrite from a direct

Figure 3.16 (Continued)

pathway MSN in a saline-injected mouse and a less spiny dendrite from a cno-injected littermate. Scale bar: 2 μm .

e. Summary data showing a decrease in direct and indirect pathway MSN mEPSC frequency (*left*) and spine density (*right*) for cno-treated mice versus saline treated littermates.

f – h. hM4D/cno-dependent decreases in MSN excitatory synapse number persist into early adulthood.

f. Timeline for experiments.

g. 2PLSM images of dendrites from indirect pathway MSNs from sibling mice in their early adulthood (P25- 28) after treatment with cno or saline during the time window for excitatory synaptogenesis (P8-15).

h. Summary data showing that decreases in mEPSC frequency (*left*) and spine density (*right*) persist into early adulthood.

Figure 3.16 (Continued)

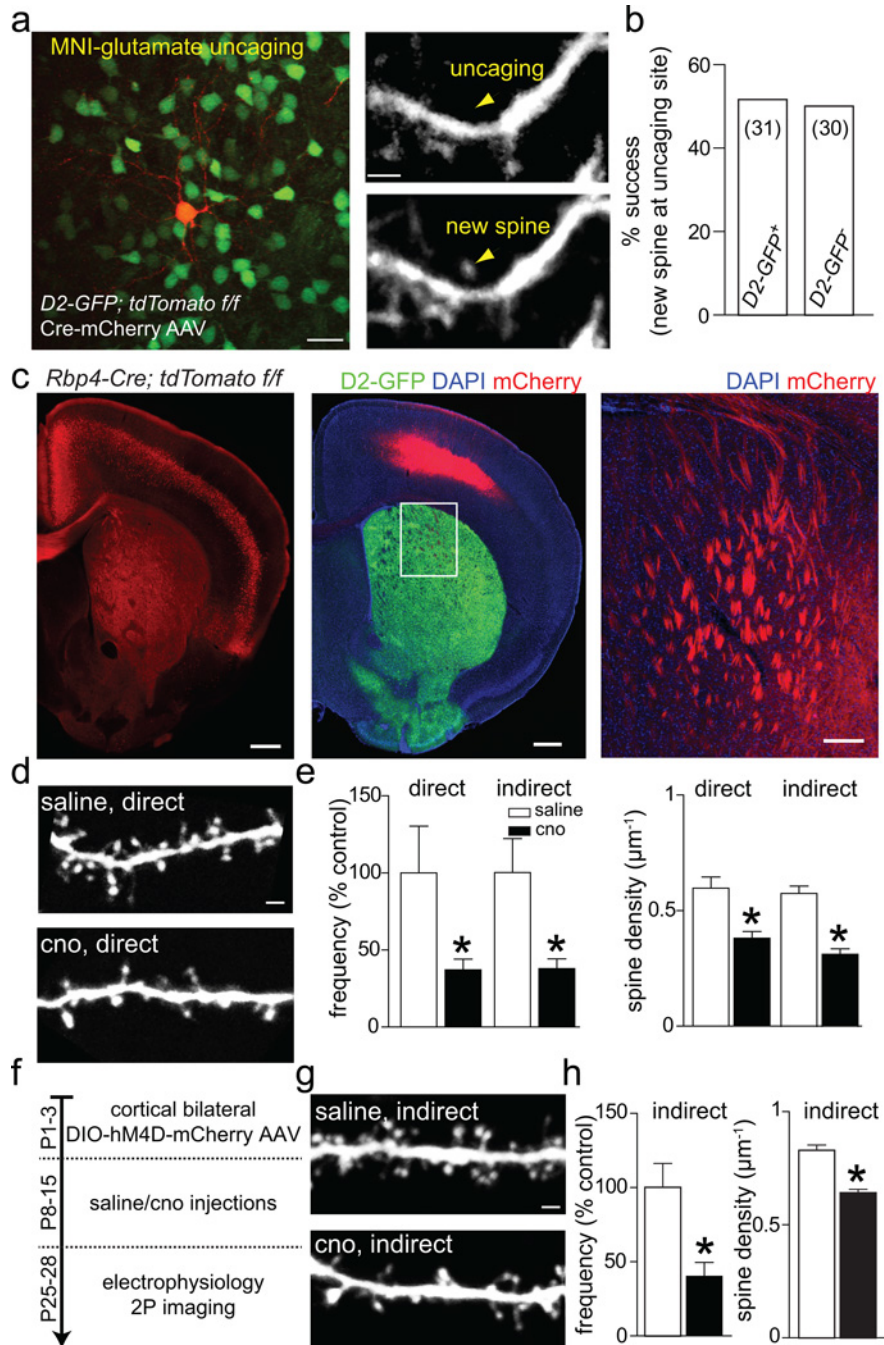


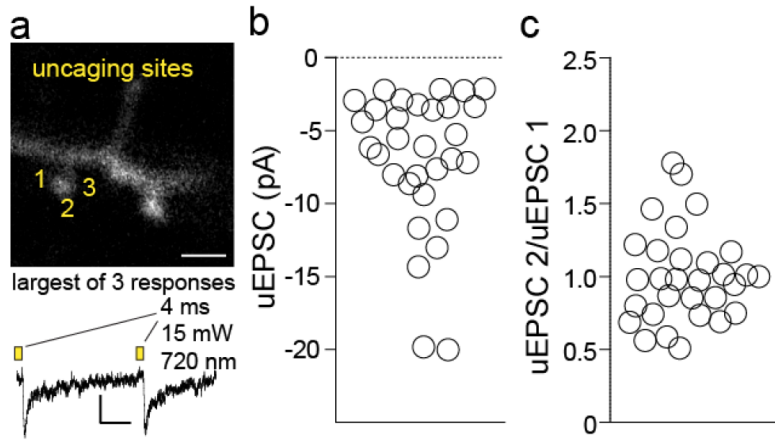
Figure 3.17. Calibration of the laser power used to trigger glutamate uncaging induced spinogenesis in young MSNs.

a. To calibrate the laser power used for glutamate uncaging, neurons of P8-P11 mice were voltage clamped and filled with Alexa Fluor-594 through the recording pipette. *top*, 2PLSM image of aspiny dendrite. Uncaging laser pulses were directed to 3 sites around a spine (1-3) and the locus of maximal uncaging-evoked excitatory post-synaptic current (uEPSC) amplitude was chosen for uncaging. *bottom*, Example of a pair of uEPSCs evoked at an existing spine. Scale bars: image, 2 μm for the image; uEPSC, 4 pA and 100 ms.

b. Amplitudes of uEPSCs elicited from spines of MSNs in slices from P8-11 mice in response to 15 mW of 720 nm laser light. The uEPSC amplitude ranged from 2.2 to 20 pA with a mean of 7 pA (n=31), similar to the size of mEPSCs in these cells³⁸.

c. No changes in current amplitudes were seen with 2 Hz stimulation, expressed as the ratio of the second to the first response (n=30).

Figure 3.17 (Continued)



uncaging site in ~50% of trials. The probability of spine growth was similar in direct and indirect pathway MSNs (Figure 3.16b), was unaffected by blockade of GABA_A receptors (52% and 50% success percentage for GFP⁺ and GFP⁻ MSNs in control conditions, and 56% and 51%, respectively, in GABA_A antagonist), and matched previous results in cortical pyramidal cells²⁷. Thus, glutamatergic stimulation is sufficient to drive spinogenesis in the developing striatum.

To test whether the postnatal activity of cortico-striatal projections drives synaptogenesis, we used the *Rbp4-cre* mouse line to express hM4D in cortico-striatal neurons emanating from deep cortical layers (Figure 3.16c). *Rbp4-cre;D2-GFP* mice were injected with the double floxed inverted AAV carrying hM4D–mCherry at P0–1 and, starting at P8, cno (1 mg kg⁻¹) or saline was administered subcutaneously twice per day to littermate pups. For MSNs of both pathways assayed at P14–15, mEPSC frequency and spine density were decreased after cno treatment (Figure 3.16d), with no change in mEPSC amplitude (direct pathway MSNs: frequency, 0.66 ± 0.2 Hz (saline) versus 0.25 ± 0.05 Hz (cno), *n* = 12 and 9; spine density, 0.60 ± 0.05 spines per μm (saline) versus 0.38 ± 0.03 spines per μm (cno), *n* = 7 and 6; indirect pathway MSNs: frequency, 0.65 ± 0.14 Hz (saline) versus 0.25 ± 0.04 Hz (cno), *n* = 16 and 16; spine density, 0.58 ± 0.03 spines per μm (saline) versus 0.31 ± 0.02 spines per μm (cno), *n* = 7 and 6) (Figure 3.16d,e). Because inhibition of *Rbp4-Cre*⁺ cortico-striatal projections caused no change in locomotion at P14–15 (Figure 3.18), activity-dependent control of striatal synaptogenesis is not secondary to behavioural changes.

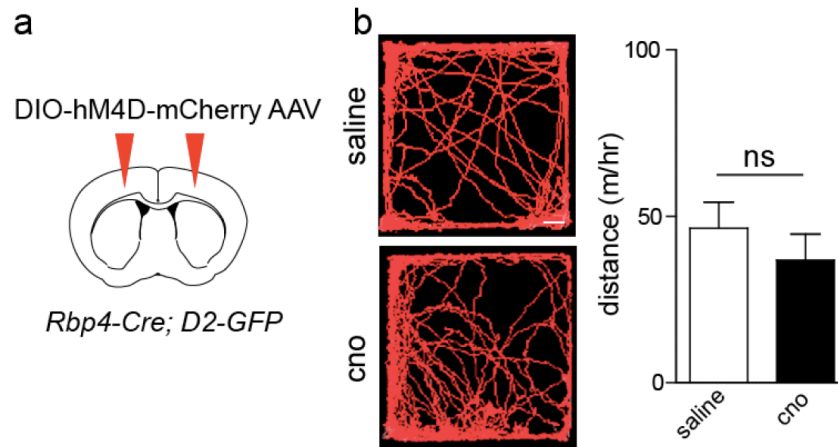
Figure 3.18. *In vivo* hM4D-based manipulation of neural activity in cortico-striatal projection neurons does not influence locomotion.

a. hM4D-mCherry was introduced into cortico-striatal projecting pyramidal neurons through bilateral cortical infection of AAV DIO-hM4D-mCherry into *Rbp4-Cre; D2-GFP* mice (P1-3). Littermate pairs were injected with saline or cno 2x/day (P8-15) and tested on P15.

b. View from the top of the arena used to test locomotor activity with examples of tracks for individual mice injected with saline or cno. Scale bar, 3 cm.

c. Average distance traveled in 1 hr does not differ for saline or cno-treated mice.

Figure 3.18 (Continued)



To determine whether activity-dependent changes in striatal synaptogenesis persist into early adulthood, we inhibited the activity of cortico-striatally projecting Rbp4-Cre neurons during P8–P15 and examined excitatory innervation in indirect pathway MSNs at P25–28 ([Figure 3.16f](#)). Both mEPSC frequency and spine density were reduced in cno-treated mice compared to saline-injected controls (indirect pathway MSNs: frequency, 0.73 ± 0.12 Hz (saline) versus 0.29 ± 0.07 Hz (cno), $n = 28$ and 26 ; spine density, 0.83 ± 0.02 spines per μm (saline) versus 0.64 ± 0.02 spines per μm (cno), $n = 10$ per group) ([Figure 3.16g,h](#)). Thus, perturbations of cortex-basal ganglia–thalamus circuit activity in early life can have lasting effects into adulthood.

Our data reveal that the balance of activity in direct/indirect pathways dictates postnatal excitatory innervation of the striatum. Because manipulating striatal output alters the structure of its input, activity must act recurrently, through a polysynaptic, multi-stage circuit. The simplest explanation for these findings is that glutamate release from cortical and thalamic axons in the striatum promotes the formation or stabilization of glutamatergic synapses onto MSNs. Perturbations that result in relative activation of the direct pathway compared to the indirect (and hence activate cortex and thalamus) will drive glutamatergic synapse formation in the striatum. Collateral connections among MSNs¹⁹ influence basal ganglia activity and may contribute to these effects. Such activity-dependent processes may be essential for refining locomotion and reward-based behaviour.

These mechanisms are fundamentally distinct from those believed to underlie topographic organization of sensory cortices during postnatal development. In these

cortical areas, waves of neural activity pass information about sensory maps from one stage of processing to the next^{28,29}, and these mappings are translated into synaptic connectivity through spike-timing-dependent plasticity rules³⁰. In contrast, striatal inputs from widespread cortical areas show only modest topographic organization. Instead of sensory maps, synaptic networks throughout the cortex-basal ganglia–thalamus loop are thought to reflect parallel, segregated loops of mixed inhibitory and excitatory projections. Here we show that activity propagates through cortex-basal ganglia–thalamus circuits to specify synaptic networks based on the balanced output of direct and indirect pathways in a manner that can, through positive feedback, select for recurrent closed loops.

References

1. Wiesel, T. N. & Hubel, D. H. Single-cell responses in striate cortex of kittens deprived of vision in one eye. *J. Neurophysiol.* **26**, 1003–1017 (1963).
2. Smith, G. B., Heynen, A. J. & Bear, M. F. Bidirectional synaptic mechanisms of ocular dominance plasticity in visual cortex. *Phil. Trans. R. Soc. B* **364**, 357–367 (2009).
3. Stephenson-Jones, M., Samuelsson, E., Ericsson, J., Robertson, B. & Grillner, S. Evolutionary conservation of the basal ganglia as a common vertebrate mechanism for action selection. *Curr. Biol.* **21**, 1081–1091 (2011).
4. Yin, H. H. & Knowlton, B. J. The role of the basal ganglia in habit formation. *Nat. Rev. Neurosci.* **7**, 464–476 (2006).
5. Alexander, G. E., DeLong, M. R. & Strick, P. L. Parallel organization of functionally segregated circuits linking basal ganglia and cortex. *Annu. Rev. Neurosci.* **9**, 357–381 (1986).

6. Nambu, A. Somatotopic organization of the primate basal ganglia. *Front. Neuroanat.* **5**, 26 (2011).
7. Smith, Y., Bevan, M. D., Shink, E. & Bolam, J. P. Microcircuitry of the direct and indirect pathways of the basal ganglia. *Neuroscience* **86**, 353–387 (1998).
8. Gerfen, C. R. The neostriatal mosaic: multiple levels of compartmental organization in the basal ganglia. *Annu. Rev. Neurosci.* **15**, 285–320 (1992).
9. Albin, R. L., Young, A. B. & Penney, J. B. The functional anatomy of basal ganglia disorders. *Trends Neurosci.* **12**, 366–375 (1989).
10. Kelly, R. M. & Strick, P. L. Macro-architecture of basal ganglia loops with the cerebral cortex: use of rabies virus to reveal multisynaptic circuits. *Prog. Brain Res.* **143**, 447–459 (2004).
11. Alexander, G. E. & Crutcher, M. D. Functional architecture of basal ganglia circuits: neural substrates of parallel processing. *Trends Neurosci.* **13**, 266–271 (1990).
12. Kravitz, A. V. et al. Regulation of parkinsonian motor behaviours by optogenetic control of basal ganglia circuitry. *Nature* **466**, 622–626 (2010).
13. Ferguson, S. M. et al. Transient neuronal inhibition reveals opposing roles of indirect and direct pathways in sensitization. *Nature Neurosci.* **14**, 22–24 (2011).
14. Cho, J. & West, M. O. Distributions of single neurons related to body parts in the lateral striatum of the rat. *Brain Res.* **756**, 241–246 (1997).
15. Tong, Q., Ye, C.-P., Jones, J. E., Elmquist, J. K. & Lowell, B. B. Synaptic release of GABA by AgRP neurons is required for normal regulation of energy balance. *Nature Neurosci.* **11**, 998–1000 (2008).
16. McIntire, S. L., Reimer, R. J., Schuske, K., Edwards, R. H. & Jorgensen, E. M. Identification and characterization of the vesicular GABA transporter. *Nature* **389**, 870–876 (1997).
17. Wojcik, S. M. et al. A shared vesicular carrier allows synaptic corelease of GABA and glycine. *Neuron* **50**, 575–587 (2006).
18. Gong, S. et al. A gene expression atlas of the central nervous system based on bacterial artificial chromosomes. *Nature* **425**, 917–925 (2003).

19. Taverna, S., Ilijic, E. & Surmeier, D. J. Recurrent collateral connections of striatal medium spiny neurons are disrupted in models of Parkinson's disease. *J. Neurosci.* **28**, 5504–5512 (2008).
20. Sohal, V. S., Zhang, F., Yizhar, O. & Deisseroth, K. Parvalbumin neurons and gamma rhythms enhance cortical circuit performance. *Nature* **459**, 698–702 (2009).
21. Nimchinsky, E. A., Sabatini, B. L. & Svoboda, K. Structure and function of dendritic spines. *Annu. Rev. Physiol.* **64**, 313–353 (2002).
22. Somogyi, P., Bolam, J. P. & Smith, A. D. Monosynaptic cortical input and local axon collaterals of identified striatonigral neurons. A light and electron microscopic study using the Golgi-peroxidase transport-degeneration procedure. *J. Comp. Neurol.* **195**, 567–584 (1981).
23. Tepper, J. M., Sharpe, N. A., Koós, T. Z. & Trent, F. Postnatal development of the rat neostriatum: electrophysiological, light- and electron-microscopic studies. *Dev. Neurosci.* **20**, 125–145 (1998).
24. Saunders, A., Johnson, C. A. & Sabatini, B. L. Novel recombinant adeno-associated viruses for Cre activated and inactivated transgene expression in neurons. *Front Neural Circuits* **6**, 47 (2012).
25. Rogan, S. C. & Roth, B. L. Remote control of neuronal signaling. *Pharmacol. Rev.* **63**, 291–315 (2011).
26. Krashes, M. J. et al. Rapid, reversible activation of AgRP neurons drives feeding behavior in mice. *J. Clin. Invest.* **121**, 1424–1428 (2011).
27. Kwon, H.-B. & Sabatini, B. L. Glutamate induces de novo growth of functional spines in developing cortex. *Nature* **474**, 100–104 (2011).
28. Meister, M., Wong, R. O., Baylor, D. A. & Shatz, C. J. Synchronous bursts of action potentials in ganglion cells of the developing mammalian retina. *Science* **252**, 939–943 (1991).
29. Triplett, J. W. et al. Retinal input instructs alignment of visual topographic maps. *Cell* **139**, 175–185 (2009).
30. Bi, G. & Poo, M. Synaptic modification by correlated activity: Hebb's postulate revisited. *Annu. Rev. Neurosci.* **24**, 139–166 (2001).

Methods

Mouse strains and genotyping

Animals were handled according to protocols approved by the Harvard Standing Committee on Animal Care, in accordance with NIH guidelines. To generate mice with conditional knockout of *Slc32a1* from the direct and indirect pathway, *D1/D2-cre;Slc32a1^{f/+}* mice were crossed with *Slc32a1^{ff}* mice. Conditional knockout crosses were made using either male or female parents as Cre carriers. To generate pups carrying the D1-, D2-, Adora2a- or Rbp4-Cre transgenes, D1-, D2-, Adora2a- or Rbp4-Cre parents, either male or female, were crossed to wild-type C57BL/6 mice. D2-BAC and GAD67 knock-in GFP transgenes were also introduced through either parent or both parents. A full description of the transgenic mouse lines used in this study is provided in Table 3.1. Genotyping was performed from tail tissue sampled at P0.5–5. Tail tissue was digested overnight (Viagen) and PCR was performed using the lysates as template DNA. The genotyping primers are listed in Table 3.2 and the PCR protocols are provided below.

PCR protocol 1: (1) 95 °C for 5 min; (2) 95 °C for 30 s; (3) 53 °C for 30 s; (4) 72 °C for 1 min; (5) repeat (2)–(4) for 35 cycles; (6) 72 °C for 5 min.

PCR protocol 2: (1) 94 °C for 3 min; (2) 94 °C for 45 s; (3) 66 °C, down –1 °C each cycle for 45 s; (4) 72 °C for 45 s; (5) repeat (2)–(4) for 9 cycles; (6) 94 °C for 30 s; (7) 58 °C for 30 s; (8) 72 °C for 30 s; (9) repeat (6)–(8) for 20 cycles; (10) 72 °C for 10 min.

Table 3.1. Transgenic mouse lines

Reference Name	Line	Transgene	Cell Type Expression	Citation
Cell Type Driver Lines				
D1-Cre (BAC)	dopamine receptor D1A (EY262)	Cre	Direct Pathway MSNs	GENSAT Gong et al. 2003
D2-Cre (BAC)	dopamine receptor D2 (ER43)	Cre	Indirect Pathway MSNs	GENSAT Gong et al. 2003
D2-GFP (BAC)	dopamine receptor D2 (S118)	EGFP	Indirect Pathway MSNs	GENSAT Gong et al. 2003
GAD67-GFP (Knock-In)	GAD67-GFP	GFP	GAD67 expressing (GABAergic) cells	Tamamaki et al. 2003
Rbp4-Cre (BAC)		Cre	Cortical-striatal deep layers	genebrainsystems.nimh.nih.gov
Adora2a-Cre (BAC)	adenosine A2a receptor	Cre	Indirect Pathway MSNs	GENSAT Gong et al. 2007
Floxed Alleles				
Vesicular GABA transporter (<i>Slc32a1</i>)	<i>Slc32a1</i> ^{loxP/loxP} (exon 2 floxed)			Tong et al. 2008
Cre Reporter Lines				
TdTomato	B6.Cg-Gt(ROSA)26Sortm14(CAG-tTomato)Hze	TdTomato		Madisen et al. 2011

Table 3.2. Genotyping primers

Gene	Forward Primer	Reverse Primer	Band Size (bps)	PCR Protocol
D1 Cre	CATTTGGAGAGATGTGGCACC	GCGAACCTCATCACTCGTTGC	492	1
D2 Cre	AGCATGCCTTGAAAACACTCCTG	GCGAACCTCATCACTCGTTGC	144	1
Cre	GCGGTCTGGCAGTAAAACTATC	GTGAAACAGCATTGCTGCACTT	100	1
GFP	GACGTAAACGGCCACAAGTTCAG	ATGGTGCGCTCCTGGACGTAG	210	2
<i>Slc32a1</i>	TCCTTTGTGGCTTCCTCCG	GGATAGAAGAAGTGTGGACC	Floxed = 250, wild type = 190	1

Table 3.3. Adeno-associated viruses

Reference Name	Vector Name	Serotype	Titer (virus molecules / ml)	Citation
DIO_ChR2-mCherry	AAV-double_floxed-hChR2(H134R)-mCherry-WPRE-pA	8	8 x 10 ¹²	Atasoy et al. 2008
DO_ChR2-mCherry	AAV-DO-hChR2(H134R)-mCherry-WPRE-pA	8	3x 10 ¹²	Saunders et al. 2012 (Chapter 2)
DIO_hM4D-mCherry	AAV-DIO-hM4D-WPRE-pA	8	1.6 x 10 ¹³ or 2 x 10 ¹²	Krashes et al. 2011
Cre-mCherry	AAV-AM/CBA-mCherry-Cre-WPRE-BGH	1	1.2 x 10 ¹³	Lu et al. 2009

Stereotaxic injections

For intracranial injections, P0–7-day-old mice were anaesthetized with isoflurane and placed into a stereotaxic apparatus. Virus was delivered at a maximum rate of 100 nl min⁻¹ using a Microinject system (WPI). Dorsolateral striatum was targeted by directing the needle approximately 1 mm anterior to midpoint between ear and eye, 1.5 mm from midline and 1.8 mm ventral to brain surface, and these coordinates were adjusted based on age. Cortical injections were similarly targeted in the anterior–posterior and medial–lateral axes, but the needle was directed 0.8 mm ventral to brain surface. Unilateral injections of 350–500 nl were used to drive Chr2 expression for electrophysiology experiments, pathway tracing, cell targeting for mEPSC recordings and cell fills for dendritic spine density analyses; 500–750 nl bilateral or 50 nl unilateral injections were used in circuit manipulation with hM4D; 50 nl unilateral injections were used for sparse postnatal *Slc32a1* knockout; 50 nl unilateral injections (1:10 dilution) were used for inducing tdTomato expression in *de novo* spinogenesis experiments. Virus titres are provided in Table 3.3 and injection rates were 50–100 nl min⁻¹. After injections and wound closure, mice received flunixin for analgesia and were returned to home cages for 8+ days.

Slice preparation

Coronal striatal slices were prepared as described previously for rat³⁴. Mice were anaesthetized by inhalation of isoflurane. Cerebral hemispheres were removed and

placed into cold choline-based artificial cerebrospinal fluid (choline-ACSF) containing 25 mM NaHCO₃, 1.25 mM NaH₂PO₄, 2.5 mM KCl, 7 mM MgCl₂, 25 mM glucose, 1 mM CaCl₂, 110 mM choline chloride, 11.60 mM ascorbic acid and 3.10 mM pyruvic acid, and equilibrated with 95% O₂/5% CO₂. Tissue was blocked and transferred into a slicing chamber containing choline-ACSF. Coronal striatal slices (300 μm) were then cut on a Leica VT1000 s (Leica Instruments) and transferred into a holding chamber with ACSF containing (in mM) 127 NaCl, 2.5 KCl, 25 NaHCO₃, 1.25 NaH₂PO₄, 2.0 CaCl₂, 1.0 MgCl₂ and 25 glucose, equilibrated with 95% O₂/5% CO₂. Slices were incubated at 34 °C for 30–45 min before recording.

Electrophysiology

Whole-cell recordings were obtained from striatal MSNs visualized under infrared differential interference contrast (IR-DIC) using patch pipettes with pipette resistance of 2.5–4.5 MW. To identify infected MSNs or those belonging to the indirect pathway, mCherry or GFP fluorescence was detected using epifluorescence illumination. For ChR2-evoked current recordings, a high Cl⁻ internal solution containing 100 mM CsCl, 35 mM CsF, 10 mM HEPES, 4 mM MgCl₂, 4 mM Na₂ATP, 0.4 mM NaGTP, 10 mM Na₂CrePO₄, 1 mM EGTA (pH 7.4) was used. For miniature excitatory postsynaptic current recordings, the internal solution consisted of 120 mM CsMeSO₄, 15 mM CsCl, 8 mM NaCl, 10 mM TEACl, 10 mM HEPES, 2 mM QX314, 4 mM MgATP, 0.3 mM NaGTP (pH 7.4). Alexa Fluor 594 (10–20 mM) was added to internals to visualize cell morphology and to confirm cell identity as MSN. For cell-attached recordings, a caesium-based internal without Alexa Fluor 594 was used instead and traces were

monitored for signs of breaking in. Recordings were made using an Axoclamp 700B amplifier (Axon Instruments) at room temperature for MSN collateral current analysis and mEPSC recordings, and at elevated temperature (34 °C) for cell-attached recordings. Data were filtered at 3 kHz and sampled at 10 kHz. Series resistance, measured with a 5 mV hyperpolarizing pulse in voltage clamp, was on average under 20 MW and less than 25 MW, uncompensated. All voltage-clamp recordings were made from cells held at -70 mV, except for a small minority of cells in which ChR2 stimulation drove unclamped spikes. In this case, cells were held at -40 mV and peak currents were multiplied by 1.75, the magnitude increase predicted by -30 mV change in driving force of Cl and confirmed by experiments where ChR2 currents were elicited at both holding potentials (-70 and -40 mV). For miniature EPSC recordings, all MSNs were held at -70 mV. Extracellular recordings were acquired in voltage-clamp mode without imposing a holding potential.

Optogenetic activation

To activate ChR2 in acute slices, 473-nm laser light (Optoengine) was focused onto the back aperture of the ×60 water immersion objective to produce whole-field illumination. To quantify the laser light delivered with each pulse, light leak through a high-pass dichroic filter was measured using a photodiode calibrated by measuring the power at the focal plane of ×60 objective. For each ChR2 activation experiment in [Figure 3.2](#), six different light intensities were used to drive postsynaptic currents (0.1–20 mW). Summary data presented in [Figure 3.2](#) are based on the strongest, 20 mW stimulation. For optogenetic activation of neurons during extracellular recording, light power was

slowly increased while acquiring data until a moderate firing rate (~4–20 Hz) was achieved.

Pharmacology

Pharmacological agents were used at the following final concentrations. For ChR2-evoked current recordings, ACSF contained 10 mM CPP (Tocris Cookson), 10 mM NBQX (Tocris), 10 mM scopolamine hydrobromide (Tocris). For mEPSC recordings, ACSF contained 1 mM TTX (Sigma), 50 mM SR 95531/gabazine (Tocris), 10 mM CPP and 10 mM scopolamine hydrobromide. For extracellular recordings, ACSF contained CPP, NBQX, SR 95531 and scopolamine hydrobromide. SR 95531 was present in a subset of glutamate-uncaging-evoked spinogenesis experiments. All reagents were dissolved in distilled water and diluted to their final concentrations in ACSF on the day of the experiment, except for NBQX, which was dissolved in DMSO. Clozapine-*n*-oxide (Sigma) was used at 10 mM for slice experiments. For *in vivo* circuit activity manipulation, clozapine-*n*-oxide in sterile saline was administered subcutaneously at 1 mg kg⁻¹ body weight twice daily.

Two-photon imaging

Two-photon laser-scanning microscopy was performed using a custom microscope as previously described³⁴. Cell morphology was visualized using Alexa Fluor 594 (10–20 mM) excited with 810–840-nm light and introduced into the cell through whole-cell recording or single-cell electroporation. Briefly, a pipette containing Alexa Fluor 594 in dH₂O was guided to a MSN cell body with low positive pressure. Pressure was released

and a single 0.2-ms-long 0.1–0.3 V pulse was delivered through an electrical stimulator (A.M.P.I) to fill the soma with dye, which rapidly diffused into dendrites and spines (~5 min). A two-photon laser-scanning microscopy three-dimensional image stack through each neuron was collected, followed by stacks through 2–3° dendritic segments at a tenfold higher magnification. For dendritic spine density and spine shape analyses, cells were coded and analysed used custom-written routines in MATLAB. Three-to-five secondary and tertiary dendrites per MSN were analysed. The size of each spine was measured in the optical section of maximal brightness.

Glutamate uncaging

Uncaging of MNI-glutamate was done on a custom-built microscope combining two-photon laser-scanning microscopy and two-photon laser photoactivation, or uncaging. Two mode-locked Ti:sapphire lasers (Coherent) tuned to 920 nm and 720 nm were used for imaging tdTomato fluorescence and uncaging MNI-glutamate, respectively. The intensity of each laser was independently controlled by Pockels cells (Conoptics). For uncaging, 2.5 mM MNI-glutamate (Sigma-Aldrich) was added to Mg-free ACSF and 15 mW of 720 nm light at the specimen was used to focally release the uncaging group. To visualize the dendrites of MSNs of known pathways, mice carrying at least one tdTomato reporter allele and a D2-GFP BAC transgene were injected with AAV carrying Cre-mCherry at P0–1. AAV injections were titred to generate sparse Cre expression in striatum. tdTomato⁺ MSN dendrites were selected using the following two criteria: smooth dendritic membrane in the immediate location of uncaging spot and the presence of at least one dendritic spine nearby (within ~5 mm). MNI-glutamate was

uncaged near the dendrite (~0.5 mm away from the edge) at 2 Hz using 40 4-ms-long pulses as described previously²⁷. This protocol drives a ~7-pA uncaging-evoked EPSC in whole-cell voltage-clamp recording (Figure 3.17). Dendrite images were taken before and immediately after induction protocol.

Behavioural analysis

For measuring activity levels, 14–17-day-old mice were monitored one at a time using the large (45 × 45 cm²) home cage module of EthoVision XT (Noldus) with centre point and nose point tracking. No food or water was provided for the 1 h duration of the recording. Comparisons were made between sibling littermates carrying 0 or 1 *Slc32a1* alleles on the same day, with genotype order counterbalanced. All recordings were done in a narrow time window in littermate mice maintained on a standard 12/12 h light/dark cycle. The distance travelled during 1 h was quantified.

AAV production

Adeno-associated virus (AAV) vector DNA was amplified in recombination-deficient bacteria (OneShot Stbl3, Invitrogen) and packaged by a commercial vector core facility (University of North Carolina). Table 2.1 describes the AAV vectors used in this study. The Cre-silenced ChR2–mCherry vector (DO–ChR2–mCherry) was generated by reversing the orientation of the ChR2–mCherry transgene with respect to the two pairs of flanking *loxP* sites using the Asc1 and Nhe1 restriction sites.

Fixed-tissue preparation, imaging and immunohistochemistry

Mice were transcardially perfused with 4% paraformaldehyde and the brains were post-fixed for 1–7 days. Brains were sectioned coronally or sagittally at 40 μm using a Vibratome. No immuno-enhancement was used to increase the signal of native fluorophores. For Cre immunofluorescence, 1:6 series of sections through the striatum were incubated overnight at 4 °C with mouse anti-Cre antibody in TBS with 0.5% Tween-20 (1:250, Invitrogen). The following day tissue was rinsed in TBS, reacted with goat anti-mouse Alexa Fluor 488 (1:500, Molecular Probes) for 1 h at room temperature, rinsed, mounted onto superfrost slides, dried and coverslipped under ProLong antifade reagent with DAPI (Molecular Probes). Images were acquired with a Zeiss LSM 510 META confocal microscope (Harvard NeuroDiscovery Center). Slides were coded for confocal microscopy and data analysis. For every animal, five fields of view were selected for analysis from several striatal sections, which matched the location of electrophysiological recordings. Two-dimensional 1-mm-thick optical sections were analysed in ImageJ using co-localization and cell counter plug-ins. The number of Cre⁺ and Cre⁻ DAPI-stained nuclei was quantified and expressed as a percentage. On average >600 cells were examined for Cre expression in every animal. The code was broken after completion of the analysis.

For parvalbumin immunofluorescence, sections were incubated in mouse anti-parvalbumin primary antibody (1:2,000, Millipore), goat anti-mouse Alexa 488 secondary antibody, and coverslipped under ProLong antifade reagent with DAPI. Image stacks were acquired with a with an Olympus FV1000 laser scanning confocal

microscope (Harvard Neurobiology Imaging Facility). The number of parvalbumin-labelled, D1-Cre tdTomato reporter-positive neurons was quantified. Stacks through >300 neurons from four mice were analysed.

Whole-brain imaging

Mice were unilaterally injected with DIO-ChR2-mCherry AAV into the right dorsal striatum and transcardially perfused with 4% paraformaldehyde 8–10 days later. Brains were sectioned sagittally at 100 μm . For every brain, the slice with maximal cross-section of SNr or globus pallidus was selected for imaging with an Olympus VS110 slide scanning microscope using $\times 20$ objective. No immuno-enhancement was needed to visualize long-range projections. For confocal imaging, sections were scanned on a confocal microscope under a $\times 63$ oil objective. ImageJ was used to analyse fluorophore distributions and data were expressed as area fractions.

Data analysis

Offline data analysis for electrophysiology was performed using custom software written in Igor Pro (Wavemetrics) and MATLAB. Statistical analyses were done using GraphPad PRIZM 5 software (GraphPad). All values are reported as means \pm s.e.m., unless noted otherwise. Statistical significance was determined by two-tailed Student's *t*-tests, with Welch's correction for data sets with significantly different variances, and two-tailed Wilcoxon signed rank test for non-parametrically distributed data. Two-way ANOVA with Bonferroni post-hoc comparisons and log-rank Mantel–Cox test were used

for weight and lifespan analyses in Figure 3.5 $P < 0.05$ was considered to be statistically significant.

References (Methods)

31. Tamamaki, N. *et al.* Green fluorescent protein expression and colocalization with calretinin, parvalbumin, and somatostatin in the GAD67-GFP knock-in mouse. *J Comp Neurol* **467**, 60–79 (2003).
32. Gong, S. *et al.* Targeting Cre recombinase to specific neuron populations with bacterial artificial chromosome constructs. *J Neurosci* **27**(37):9817-9823 (2007).
33. Madisen, L. *et al.* A robust and high-throughput Cre reporting and characterization system for the whole mouse brain. *Nat Neurosci* **13**(1):133-142 (2010).
34. Carter, A. G. & Sabatini, B. L. State-dependent calcium signaling in dendritic spines of striatal medium spiny neurons. *Neuron* **44**, 483–493 (2004).

Chapter 4

A direct GABAergic output of the basal ganglia

Arpiar Saunders, Ian A. Oldenburg, Vladimir K. Berezovskii, Caroline A. Johnson, Nathan D. Kingery, Hunter L. Elliott, Tiao Xie, Charles R. Gerfen and Bernardo L. Sabatini

This chapter is based on submitted work.

Author Contributions

A.S., I.A.O and B.L.S designed the experiments. A.S. performed the anatomical and acute slice experiments, analyzed the data and assisted all other parts of the study. I.A.O performed *in vivo* physiology experiments and analyzed data. C.A.J performed immunohistochemistry experiments and assisted with mouse genotyping. V.K.B. performed *rhesus macaque* anatomical experiments. C.R.G sliced and imaged mouse brains for three-dimensional reconstructions. N.D.K performed the sectioning, staining and imaging for array tomography. H.L.E and T.X. assisted in the image analysis for axon detection in whole-brain reconstructions and array tomography respectively. A.S. and B.L.S wrote the manuscript with contributions from the other authors.

Abstract

The basal ganglia (BG) are a phylogenetically conserved set of subcortical nuclei necessary for coordinated motor action and reward learning¹. Accepted models postulate that the BG modulate cerebral cortex indirectly via an inhibitory output to thalamus, bidirectionally controlled from within the BG by direct (dSPNs) and indirect (iSPNs) pathway striatal projection neurons²⁻⁴. The BG thalamic output sculpts cortical activity by interacting with signals from sensory and motor systems⁵. Here we describe a direct projection from the globus pallidus externus (GP), a central nucleus of the BG, to frontal regions of the cerebral cortex (FC). Two cell types make up the GP-FC projection, distinguished by their electrophysiological properties, cortical projection patterns and expression of choline acetyltransferase (ChAT), a genetic marker for neurons that release the neurotransmitter acetylcholine (ACh). Despite these differences, ChAT+ cells, which have historically been identified as an extension of the nucleus basalis (NB), as well as ChAT- cells, release the inhibitory neurotransmitter GABA (γ -aminobutyric acid) and are inhibited by iSPNs and dSPNs of dorsal striatum. Thus GP-FC cells comprise a direct GABAergic/cholinergic projection that places frontal cortex under the inhibitory control of the striatum. Furthermore, iSPN inhibition of GP-FC cells is sensitive to dopamine 2 receptor signaling, revealing a pathway by which drugs that target dopamine receptors for the treatment of neuropsychiatric disorders can act in the BG to modulate frontal cortices.

Introduction, Results & Discussion

iSPNs are the major dopamine 2 receptor (D2r) expressing cells in the brain and project from dorsal striatum exclusively to the GP. This connectivity suggests that the therapeutic effects of drugs that target D2rs to treat schizophrenia⁶, bipolar disorder⁷ and obsessive compulsive disorder⁸ likely involve GP circuits. In humans, the GP is one of the most transcriptionally distinctive regions of the brain⁹, yet how this molecular diversity maps onto functionally distinct cell types is unclear. The anatomy of projection axons, intrinsic firing properties, and synaptically released neurotransmitters often distinguish neuron types and determine the function of each type in controlling neuronal circuits and behavior. Previous studies generally describe that GP neurons are spontaneously active, project to all nuclei of the BG and thalamus¹⁰, and release the neurotransmitter GABA¹¹. Thus the GP is thought to coordinate subcortical activity through inhibition^{12,13}.

In contrast to this accepted function, anatomical studies across species have identified ChAT⁺ neurons in and around the GP that project to cortex¹⁴⁻¹⁶. These cells have been assumed to be an extension of the adjacent NB, associated with the limbic functions of the basal forebrain and not the motor, sensory and cognitive functions of the BG¹⁷. However, several lines of evidence suggest they may be part of the GP. Anatomically, ChAT⁺ GP cells appear to be innervated by SPNs from dorsal striatum¹⁸ despite the rarity of iSPN synapses at the ultrastructural level¹⁹. Functionally, recordings in macaques described GP neurons with NB-like firing properties that were responsive to reward²⁰, a computation attributed to the BG²¹. Behaviorally, humans with lesions of

the GP exhibit reduced metabolism in frontal cortices and psychiatric symptoms reminiscent of patients with fronto-temporal lobe damage, consistent with loss of substantial extrinsic input²². Therefore we asked whether the GP contains a projection system to FC that is integrated into the BG circuitry.

We performed retrograde labeling by injecting fluorescent microspheres (retro beads) into the FC of *Drd2*-EGFP mice to localize FC projection neurons with respect to the GP borders defined by the iSPN axonal arbor ([Figure 4.1a](#)). Retro bead⁺ cells were found within the GP and clustered on the GP/NB and GP/striatum borders ([Figure 4.1b](#)). Like other basal forebrain projection systems to cortex²³, these GP-FC cells arborize exclusively in ipsilateral cortex ([Figure 4.2a-c](#)).

To investigate if GP-FC cells use GABA or ACh as a neurotransmitter, we repeated retrograde labeling and ChAT immunostaining in *Vgat*^{i-Cre/+}; *Rosa26*^{lsl-zsGreen/+} or *GAD2*^{i-Cre/+}; *Rosa26*^{lsl-zsGreen/+} mice where cells expressing the vesicular GABA transporter (*Vgat*, encoded by *Slc32a1*) or glutamic acid decarboxylase 2 (*GAD2*) are fluorescently labeled ([Figure 4.1c](#)). Nearly all retro bead⁺ GP cells were *Vgat*⁺ (n=159 of 159 cells, n=3 mice) or *GAD2*⁺ (n=231 of 233 cells, n=2 mice), whereas 72% were ChAT⁺ (n=215 of 300 cells, n=5 mice) and 28% ChAT⁻ (n=85 of 300 cells). Based on ubiquitous *Vgat* / *GAD2* but differential ChAT expression, we conclude that the GP-FC projection consists of two molecularly distinct cell types²⁴ (hereafter ChAT⁺ and ChAT⁻ cells, [Figure 4.1d](#)) and that ChAT⁺ cells of the adjacent NB express GABAergic markers, consistent with previous transcriptional analysis²⁵.

Figure 4.1. The Globus Pallidus (GP) and bordering nucleus Basalis (NB) contain two GABAergic cell types that project to frontal cortex (FC).

a. *Left*, sagittal section from a *Drd2*-EGFP mouse injected with retro beads (red) into FC, which include dorsal and ventral agranular insular cortex, as well as anterior regions of primary motor, secondary motor and primary sensory cortex. EGFP (green) is expressed in iSPNs of the striatum (Str). iSPN axons arborize in the GP and define its anatomical boundaries. DAPI (blue), nuclear stain. *Right*, higher magnification view of the GP from a single, more medial section from the same mouse. Retro bead⁺ neurons (inset and highlighted with circles) are located in the GP and around the GP/NB border. ac, anterior commissure; VP, ventral pallidum.

b. Overlaid locations of retro bead⁺ cells in the central ~300 mm (medial-lateral axis) of GP from separate FC injections (n=3 mice).

c. FC retro bead labeling in *Vgat*^{Cre/+}; *Rosa26*^{Isl-zsGreen/+} or *GAD2*^{Cre/+}; *Rosa26*^{Isl-zsGreen/+} mice followed by ChAT immunostaining (magenta) demonstrates that nearly all retro bead⁺ GP cells (red) are *Vgat*^{i-Cre+} or *GAD2*^{i-Cre+} (green). A subset of these are also ChAT⁺ (solid circles) and the remainder are ChAT⁻ (dashed circles). *Top*, low magnification sagittal view of the GP. *Bottom*, a single confocal plane from stacks used to quantify marker co-localization.

d. Summary of co-expression of *Vgat*^{i-Cre} (n=3 mice) and/or ChAT (n=5 mice) in retro bead⁺ GP neurons.

Figure 4.1 (Continued)

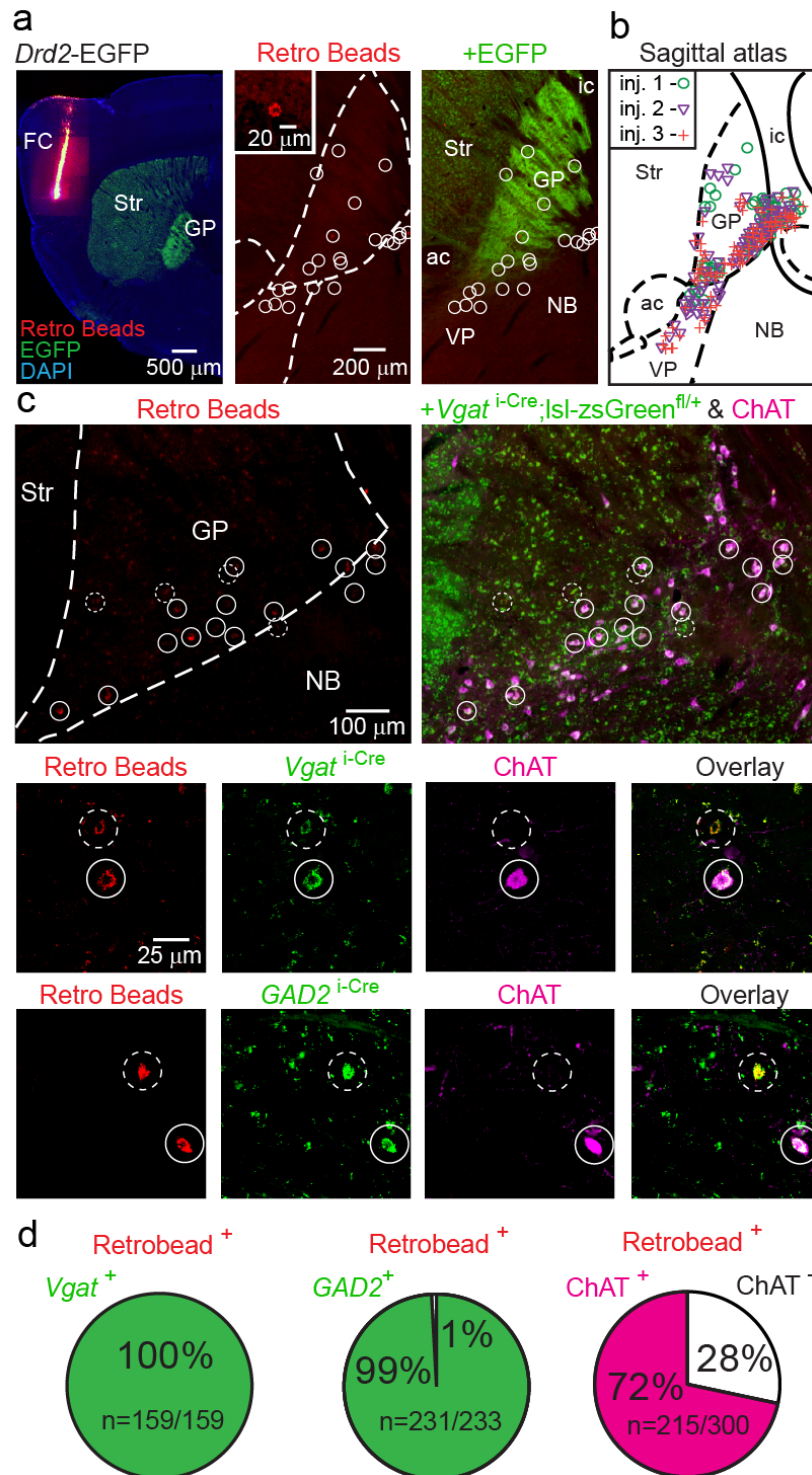


Figure 4.2. Anatomical and molecular properties of GP-FC cells and ChAT⁺ cells of the Substantia Innominata (SI) and Ventral Pallidum (VP).

a-c. GP-FC cells project exclusively to ipsilateral cortex.

a. Low magnification horizontal section from a wild type mouse injected bilaterally in FC with red (right hemisphere) and green (left hemisphere) retro beads. DAPI (blue), nuclear stain. Boxed insets show location of GP in **b**. Green signal in the right hemisphere is due to bleed through from the red channel.

b. High magnification of left and right GP from the same brain as in **a**. Retro bead⁺ cells from ipsilateral (ipsi) and contralateral (contra) injections are highlighted with white circles. Dashed lines demarcate the approximate boundaries of the GP.

c. Summary graph showing nearly all bead⁺ cells (n=436 of 437) resulted from injections in ipsilateral FC (n=4 mice).

d-e. ChAT⁺ neurons of the substantia innominata (SI) and ventral pallidum (VP) express the vesicular GABA transporter gene (*Vgat*) and glutamic acid decarboxylase 2 (*GAD2*).

d. *Top*, low magnification ventral view of a sagittal section from a *Vgat*^{i-Cre/+}; *Rosa26*^{lsl-zsGreen/+} mouse immunostained for ChAT. *Bottom*, high magnification view of the SI and bordering VP.

e. Similar high magnification view of SI/VP area in a *GAD2*^{i-Cre/+}; *Rosa26*^{lsl-zsGreen/+} mouse immunostained for ChAT.

f-h. ChAT⁻ GP-FC cells do not express Parvalbumin (PV).

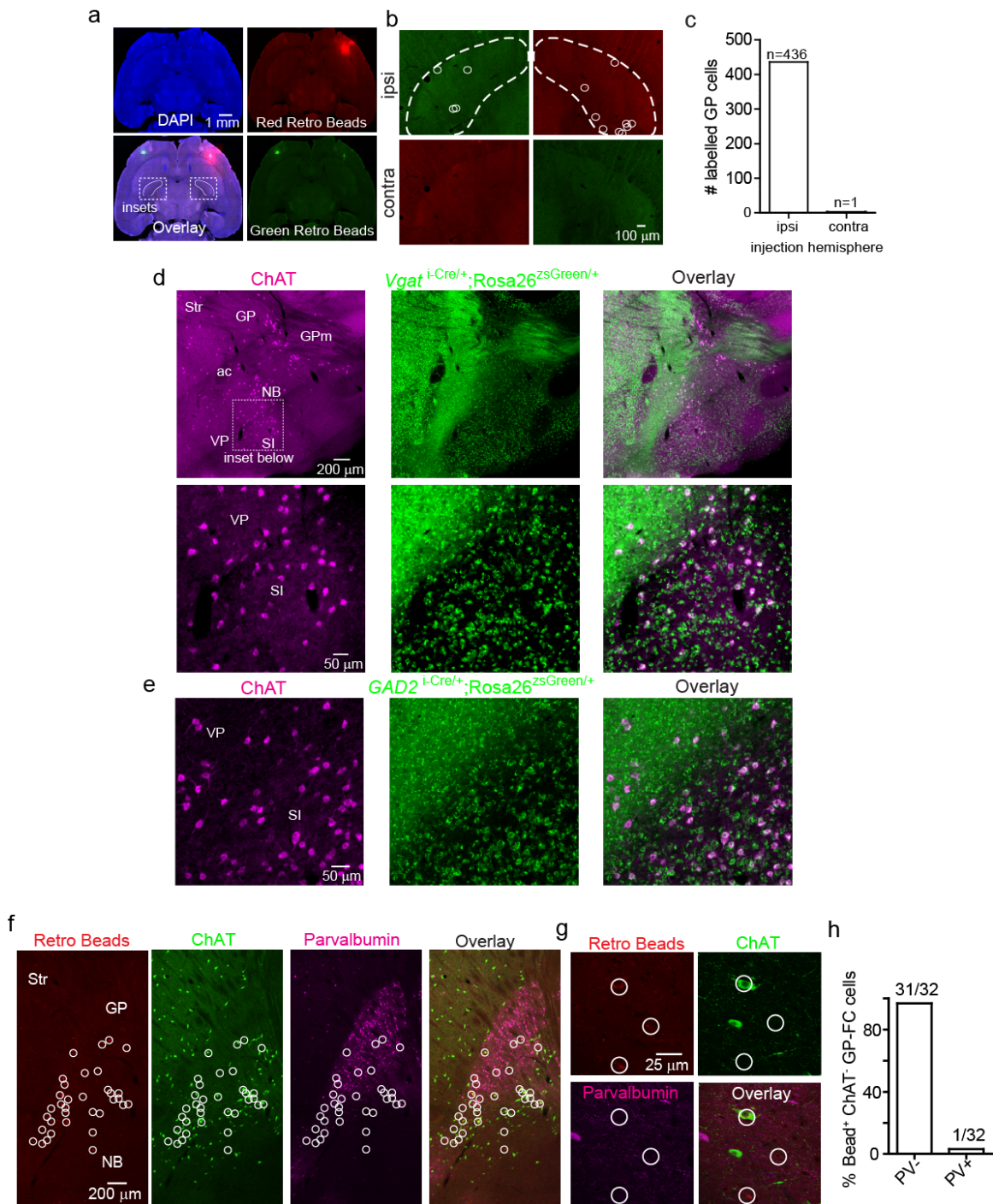
Figure 4.2 (Continued)

f. Low magnification view of sagittal section through the GP of a wild type mouse injected with retro beads (red) in FC and immunostained for ChAT (green) and PV (magenta). White circles highlight bead⁺ GP-FC cells.

g. A single confocal plane showing bead⁺ GP-FC cells (circled in white) and immunostaining for ChAT and PV.

h. Confocal quantification of co-localization between bead⁺ ChAT⁻ GP-FC cells and PV (n=2 mice).

Figure 4.2 (Continued)



ChAT⁺ cells throughout the NB and Substantia Innominata were also *Vgat*⁺ and *GAD2*⁺ (Figure 4.2d,e), suggesting that much of the basal forebrain cholinergic system may release GABA in addition to ACh²⁶. ChAT⁻ GP-FC cells did not express the calcium binding protein parvalbumin (PV) (Figure 4.2 1f-h), indicating that GP-FC cells are distinct from both the GP neurons that project to posterior BG nuclei²⁷ and the other non-cholinergic cortical projecting cells found across the basal forebrain^{1,28,29}.

To determine if ChAT⁺ and ChAT⁻ GP-FC cells are conserved in higher mammals, we performed retrograde tracing followed by ChAT immunostaining in a *rhesus macaque*. We targeted cortical areas innervated by NB neurons adjacent to the GP^{2-4,30} (Figure 4.3a,b) and observed tracer⁺ neurons in the GP and bordering NB that were ChAT⁻ and ChAT⁺ (Figure 4.3c-e). In the macaque and mouse, ChAT⁺ cells were similarly distributed around the GP and GP/NB border (Figure 4.3d,g). In the mouse, iSPN axons abut ChAT⁺ cells bordering the GP and arborize in the dorsal NB (Figure 4.3g). We conclude that ChAT⁺ and ChAT⁻ cortical projection neurons within the GP/dorsal NB are conserved and ideally positioned to be innervated by iSPNs.

To determine if ChAT⁻ and ChAT⁺ cells have distinct circuit functions, we compared their cortical projection patterns and electrophysiological properties. Differential labeling of GP-FC cells in *ChAT*^{i-Cre/+} mice was accomplished using recombinant adeno-associated viruses (rAAVs) to selectively express fluorophores in intermingled Cre⁺ and Cre⁻ neurons^{5,31} (Figure 4.4a-f). The brains of mice with injections of rAAVs confined to the GP and adjacent NB were reconstructed in three-

Figure 4.3. ChAT+ and ChAT- GP-FC cells are present in a *rhesus macaque*.

- a.** In order to label frontal cortical projection neurons from Ch4iv and Ch4id regions of the NB adjacent to the GP³⁰, the neuronal tracer biotinylated dextran amine (BDA) was injected at multiple sites along the arcuate and principal gyri and in the orbital cortex. *Left*, dorsal (*top*) and ventral (*bottom*) views of a fixed *macaque* brain. Dashed boxes indicate the injected areas. *Right*, schematic of the injection sites. Blue circles correspond to 2 x 0.5 μ l BDA injections at 1 and 2 mm below the pial surface. **b.** Coronal section through the injection area after immunostaining to visualize BDA. **c-e.** Immunostaining for BDA and ChAT identifies retrogradely labeled ChAT+ and ChAT- GP-FC cells.
- c.** Coronal section from *Macaque* atlas containing GP and NB.
- d.** *Left*, ChAT immunostaining highlights traditional anatomical boundaries of the GP/Putamen and GP/NB. Same plane as in **c.** *Right*, higher magnification view of GP/NB border corresponding to the inset in **c.** ChAT+ neurons are distributed around the ventral GP/dorsal NB and along laminae separating the GP from the Putamen (lateral medullary laminae, lml) and GPi (medial medullary laminae, mml). Arrow and arrowhead indicate approximate locations of BDA⁺ChAT⁺ (680 μ m anterior) and BDA⁺ChAT⁻ (360 μ m anterior) example GP-FC cells shown in **e.**
- e.** Single confocal planes showing example BDA⁺ChAT⁺ and BDA⁺ChAT⁻ GP-FC cells.
- f,g.** ChAT immunostaining in a *Drd2*-EGFP mouse distinguishes traditional anatomical boundaries of the GP/NB from the territory occupied by iSPN axons.
- f.** Coronal section from the mouse atlas.

Figure 4.3 (Continued)

g. *Left*, ChAT immunostaining highlights traditional anatomical boundaries of the GP/Striatum and GP/NB. Same plane as in **f**. *Right*, higher magnification view of GP/NB border region corresponding to the inset in **f**. As in *Macaque*, ChAT⁺ cells are distributed along GP borders between striatum and the internal capsule (ic) and at the border of ventral GP/dorsal NB. Overlay of GFP fluorescence demonstrates iSPN axons arborize throughout the GP, abutting ChAT⁺ cells on the GP border regions (arrow), and ventrally in the dorsal NB (arrowhead). AA, anterior amygdaloid area; ac, anterior commissure posterior; CeL, central lateral division of amygdala; CeM, central medial division of amygdala; GP, globus pallidus externus; GPi, globus pallidus internus; Lh, lateral

Figure 4.3 (Continued)

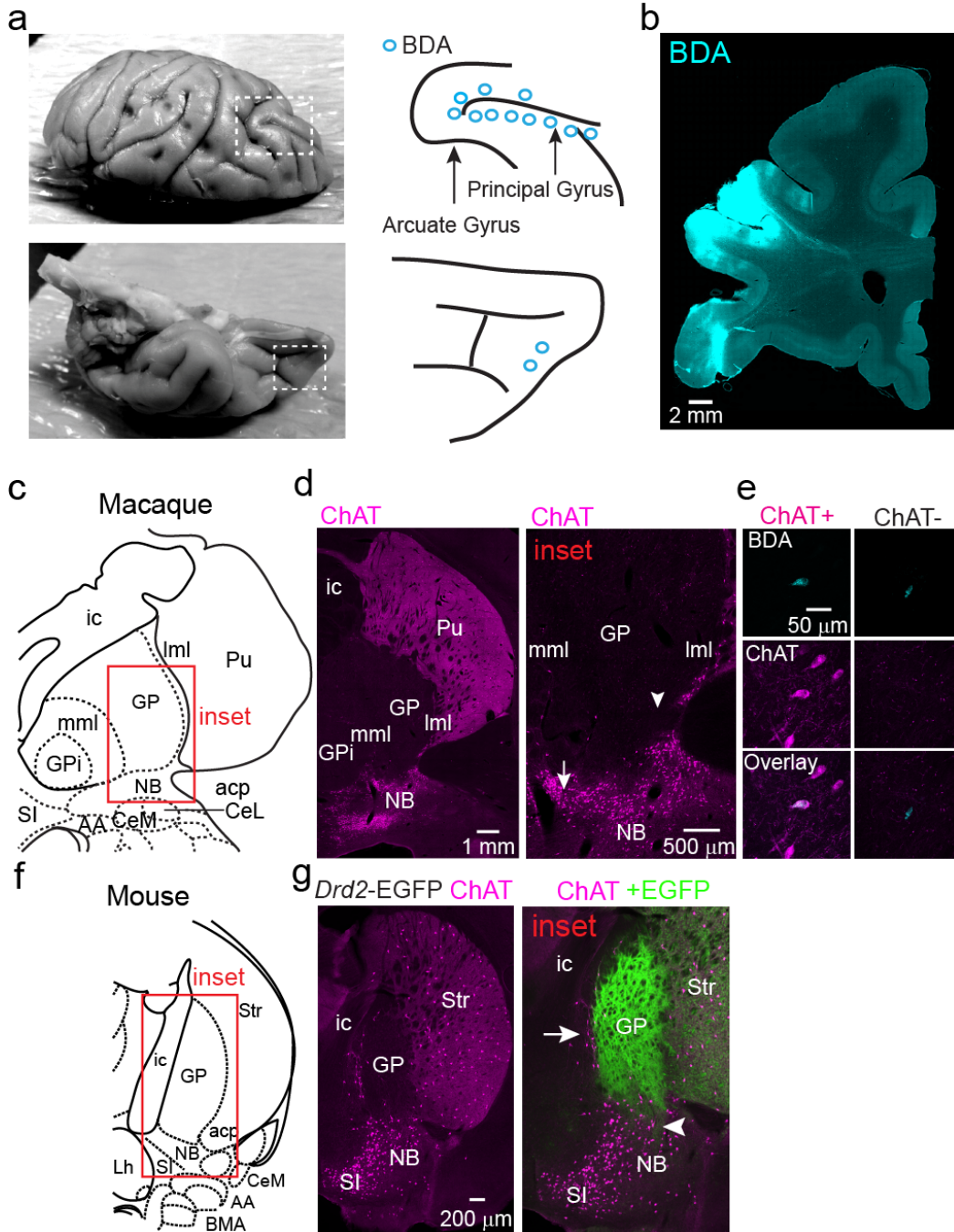


Figure 4.4. Validation of $ChAT^{i-Cre}$ knock-in mouse and rAAV strategy for Cre-On/Off labeling of GP-FC cells.

a-c. The $ChAT^{i-Cre}$ mouse expresses Cre selectively in $ChAT^+$ GP/NB neurons with high penetrance.

a. *Left*, low magnification view of sagittal section through $ChAT^{i-Cre/+};Rosa26^{lsl-tdTomato/+}$ mouse immunostained for ChAT. *Right*, inset showing higher magnification view of the GP and NB. Dashed line approximates the boundaries for quantifying Cre-reporter and ChAT co-localization.

b. Single confocal plane showing overlap of Cre-reporter expression and ChAT immunostaining of $ChAT^+$ cells at the GP/NB border.

c. Quantification of confocal co-localization between the Cre-reporter and ChAT (n=3 mice).

d-f. Transduction of the GP in a $ChAT^{i-Cre/+}$ mouse with DIO-EGFP (Cre-On) and FAS-tdTomato (Cre-Off) rAAVs effectively targets GFP and tdTomato to $ChAT^+$ and $ChAT^-$ cells respectively.

d. Sagittal section through the GP following transduction of the DIO-EGFP (green) and FAS-tdTomato (red) rAAVs and immunostaining for ChAT (magenta).

e. Single confocal plane showing $ChAT^+$ cells (circled in white) co-localized with GFP but not tdTomato.

f. Quantification of confocal co-localization between ChAT, GFP and tdTomato (n=2 mice).

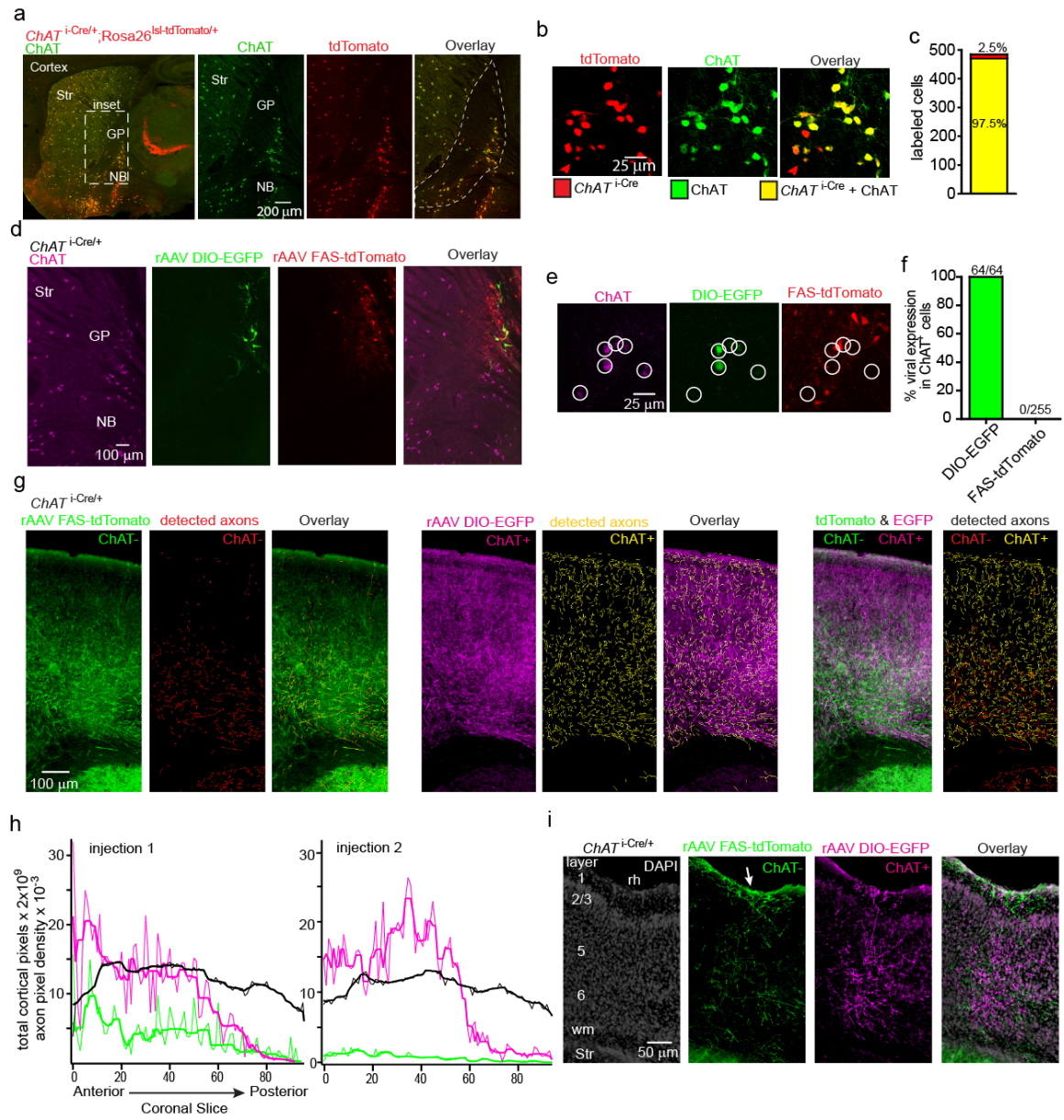
Figure 4.4 (Continued)

g. Coronal section of anterior M1 illustrating automated axon detection of ChAT- and ChAT+ axons.

h. Densities of detected ChAT- (green) and ChAT+ (magenta) axons along with total cortical area (black) in successive 50 μm coronal slices (anterior-posterior) across the cortical mantle (n= 2 mice). Densities and area are shown raw (thin line) and after 5 point median filtering (thick line).

i. Coronal section illustrating the distribution of GP-FC axons across layers of ectorhinal cortex, a posterior cortical area that receives a large GP-FC projection. ChAT- axons target superficial layers 1 and 2/3 (arrow), in addition to deeper layers 5 and 6, as in anterior cortices including M1. The ChAT+ axons arborize across all cortical layers in both ectorhinal and anterior cortical areas. rh, rhinal fissure; Str, striatum; wm, white matter.

Figure 4.4 (Continued)



dimensions, cortical axons were computationally detected (Figure 4.4g), and axonal densities were quantified across cortical areas and layers (n=2 mice) (Figure 4.5a,b and B.Movie 1). ChAT+ and ChAT- cells send a pronounced projection to FC (Figure 4.5c and Figure 4.4h), targeting different but overlapping cortical areas (Figure 4.5d) and layers (Figure 4.5e). In anterior primary motor cortex (M1), ChAT+ axons arborize in layers 1-6, most densely in layers 1 and 2/3, whereas ChAT- axons arborize densely in layers 5 and 6, sparsely in layer 2/3 and are absent from layer 1. This layer distribution is representative of most but not all cortical areas. In cingulate cortex, which receives a strong GP-FC projection, ChAT- axons extend into layer 1 (Figure 4.4i). GP-FC cells also target distinct but overlapping subcortical nuclei. ChAT+ cells arborize in the thalamic reticular nucleus (Rt), the basolateral amygdala (BLA) and the substantia nigra reticulata/compacta (SNr/c). ChAT- cells target the striatum (Str), subthalamic nucleus (STN) and Substantia Nigra reticulata (SNr), as well as the lateral amygdala (LA) and BLA, lateral habenula (LH) and thalamic Rt and parafascicular nuclei (PF) (Figure 4.6).

To determine electrophysiological and morphological properties of ChAT+ and ChAT- GP-FC cells, we identified these cells in acute brain slices following FC retrograde bead labeling in *ChAT*^{i-Cre/+};*Rosa26*^{Isl-tdTomato/+} mice and made whole-cell current-clamp recordings followed by two-photon imaging of neuronal morphology (Figure 4.5f).

ChAT+ and ChAT- cells differed significantly in several aspects (Figure 4.5g-i and Figure 4.7a-e): ChAT- cells have smaller somata than ChAT+ cells (Figure 4.5g) and exhibit a hyperpolarization activated cation current (I_h), whereas ChAT+ cells do not. Compared

Figure 4.5. GP-FC cells are distinguished by cortical projection patterns and electrophysiological properties.

a-e. GP-FC axons arborize in distinct areas and layers of FC.

a. Coronal sections of a *ChAT*^{i-Cre/+} mouse injected in GP with rAAVs DIO-EGFP (Cre-On, magenta) and FAS-tdTomato (Cre-Off, green) sampled from a whole-brain reconstruction. The injection site (GP, shown in **b**) and anterior primary motor cortex (M1, shown in **e**) are indicated along with other BG nuclei. Str, striatum; Rt, thalamic reticular nucleus; STN, subthalamic nucleus; SNr, substantia nigra reticulata.

b. *Left*, coronal atlas. *Right*, injection site showing ChAT+ (Cre-On) expression limited to GP and the immediately adjacent NB. ChAT- (Cre-Off) expression is limited to GP with slight leak in striatum. ChAT+ and ChAT- axons arborize in Rt. SI, substantia innominata; NB, nucleus basalis; ic, internal capsule.

c. Anterior-posterior distribution of normalized, median filtered ChAT+ and ChAT- axonal densities across the cortical mantle (n= 2 mice; solid lines, injection 1; dotted lines, injection 2).

d. Average density of ChAT+ and ChAT- GP-FC axons by cortical area. FrA, frontal association; PrL, prelimbic; MO, medial orbital; LO, lateral orbital; VO, ventral orbital; GI/DI, granular/dysgranular; AI, agranular insular; M1, primary motor; M2, secondary motor; S1, primary sensory; S2, secondary sensory; Cg, cingulate; IL, infralimbic; DLO, dorsolateral orbital; Pir, piriform; A2, secondary auditory; A1, primary auditory; RS retrosplenial; V1, primary visual; V2, secondary visual; TeA, temporal association; PTA, parietal; Ent, entorhinal; Ect, ectorhinal; PRh, perirhinal.

Figure 4.5 (Continued)

e. *Left*, distribution of GP-FC axons across layers of anterior primary motor cortex (M1).

Right, line scan of average fluorescence across layers, normalized to peak and baseline subtracted by white matter signal.

f. ChAT⁺ and ChAT⁻ GP-FC cells are distinguishable in acute slices following green retro bead injection in FC of *ChAT^{i-Cre};Rosa26^{lsl-tdTomato/+}* mice.

g. ChAT⁺ cells have larger soma than ChAT⁻ cells. *Left*, maximum intensity 2-photon projections of soma after whole-cell recording. *Right*, quantification of soma volumes (P18-22; n=8 ChAT⁺ cells, n=8 ChAT⁻ cells).

h. Example membrane voltage traces for GP-FC cells (P18-22) following positive (ChAT⁺:1.7; ChAT⁻:0.9 nA) and negative (ChAT⁺:-0.2; ChAT⁻:-0.1 nA) current injections (500 ms) to determine maximum firing rates and hyperpolarized membrane properties.

i. Whole-cell spontaneous firing rates (P13-56; n=45 ChAT⁺ cells, n=35 ChAT⁻ cells).

Asterisk, P<0.05 (Mann-Whitney).

Figure 4.5 (Continued)

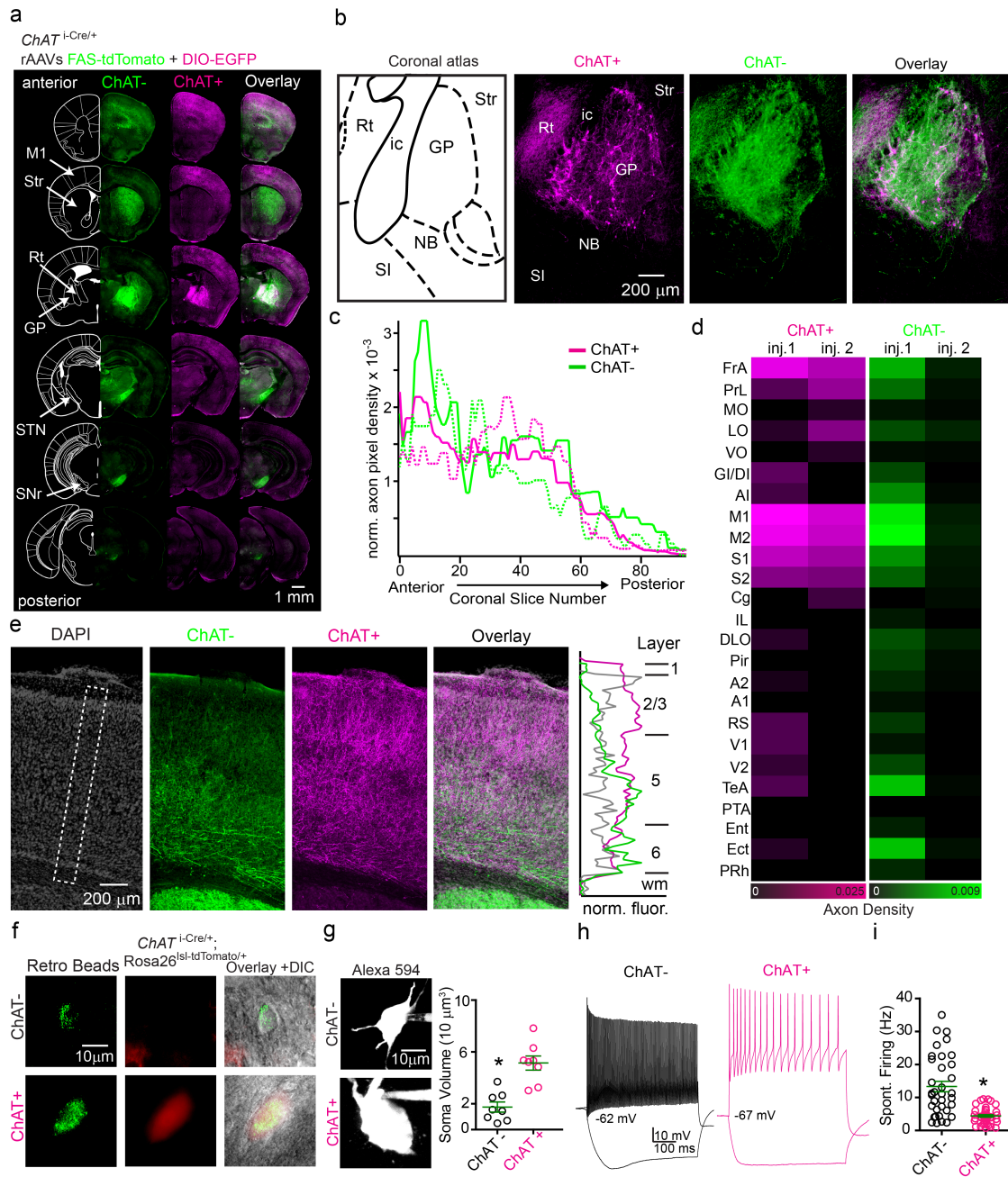


Figure 4.6. ChAT⁺ and ChAT⁻ GP-FC cells target distinct but overlapping subcortical nuclei.

a. Coronal sections from a three dimensional brain reconstructions illustrating subcortical nuclei targeted by ChAT⁺ and ChAT⁻ axons following transduction of *ChAT*^{i-Cre} GP/dorsal NB with rAAVs DIO-EGFP (green, Cre-On) and FAS-tdTomato (magenta, Cre-Off)(n=2 mice, examples from inj. 1). *Left*, coronal atlas. *Right*, high magnification views of subcortical nuclei.

Figure 4.6 (Continued)

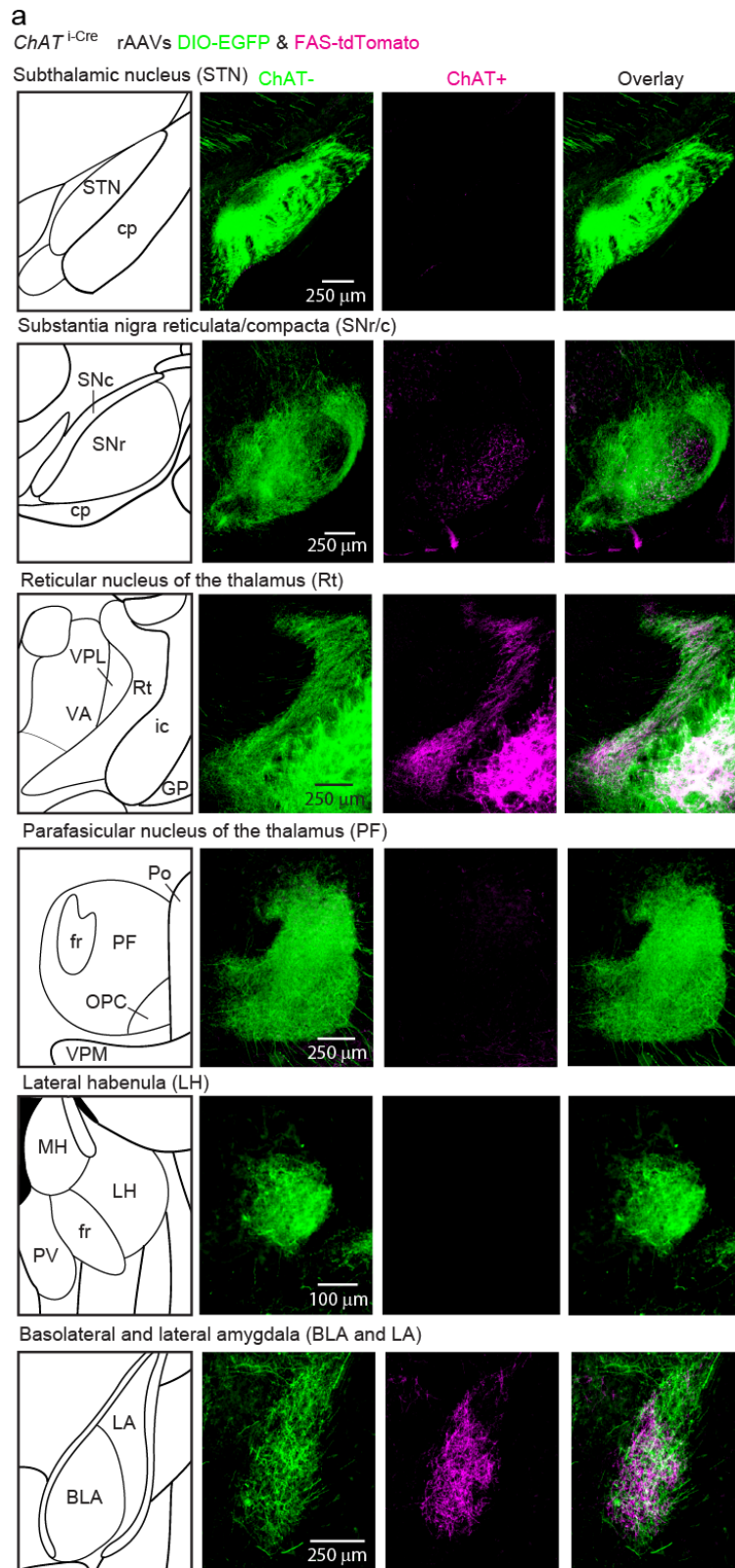


Figure 4.7. GP-FC cells are distinguished by active and passive membrane properties.

a. Maximum intensity 2-photon projections of ChAT- (*left*) and ChAT+ (*right*) GP-FC cells following whole-cell recording. Dashed insets show high magnification projections through dendrites.

b. Passive membrane properties of GP-FC cells (P18-22; n=9 ChAT-, n=10 ChAT+).

c. Representative waveforms of spontaneously active ChAT- and ChAT+ GP-FC cells.

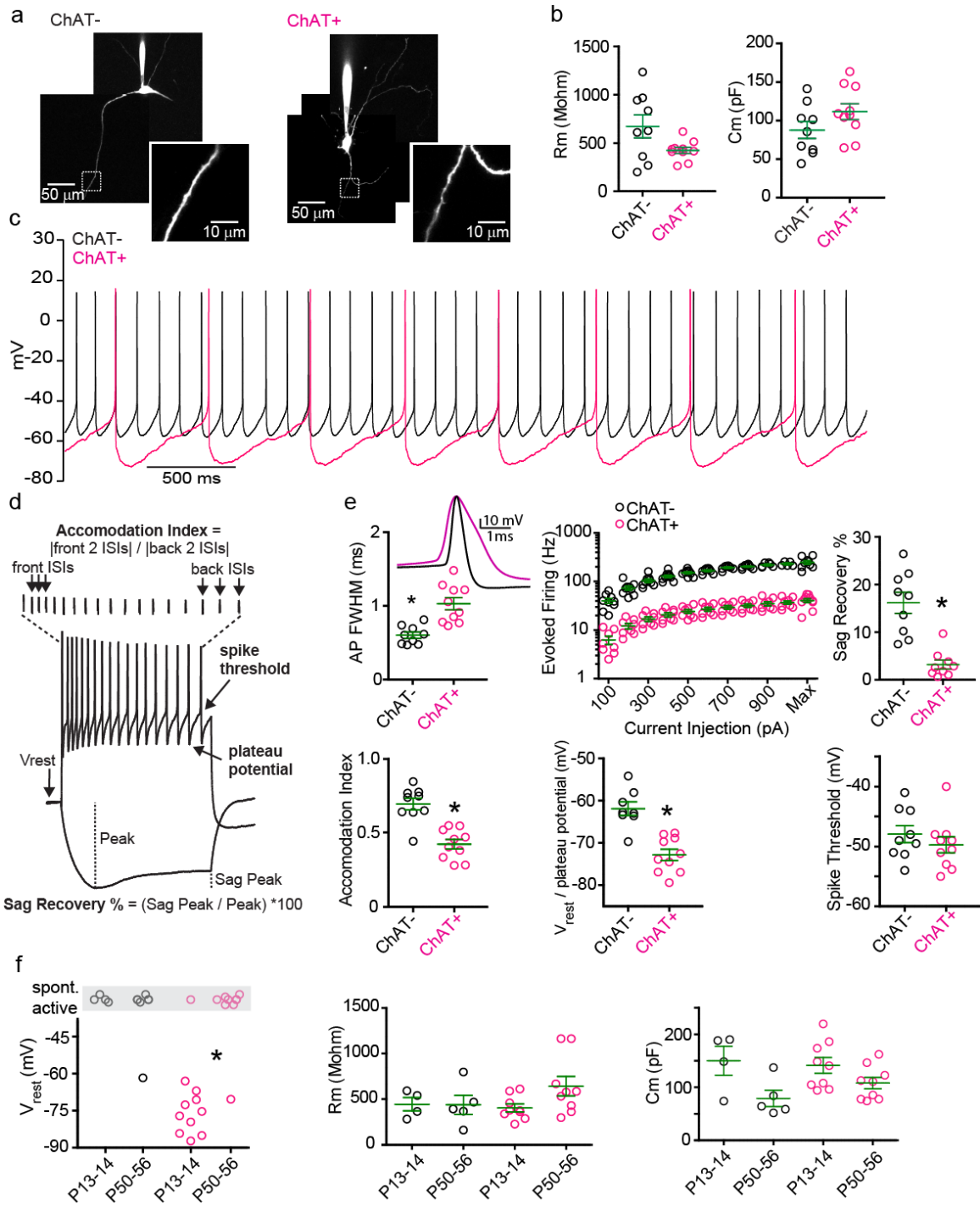
d. Schematic of quantified membrane properties following positive and negative current injections. ISI, interspike interval.

e. Active membrane properties of GP-FC cells (P18-22; n=8-9 ChAT-, n=10 ChAT+).

Representative action potential waveforms from a spontaneously active ChAT- cell or from minimal current injection in a ChAT+ cell. Evoked firing rates were calculated for 500 ms current injections.

f. Developmental comparison of GP-FC membrane properties before (P13-14) and around (P50-56) sexual maturity. *Left*, ChAT- GP-FC cells are spontaneously active throughout post-natal development (P13-14, n= 4; P50-56, n=5), while ChAT+ cells tend to become spontaneously active after sexual maturity (P13-14, n= 11; P50-56, n=8). GP-FC membrane resistance (*middle*) does not change before and after sexual maturity but membrane capacitance (*right*) is reduced (ChAT-: P13-14, n= 4; P50-56, n=5; ChAT+: P13-14, n= 9; P50-56, n=9). Asterisk, $P < 0.05$ (Fisher's Exact test); Bars denote mean \pm s.e.m.

Figure 4.7 (Continued)



to ChAT+ cells, ChAT- cells have narrower action potentials, higher maximum firing rates (~200 vs. 30 Hz) and less spike accommodation (Figure 4.5h). Finally, ChAT- cells were spontaneously active at all ages studied, whereas ChAT+ cells become spontaneously active around sexual maturity (Figure 4.7f). Once spontaneously active, ChAT+ cells have lower firing rates than ChAT- cells (4.4 ± 0.39 vs. 13.3 ± 1.6 Hz) (Figure 4.5i). We conclude that while all GP-FC cells are *Vgat*⁺ and *GAD2*⁺, ChAT expression distinguishes two physiologically distinct cell types that are anatomically positioned to differentially affect cortical and sub-cortical activity during post-natal development and in adulthood.

To determine if GP-FC cells influence cortical activity *in vivo*, we recorded extracellular spiking across layers in FC of mice performing a motor reward task and compared cortical firing rates during non-motor epochs with and without optogenetic activation of ChAT+ GP-FC neurons. *Chat*^{i-Cre} mice were injected in the GP and adjacent NB with Cre-On rAAV carrying the light-gated cation channel channelrhodopsin fused to mCherry (ChR2-mCherry) or mCherry alone and trained on the task until proficient (Figure 4.8). Pulsed activation (3s 10 Hz train of 473 nm light) of ChR2⁺ somata in GP through an implanted fiber (Figure 4.9a) increased the firing rates of individual cortical units (Figure 4.9b) (n=15 of 106 increased, mean firing rate with stimulation $145 \pm 14\%$ of firing rate without; n=2 of 106 decreased, mean change $71 \pm 0.2\%$), and this increase was not observed in GP neurons expressing mCherry alone (n=0 of 73 units increased). Light also shifted the mean firing rate of the population as a whole (ChR2: $112 \pm 3\%$ compared to no light condition; mCherry $96 \pm 2\%$) (Figure 4.9c,d), but did not consistently modulate activity associated with tones or lever presses (data not show).

Figure 4.8. Optogenetic manipulations of GP-FC cells coupled with *in vivo* extracellular FC recordings in awake behaving mice.

- a.** Schematic of the training and testing task designs. After the start of the task, if the mouse refrains from pressing a lever for a variable length period ($T_{nopress}=1.5-5$ s, red), then a 10 kHz tone is played (“cue”). Following the cue is a reward period ($T_{reward}=1.5-10$ s, green) in which the animal receives a water drop if it presses and releases the lever. During training the duration $T_{nopress}$ and T_{reward} are progressively and dynamically adjusted based on the animals performance to shape its behavior and reaction times. Throughout training $T_{nopress}$ is randomly varied to prevent an interval timing strategy, while ΔT_{reward} is reduced to keep the task challenging for the animal. Furthermore, the volume of water per reward (V) is proportional to reaction time ($\Delta T_{reaction}$, measured from the end of the tone to the level release) such that $V=8\ \mu\text{l}$, if $\Delta T_{reaction} < 200$ ms, linear decreases to $4\ \mu\text{l}$ up to $\Delta T_{reaction}=1\text{s}$, and further linearly decreases to $2\ \mu\text{l}$ at the maximally allowed $\Delta T_{reaction}$.
- b.** For behavioral testing and recordings sessions, a static version of the task is used in which $T_{nopress}$ is randomly chosen from 1.5-3 s, $\Delta T_{reaction}=1.5$ s, $V=4\ \mu\text{l}$.
- c.** Raster plot (*top*) and summary histogram (*bottom*) of lever presses times relative to the tone ($t=0$) for a single testing session of a well-trained animal.

Figure 4.8 (Continued)

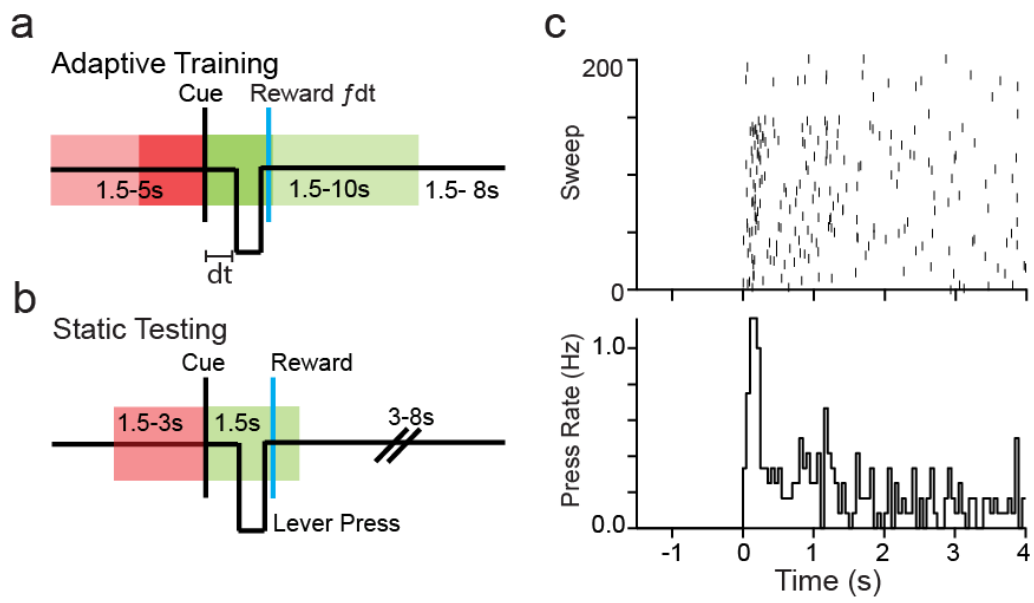


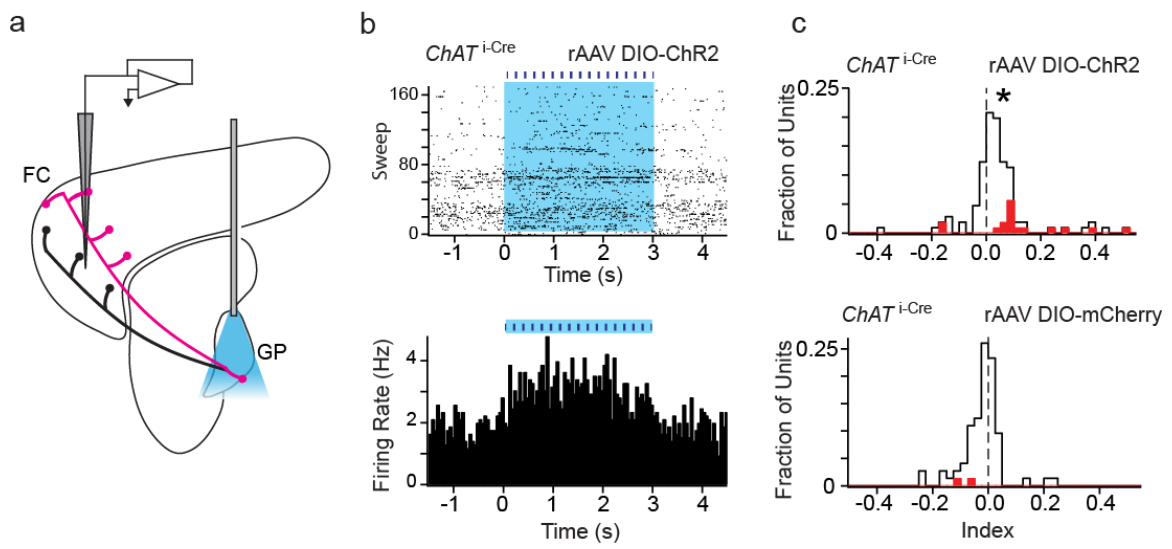
Figure 4.9. ChAT+ GP-FC cells activate FC *in vivo*

a. Schematic for *in vivo* recording combined with optogenetic stimulation. 473 nm light was delivered to GP with a chronically implanted fiber, while a 16 or 32 channel silicon probe was lowered to ~1000 μm below the pia to record extracellular spiking in FC.

b. Example unit in FC activated by 5 mW of 473 nm light (3s 10 Hz train, 6s inter-trial interval). Raster plot (*top*) and histogram (*bottom*) includes only trials where no lever presses were detected from 3s prior to 3s after light onset.

c. ChR2 (*top*) and mCherry control (*bottom*) index of modulation histograms for all units (ChR2: n=106 units, 3 mice; mCherry, n=73 units, 2 mice). Index is based on the Firing Rate (FR) of cells during the entire light on period, calculated as $(FR_{\text{ON}} - FR_{\text{OFF}}) / (FR_{\text{ON}} + FR_{\text{OFF}})$. Dashed vertical line indicates no FR modulation. Rightward shifts indicate increases and leftward shifts decreases in FR due to light. Red bars indicate cells that were statistically significantly modulated on the trial by trial basis, $P < 0.05$ (Students T test). Asterisk indicates a statistically significant change in population FR, $P < 0.0001$ (Kruskal-Wallis with Dunn's Multiple Comparison Test).

Figure 4.9 (Continued)



We conclude that action potentials in ChAT+ GP-FC neurons are sufficient to increase firing in FC of an awake, behaving mouse.

To determine the synaptic mechanisms by which GP-FC cells activate cortex, we sought to define the neurotransmitters released by each cell type. We introduced the ChR2 into ChAT- or ChAT+ GP-FC cells by injecting rAAVs transcriptionally activated or inactivated by Cre^{6,31} into the GP and adjacent NB of *ChAT*^{i-Cre/+}; *GAD67*^{GFP/+} mice ([Figure 4.10a](#) and [Figure 4.11a](#)). To characterize the currents produced by GP-FC axon stimulation, we cut acute brain slices and made whole-cell voltage-clamp recordings from somata within 150 μm of ChR2⁺ axons ([Figure 4.10b](#)).

Recordings post-synaptic to ChAT- axons were made in FC at ~ 0 mV (the reversal for ionotropic glutamate and nicotinic receptors) and in the presence of NBQX and CPP to block ionotropic glutamate receptors. In a subset of neurons ($n=5$ of 94), optogenetic activation evoked fast outward currents ([Figure 4.10c](#)). These light-evoked inhibitory post-synaptic currents (IPSCs) were blocked by the voltage-gated sodium Na⁺ blocker tetrodotoxin (TTX), demonstrating ChR2 depolarization alone was not sufficient for transmitter release. IPSCs could be rescued in the continued presence of TTX by enhancing ChR2 mediated depolarization of terminals with application of the voltage-gated K⁺ channel blocker 4-aminopyridine (4AP) and were abolished in the presence of the GABA_A receptor antagonist SR95531, indicating direct (monosynaptic) release of GABA by ChAT- cells.

In addition to a cortical projection, ChAT+ cells ramify local axons at the GP/NB border ([Figure 4.11b-d](#)). We took advantage of this axonal convergence to

Figure 4.10. GP-FC cells release GABA and ACh in FC

- a.** Illustration of cortical (ChAT+ and ChAT-) and local (ChAT+) GP-FC axons expressing ChR2-mCherry after rAAV transduction in $ChAT^{i-Cre/+}$ GP. Labeled areas were targeted for paired whole-cell recordings and optogenetic activation.
- b.** Max projection confocal stack (30 μm) of ChAT+ axons in FC layer 6 following transduction of rAAV DIO-ChR2-mCherry in GP of $ChAT^{i-Cre};GAD67^{GFP/+}$ mouse. Whole-cell recordings were targeted to somata within 150 μm of the ChR2⁺ arbors. GFP fluorescence helped identify GABAergic interneurons (GFP⁺) or non-GABAergic pyramidal neurons (GFP⁻).
- c.** *Top left*, currents in a layer 6 interneuron held at indicated potentials evoked by optogenetic activation of surrounding ChAT- axons under baseline conditions (NBQX and CPP) and following co-application of (from *left to right*) TTX, 4AP and SR95531. *Top right*, IPSC peak amplitudes across conditions normalized to baseline (n=5 cortical interneurons). *Bottom left*, evoked current responses in a ChR2⁻ neuron at the GP/NB border held at indicated potentials to optogenetic activation of surrounding ChAT+ cells under baseline conditions (ACSF) and following co-application of (from *left to right*) glutamate (NBQX & CPP) and nicotinic (MEC, MLA & DH β E) receptor antagonists, TTX, 4AP and SR95531. *Top right*, IPSC peak amplitudes across conditions normalized to baseline (n=7 ChR2⁻ GP/NB cells).

Figure 4.10 (Continued)

d. Maximum intensity projection of dendritic morphology following whole-cell recording used to identify FC neurons as pyramids or interneurons. *Top*, a layer 5 pyramidal neuron. *Bottom*, a layer 1 interneuron.

e. Ionotropic synaptic connectivity screen for cortical neurons with monosynaptic GABAergic (present in TTX/4AP or <3.1ms onset latencies) or nicotinic ChR2-evoked current responses from ChAT+ or ChAT- axons. ChAT- data includes cells in [Figure 4.10c](#).

f-k. Co-localization analysis of virally labeled ChAT+ axon terminals in FC using array tomography.

f. Maximum projection stack ($z=2.17\ \mu\text{m}$, 70 nm sections) through layers 1 and 2/3 of frontal cortex following injection of rAAV DIO-Synaptophysin-GFP into the GP of a *ChAT^{i-Cre/+}*. GFP signal resembles “pearls on a string,” indicating GFP is targeted to vesicles and is accumulated in pre-synaptic terminals along individual axonal branches. Boxed inset shows a high magnification view of a labeled axon from layer 1 (*left*) and a single 70 nm plane with diffraction limited immunohistochemical labeling of Gephyrin, PSD-95, VGAT and VAcHT. Arrowheads indicate the two example pearls in **g**.

g. Three consecutive z-planes illustrating marker association with GFP⁺ pearls shown in **f**. Example pearls about the post-synaptic marker Gephyrin but not PSD-95 and contain both VGAT and VAcHT puncta (arrowheads).

Figure 4.10 (Continued)

h. Quantification of mean occurrence between GFP⁺ pearls and synaptic markers for voxels located within the pearl (0 distance) and 1-5 pixels away (102-512 nm). Mean occurrences for the real data (crosses) are compared to mean occurrence following 1000 rounds of marker randomization (lines, error bars denote 99% confidence intervals). Crosses above or below the error bars indicate positive or negative occurrences respectively.

i. summary (n=8 stacks) quantifying the difference in 0 distance occurrence distributions between GFP⁺ pearls and individual synaptic markers for the real data and following 10 rounds of randomization of GFP⁺ pearls. Positive Z scores indicate higher occurrence in the real data. Asterisk, P<0.001 for all stacks compared.

j. Distances between the centroids of VGAT and VAcHT puncta within the same GFP⁺ pearl (n=1,851 comparisons). Plot excludes singleton values between 1.2-1.6 μm (n=8).

k. *Left*, maximum projection of GFP⁺ labeled axon from stack shown in **a**. *Right*, GFP⁺ pearls color-coded by VGAT/VAcHT identity following automated detection.

Figure 4.10 (Continued)

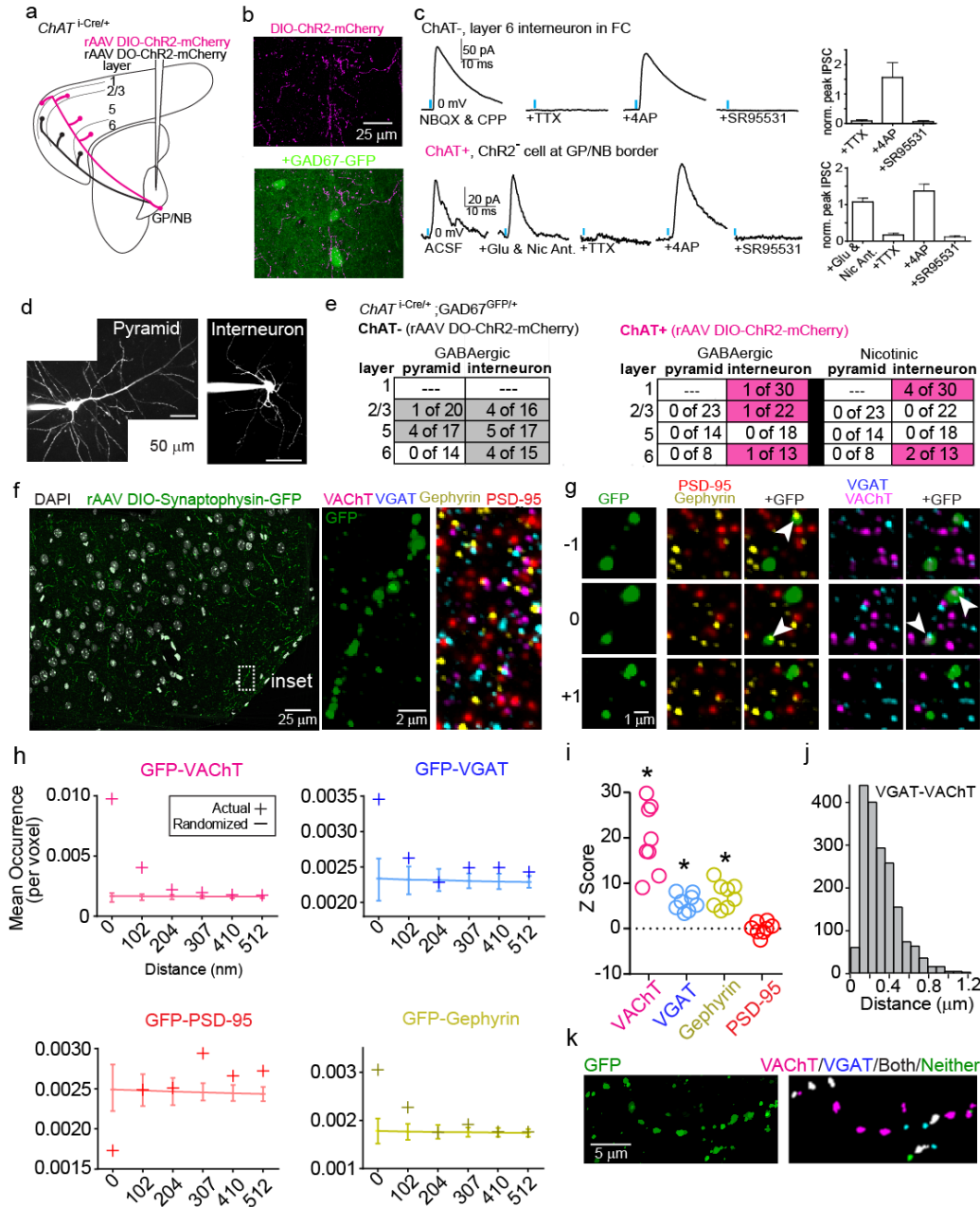


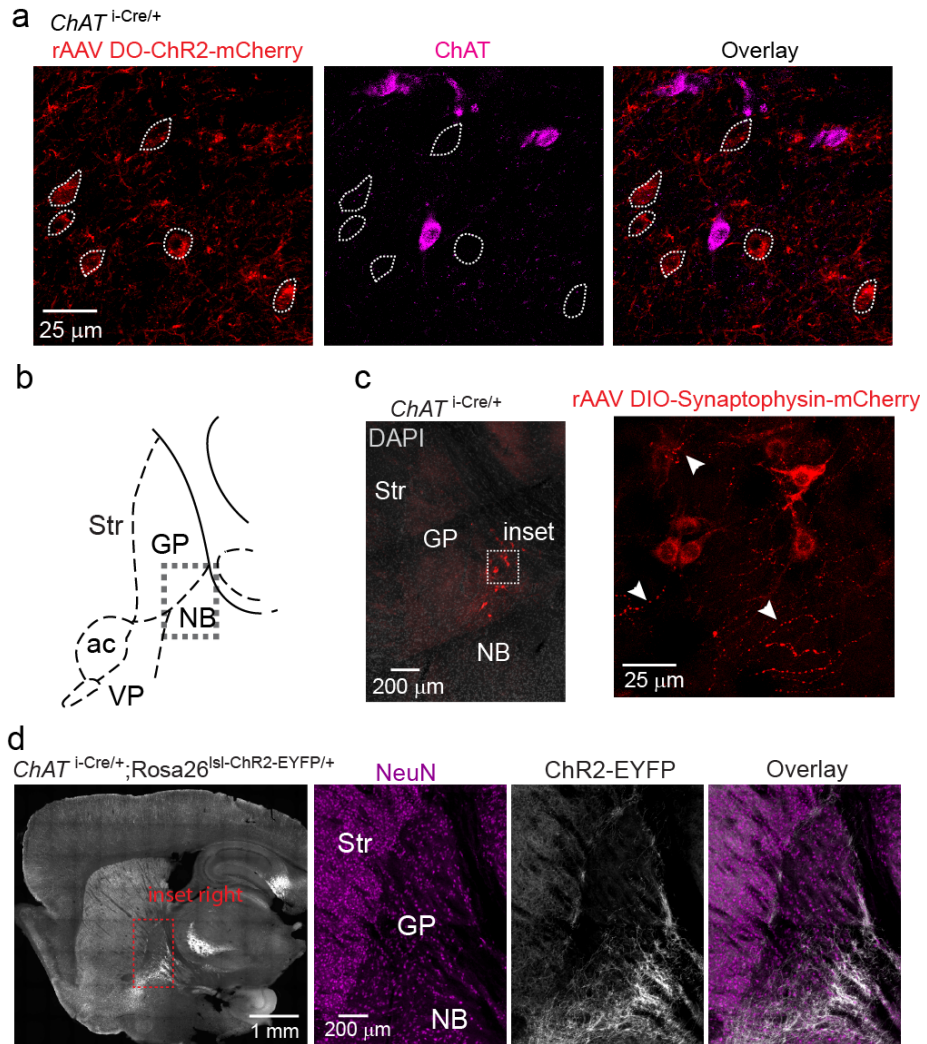
Figure 4.11. ChAT+ GP-FC cells ramify local axon collaterals around the GP/NB border.

a. rAAV DO-ChR2-mCherry transduced into the $ChAT^{i-Cre/+}$ GP expresses ChR2-mCherry selectively in Cre^{-} neurons. Single confocal plane showing neighboring ChR2-mCherry⁺ soma (dotted outline) and ChAT⁺ soma at the GP/NB border. Of 158 ChR2-mCherry⁺ neurons surrounding 223 ChAT⁺ neurons, 0 were ChR2-mCherry⁺ChAT⁺ (n=2 mice).

b. Sagittal atlas with the GP/NB border dotted. **c.** *Left*, low magnification view of $ChAT^{i-Cre/+}$ GP following transduction with rAAV DIO-Synaptophysin-mCherry. DAPI (gray), nuclear stain. *Right*, max projection confocal stack (28 μ m) of inset region. Example putative presynaptic punctae indicated by arrowheads.

d. *Left*, low magnification sagittal section from $ChAT^{i-Cre/+}; Rosa26^{lsI-ChR2-EYFP/+}$ mouse. *Right*, high magnification inset of GP showing distribution of neurons (NeuN immunostain) and ChR2-EYFP⁺ processes.

Figure 4.11 (Continued)



record from ChR2⁻ neurons densely surrounded by ChAT⁺ ChR2⁺ fibers. Optogenetic activation evoked inward excitatory post-synaptic currents (EPSCs) at -70 mV (E_{Cl} , the reversal potential for Cl⁻) in a small number of cells (n=2 of 85) (Figure 4.12a) and larger, more prevalent outward IPSCs at 0 mV (n=7 of 85) (Figure 4.10c and Figure 4.12b). EPSCs were unaffected by application of CPP and NBQX, but abolished by nicotinic receptor antagonists (MEC, MLA and DH β E), indicative of ACh release and activation of ionotropic nicotinic receptors (Figure 4.12c-f). IPSCs were blocked by SR95531, but not by CPP, NBQX, MEC, MLA or DH β E, indicating GABA_A receptor activation independent of glutamatergic and nicotinic signaling. IPSCs were blocked by TTX and rescued by 4AP, confirming direct release of GABA by ChAT⁺ cells (Figure 4.10c). We conclude that both ChAT⁺ and ChAT⁻ GP-FC cells are functionally GABAergic, consistent with *Vgat* and *GAD2* expression in both cell types. Additionally, ChAT⁺ GP-FC cells release ACh, consistent with ChAT expression.

Understanding how ChAT⁻ and ChAT⁺ GP-FC cells modulate FC by release of GABA and GABA/ACh requires identifying the post-synaptic cell types. GABA and ACh can signal through ionotropic and metabotropic receptors, both of which can be expressed pre and post-synaptically. Cortical microcircuits are organized by layer^{7,32} and include two major classes of neurons: Pyramidal neurons that excite local and distant targets through the release of glutamate and a diverse set of interneurons that inhibit other cortical neurons through the release of GABA^{8,33}. We focused on post-synaptic ionotropic receptor signaling as it allows unambiguous identification of monosynaptic connections. We introduced ChR2 into ChAT⁺ and ChAT⁻ GP-FC cells by rAAV injection in

Figure 4.12. ChR2-mediated activation of $ChAT^{i-Cre}$ axons following rAAV transduction or with a Cre-activated allele evokes ACh and GABA mediated currents.

a,b. Following rAAV transduction in $ChAT^{i-Cre/+}$ mice, ChR2 activation of local $ChAT^{i-Cre}$ axon collaterals results in rare nicotinic EPSCs but prevalent GABAergic IPSCs onto ChR2⁻ GP/NB neurons (EPSC=2 of 85 cells; IPSC=7 of 85 cells).

a. Light-evoked EPSC from an example ChR2⁻ GP/NB cell voltage-clamped at -70 mV (*top*) was insensitive to glutamate receptor block with NBQX and CPP (*middle*), but abolished by bath application of MEC, MLA & DH β E (*bottom*), suggesting the EPSC resulted from ACh release and nicotinic receptor activation.

b. Summary of peaks from nicotinic EPSCs and GABAergic IPSCs evoked from $ChAT^{i-Cre}$ axons onto ChR2⁻ GP/NB cells.

c. *Left*, low magnification image of sagittal section from a $ChAT^{i-Cre/+}; Rosa26^{lsI-ChR2-EYFP/+}$ mouse. *Right*, high magnification of inset from frontal cortex showing distribution of neurons (NeuN immunostain) and ChR2-EYFP, expressed in axons from basal forebrain and in local cortical interneurons.

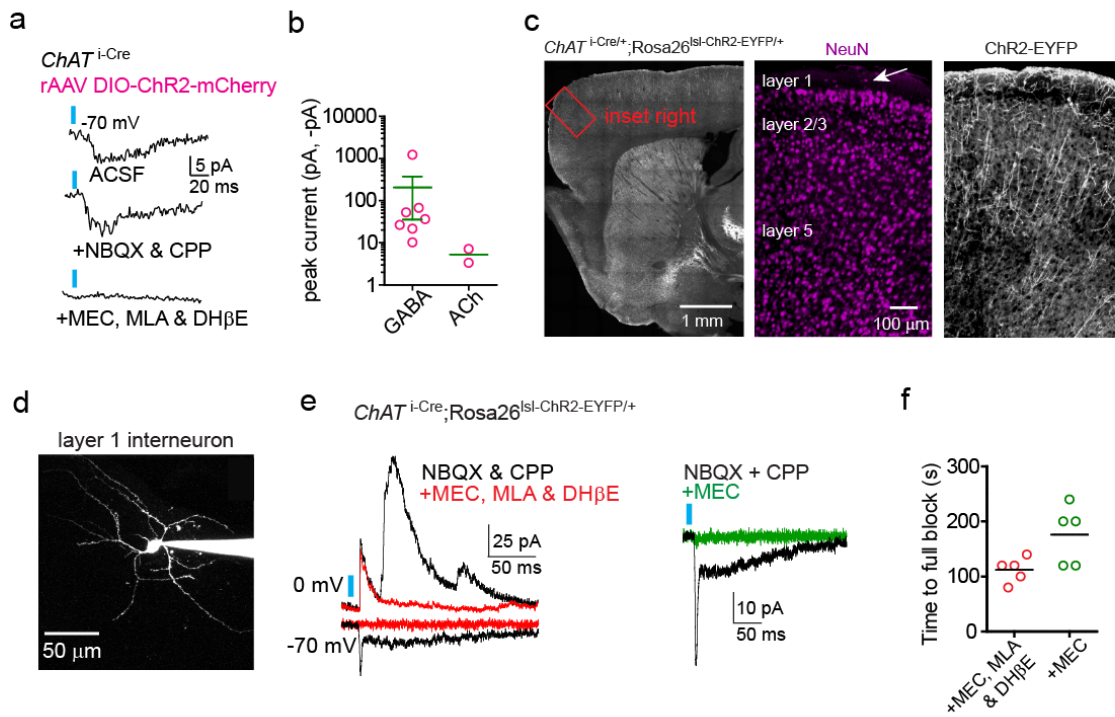
d. Maximum intensity 2-photon projection of a layer 1 interneuron following whole-cell recording.

e. *Left*, light-evoked current responses from two layer 1 interneurons held at indicated potentials to optogenetic activation in a $ChAT^{i-Cre/+}; Rosa26^{lsI-ChR2-EYFP/+}$ mouse in baseline conditions (black, NBQX & CPP) and after bath application of nicotinic receptor antagonist cocktail (red, MEC, MLA & DH β E). *Right*, nicotinic EPSCs are blocked by bath application of the non-selective blocker MEC alone (green).

Figure 4.12 (Continued)

f. Time until full block of light-evoked nicotinic EPSCs following bath application of either nicotinic receptor antagonist cocktail (MEC, MLA & DH β E)(n=5 cells) or MEC alone (n=5 cells). Inter-stimulus interval = 20 s.

Figure 4.12 (Continued)



the GP of *ChAT*^{i-Cre};*GAD67*^{GFP/+} mice and targeted whole-cell voltage-clamp recordings to FC somata within 150 μm of *ChR2*⁺ axons. We light-activated axons and screened for direct (present in TTX/4AP or short-latency) nicotinic EPSCs and GABAergic IPSCs at -70 and 0 mV. Following recording, we determined the layer (1, 2/3, 5 and 6) and type (pyramidal neuron or interneuron) of cells, based on location, *GAD67*^{GFP} expression and dendritic morphology ([Figure 4.10d](#)).

Activation of ChAT- axons evoked reliable IPSCs onto interneurons in layers 2/3, 5, and 6, as well as a pyramids in layers 5 and 2/3. Activation of ChAT+ axons produced less reliable ionotropic currents. We detected IPSCs in a small number of interneurons in layers 1, 2/3 and 6 and EPSCs in interneurons in layers 1 and 6 ([Figure 4.10e](#) and [Figure 4.13a,b](#)). These results suggest ChAT- GP-FC cells inhibit interneurons and pyramids across cortical layers, while ChAT+ GP-FC cells can activate and inhibit cortical interneurons via release of GABA and ACh.

Understanding how co-released neurotransmitters affect target cells necessitates understanding if the transmitters are packaged in the same synaptic vesicles and present in the same pre-synaptic terminals. To determine the anatomy of co-release, we labeled ChAT+ GP-FC axonal terminals by injecting an rAAV carrying a Cre-dependent Synaptophysin-GFP into the GP of *ChAT*^{i-Cre} mice (n=2) and assayed co-localization with a variety of pre and post-synaptic markers in FC using array tomography and automated detection ([Figure 4.10h-k](#) and [Figure 4.13c-d](#)). Maximum projections through reconstructed stacks (n=8 stacks, with n=26-31 70 nm slices each; total volume = $7.6 \times 10^5 \mu\text{m}^3$) revealed a GFP signal that resembled “pearls

Figure 4.13. Synaptic connectivity and array tomography marker co-localization analysis of GP-FC cells in FC.

a. Peak currents induced by Chr2 activation of ChAT+ or ChAT- GP-FC cells. Post-synaptic cells are grouped across layers as pyramids or interneurons. *Left*, GABAergic IPSCs reported with either TTX/4AP in the bath or following wash in are plotted with dotted data. IPSCs recorded in baseline conditions (ChAT-, NBQX & CPP; ChAT+, ACSF only) and are plotted with undotted data. Each cell is represented once. (ChAT-, n=5 pyramids, n=15 interneurons; ChAT+, n=3 interneurons). *Right*, nicotinic EPSCs recorded in ACSF, present after bath application of CPP and NBQX and fully blocked by nicotinic receptor antagonists (MEC, MLA, DH β E)(n=2 interneurons).

b. Onset latencies for IPSCs and EPSCs induced by Chr2 activation of ChAT+ or ChAT- GP-FC cells under baseline conditions only (“ACSF”) or in the presence of TTX/4AP (“TTX/4AP”). “Baseline_{TTX/4AP}” refers to the subset of cells with IPSCs recorded under both baseline conditions and recovered following wash in of TTX/4AP (n=5; same data as [Figure 4.10c](#)). Onset latencies of ChAT- IPSCs were longer in TTX/4AP (n=14) than ACSF (n=11). Asterisk, P<0.05 (Mann-Whitney). Bars denote mean \pm s.e.m.

c-d. Array tomography based co-localization analysis of ChAT+ axonal terminals in FC.

c. *Left*, 300 μ m sagittal slab from a *ChAT*^{i-Cre/+} mouse injected with 300 nl of rAAV DIO-Synaptophysin-GFP in GP. *Right*, box indicates area of FC prepared for array tomography.

Figure 4.13 (Continued)

d. Automated detection of GFP⁺ pearls and synaptic markers. Left, Maximum projection of GFP following computational detection of string-associated “pearls” (in red). *Right*, a single 70 nm plane showing diffraction-limited immunohistochemical puncta for PSD-95 and computationally detected point-sources (in red).

e-g. GFP⁺ pearls are putative GABAergic pre-synaptic terminals.

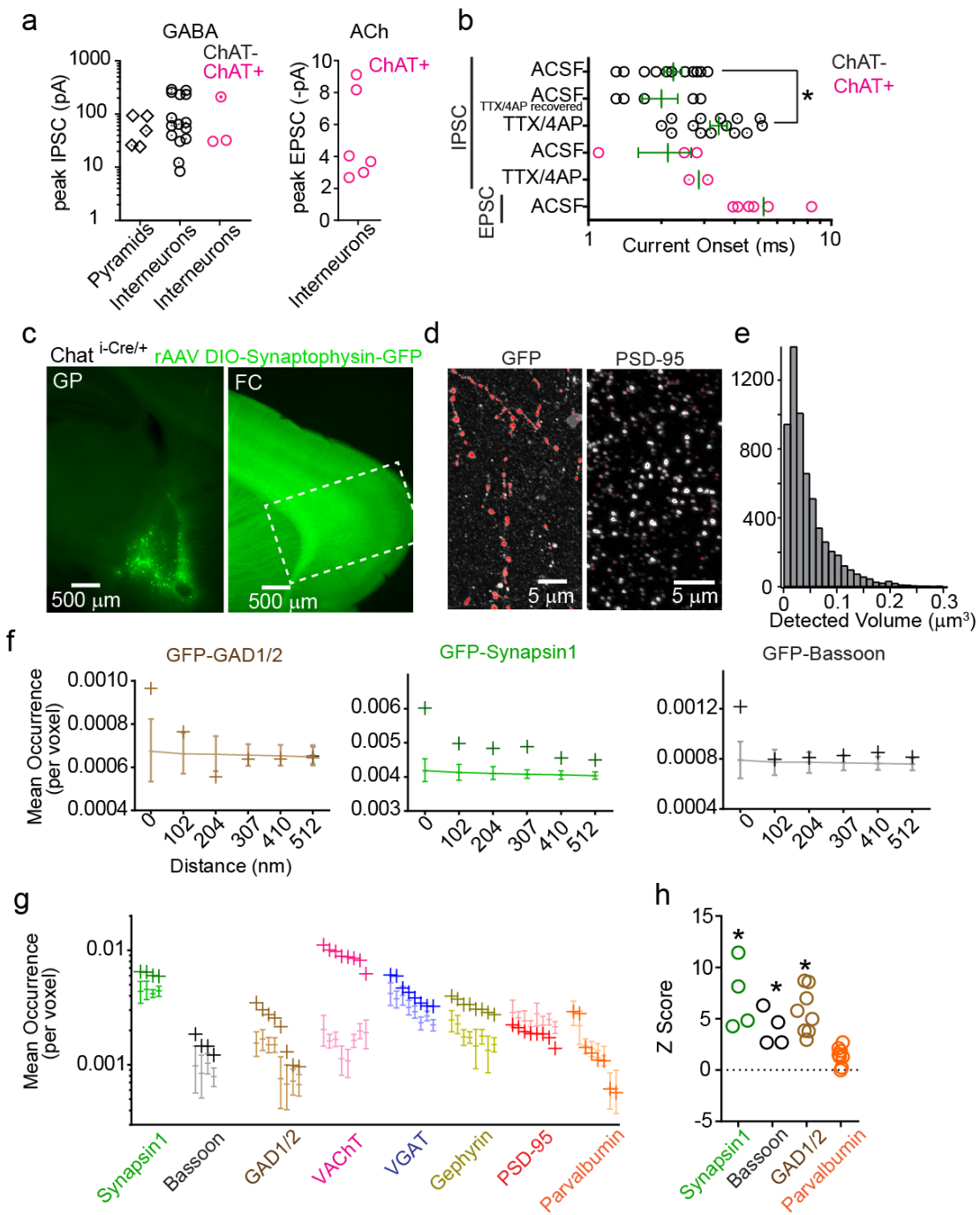
e. Volumes for all detected GFP⁺ pearls (n=6,071 pearls from n=2 mice; n=4 layers 1 & 2/3 stacks and n=4 layer 5 stacks).

f. Mean occurrence by distance plots for GFP⁺ pearls association with GAD1/2, synapsin1, bassoon and parvalbumin (PV) from a single stack. Crosses indicate real data means, while lines denote mean values following 1000 rounds of marker randomization. Error bars denote 99% confidence intervals.

g. Z score summary (n=8 stacks) quantifying the difference in 0 distance occurrences between GFP⁺ pearls and individual synaptic markers shown in **f.** for the real data and following 10 rounds of randomization of GFP⁺ pearls. Positive Z scores indicate higher occurrence in the real data. Asterisk, P<0.001 for all stacks.

h. Mean occurrences at 0 distance for all markers and all stacks. Real and randomized data are indicated as in **f.**

Figure 4.13 (Continued)



on a string,” consistent with GFP enriched in synaptic vesicles (Figure 4.10f). Detected GFP⁺ pearls had volumes consistent with pre-synaptic terminals in the central brain^{9,34} and co-localized with Synapsin1, Bassoon and GAD1/2 (Figure 4.13e-h), suggesting “pearls” correspond to functional pre-synaptic terminals capable of synthesizing GABA. Pearls co-localized with Gephyrin but not PSD-95, indicating that ChAT+ “pearls” oppose inhibitory but not excitatory post-synaptic densities (Figure 4.10g-i).

Consistent with the co-release observed physiologically, pearls co-localized with the vesicular transporters for both GABA and ACh (Figure 4.10g-i). While the majority of pearls contained at least one of the vesicular transporters (n= 4274 of 6071), we observed all combinations: VAcHT alone (n=2030), VGAT alone (n=407) and both VGAT and VAcHT (n=1837). To determine whether VGAT and VAcHT are localized to the same vesicle pool, we measured their centroid distances in pearls containing both vesicular transporters (Figure 4.10j). On average, VGAT and VAcHT puncta are 318(±0.39) nm apart. This separation suggests ChAT+ GP-FC cells achieve GABA and ACh co-release through distinct vesicular pools which can be located in the same or neighboring pre-synaptic terminals (Figure 4.10k). Consistent with the GABA release described here, ChAT⁺ pre-synaptic terminals in cortex contain GABA^{10,35} and appear inhibitory at the ultra-structural level^{11,36}.

Our results suggest GP-FC signaling in FC is complex: ChAT- axons release GABA onto pyramidal neurons and interneurons, whereas ChAT+ axons release ACh and GABA exclusively onto cortical interneurons, likely via distinct vesicular pools, with the net effect of disinhibiting cortex. Additional mechanisms by which ChAT+ and ChAT-

neurons may affect FC include metabotropic receptor signaling, pre-synaptic modulation of transmitter release, or by ionotropic signaling in distal dendrites of other cell types, all of which would be missed by our anatomical and connectivity screen.

To determine if the GP-FC projection is a bonafide BG output, we tested whether GP-FC cells receive synaptic inputs typically associated with the GP: excitatory glutamatergic input from the subthalamic nucleus (STN) and inhibitory GABAergic input from SPNs of the dorsal striatum. To determine whether STN axons arborize in the regions of the GP containing GP-FC cells, we cut parasagittal acute slices that preserve STN-GP connectivity^{12,13,37} and labeled the STN using biocytin. Labeled projections were present in the ventral and posterior GP, the region containing GP-FC cells (Figure 4.14a). To test whether STN neurons make synapses on retro bead labeled GP-FC cells, we combined whole-cell voltage-clamp recordings with electrical stimulation of the STN-GP axon tract and pharmacologically isolated ionotropic glutamate receptors (Figure 4.14b,c). ChAT+ and ChAT- cells were distinguished by reporter expression in *ChAT*^{i-Cre/+} mice or by soma size and cell-attached recordings of spontaneous firing rate in non-reporter mice. Electrical stimulation evoked NBQX-sensitive inward currents at -70 mV and CPP-sensitive outward currents at +40 mV, indicating activation of AMPA and NMDA receptors respectively (Figure 4.14d). Current onset latencies were short (ChAT+: 2.3 ± 0.3 ms, n=6 cells; ChAT-: 3.08 ± 0.3 ms, n= 4 cells)(Figure 4.14e) consistent with direct connectivity of STN projection neurons onto GP-FC cells.

Figure 4.14. GP-FC cells receive glutamatergic synapses from STN and GABAergic synapses from dorsal striatal iSPNs and dSPNs with different presynaptic properties.

a. *Left*, low magnification view of para-sagittal slice showing the GP following biocytin labeling of the STN and avidin-HRP/DAB visualization of STN projections. *Right*, high magnification view of inset showing DAB-labeled projections in the GP and around the GP/NB border.

b. Schematic of experimental strategy to electrically stimulate STN projections to GP. A bipolar electrode was placed at the anterior border of STN and GP-FC cells were targeted for whole-cell voltage-clamp recording.

c. Acute parasagittal slice showing location of the bipolar electrode and recording pipette (red asterisk).

d,e. Electrically-evoked glutamatergic currents in GP-FC cells following stimulation of STN-GP axon tract.

d. *Left*, example NBQX-sensitive AMPAR ($V_{\text{hold}} = -70$ mV) then CPP-sensitive NMDAR ($V_{\text{hold}} = +40$ mV) currents evoked in GP-FC cells under baseline conditions (SR95331, scopolamine, CGP55845). *Right*, summary of AMPAR and NMDAR peak currents in ChAT+ (n=6) and ChAT- (n=4) GP-FC cells.

e. Onset latencies of glutamatergic currents. Bars denote mean \pm s.e.m.

f,g. SPNs from dorsal striatum arborize axons in and around the GP/NB border but not in the basal forebrain.

Figure 4.14 (Continued)

f. *Left*, sagittal section from a $VGAT^{i-Cre/+}$ mouse injected with rAAV DIO-mCherry into dorsal striatum. *Right*, higher magnification of inset. Axons from SPNs arborize in the GP proper and GP/NB border regions (areas 1 and 2) but not in the more ventral region of the basal forebrain (area 3, NB proper/Substantia Innominata).

g. *Left*, maximum projection confocal stacks ($z = 28-42 \mu\text{m}$) from the inset regions in **f.** *Right*, binary axonal quantification from the regions indicated. SPN axon density is sharply reduced in NB proper/Substantia Innominata.

h. Synaptic connectivity screen for dorsal striatal SPN IPSCs onto $ChAT^+$ neurons of the GP and basal forebrain. $ChAT-GFP$ mice were injected with Cre-Off rAAV DO-ChR2-mCherry in dorsal striatum and whole-cell recordings were targeted to $ChAT^+$ neurons ($n=4$ mice, 23 cells) in combination with optogenetic activation. NBQX and CPP were included in the bath to block glutamatergic transmission. *Left*, sagittal map of recording locations of SPNs with detected IPSCs (blue) and no detected IPSCs (red). *Right*, peak and onset latencies for detected IPSCs. Green lines denote means. IPSCs onto $ChAT^+$ neurons of the GP were detected before recordings were targeted to more ventral areas.

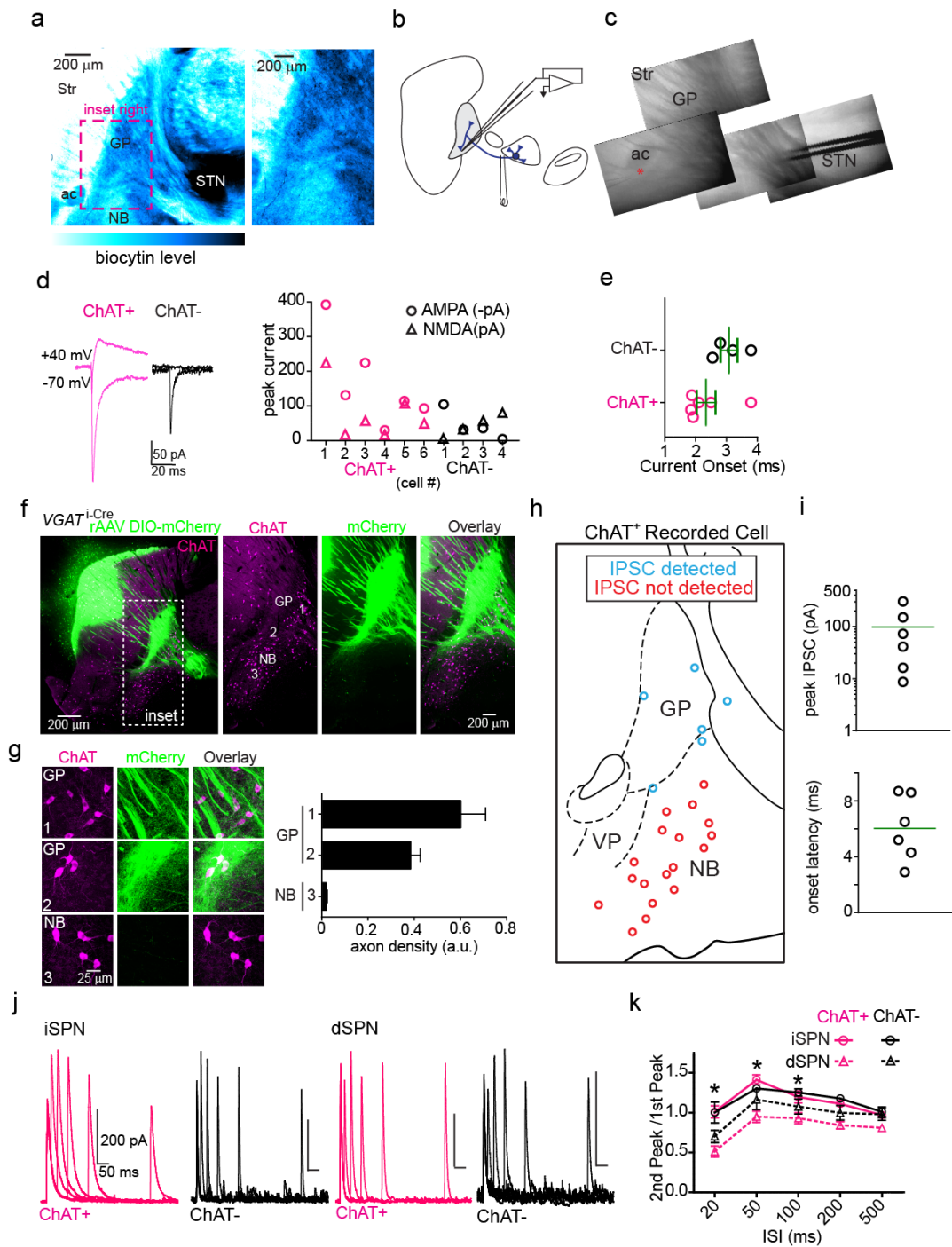
j,k. Paired pulse optogenetic activation of iSPNs ($Adora2a-Cre;Rosa26^{Isl-CHR2-EYFP/+}$) and dSPNs ($Drd1a-Cre;Rosa26^{Isl-CHR2-EYFP/+}$) in dorsal striatum reveals differences in short-term synaptic plasticity properties in GP-FC cells.

j. Examples of optogenetically evoked paired pulse IPSCs (interstimulus interval = 20, 50, 100, 200, and 500 ms) from iSPNs (*left*) and dSPNs (*right*) in GP-FC cells.

Figure 4.14 (Continued)

k. Mean 2nd/1st peak IPSC ratios (iSPN: n= 13 ChAT+, n=9 ChAT-; dSPN: n=9 ChAT+, n=8 ChAT-). Asterisk, $P < 0.05$ iSPNs vs dSPNs (ChAT+ and ChAT- grouped together)(Mann-Whitney); Error bars denote s.e.m.

Figure 4.14 (Continued)



SPNs of the dorsal striatum receive glutamatergic input from motor, sensory and associative areas of cortex^{14-16,38} and convey this information to the rest of the BG through the direct and indirect pathways^{2,17}. iSPNs and dSPNs provide the only projections out of the striatum and both cell types arborize in the GP^{18,39}. To assess whether iSPN and dSPN axons ramify in areas of the GP containing GP-FC cells, we injected rAAVs into the dorsal striatum of *Drd2-Cre* mice to selectively label projections of Cre⁺ iSPNs and Cre⁻ dSPNs followed by ChAT immunostaining (Figure 4.15a) or whole-brain reconstructions (B.Movie 2). iSPN and dSPN axons target distinct but overlapping areas of the GP, including the GP/NB border containing ChAT⁺ cells, but not more ventrally located ChAT⁺ cells of the basal forebrain (Figure 4.14f-i). Unexpectedly, dSPN axons arborize extensively in this region, suggesting that iSPNs and dSPNs from dorsal striatum are positioned to innervate GP-FC cells.

To determine whether iSPNs and dSPNs axons synapse onto GP-FC cells, we targeted retro bead labeled GP-FC cells for whole-cell voltage-clamp recording in *Adora2a-Cre; Rosa26^{lsl-ChR2-EYFP/+}* or *Drd1a-Cre; Rosa26^{lsl-ChR2-EYFP/+}* mice where ChR2 is expressed in iSPNs or dSPNs, respectively (Figure 4.15b). Ionotropic GABA receptor currents were pharmacologically isolated and measured in voltage-clamp at 0 mV as outward currents. Light-activation of iSPN or dSPN axons surrounding the recorded cell evoked SR95531-sensitive outward currents in nearly all GP-FC cells (ChAT⁺: 20 of 22; ChAT⁻: 19 of 20), indicating high GABA_A receptor mediated connectivity.

Figure 4.15. The GP-FC projection is a basal ganglia (BG) output sensitive to anti-psychotic drugs.

a. *Top left*, sagittal section from a *Drd2*-Cre mouse injected with rAAVs DIO-EGFP (Cre-On, green) and FAS-TdTomato (Cre-Off, red) into dorsal striatum. *inset 1*, higher magnification view of the GP, illustrating the axonal innervation zones of iSPNs (green) and dSPNs (red) in relation to ChAT⁺ cells (magenta). *Insets 2 and 3* show a higher magnification view of the ventral and posterior ChAT⁺ GP-FC clusters, surrounded by iSPN and dSPN axons.

b. *Left*, sagittal sections from an *Adora2a*-Cre;*Rosa26*^{Isl-ChR2-EYFP/+} mouse (*top*) or *Drd1a*-Cre; *Rosa26*^{Isl-ChR2-EYFP/+} mouse (*bottom*) where ChR2-EYFP is expressed in either iSPNs or dSPNs, respectively. *Middle*, schematic of experimental strategy to study connectivity and properties of iSPN or dSPN synapses onto GP-FC cells using whole-cell voltage-clamp recording. First, a standardized light pulse (1 ms; 1.3 mW·mm⁻²) was delivered over the recorded cell. Second, the objective was moved into dorsal striatum and light power adjusted (0.5–1 ms; 0.06–4.4 mW·mm⁻²) for ~200 pA first-peak paired-pulse and pharmacology experiments. *Top right*, optogenetic activation of iSPN (*top*) or dSPN (*bottom*) axons evoked outward currents from ChAT⁺ and ChAT⁻ cells held at 0 mV under baseline conditions (black; NBQX, CPP, scopolamine, CGP55845 & AM251) which were blocked by bath application of SR95531 (gray).

c. Peak IPSCs evoked from iSPN or dSPN optogenetic activation over the recorded GP-FC cell. iSPN activation evokes larger peak IPSCs onto ChAT⁻ (n=19) vs. ChAT⁺ (n=20) cells, while dSPN evoked comparable IPSCs onto ChAT⁻ (n=11) vs. ChAT⁺ (n=12) cells. ChAT⁻

Figure 4.15 (Continued)

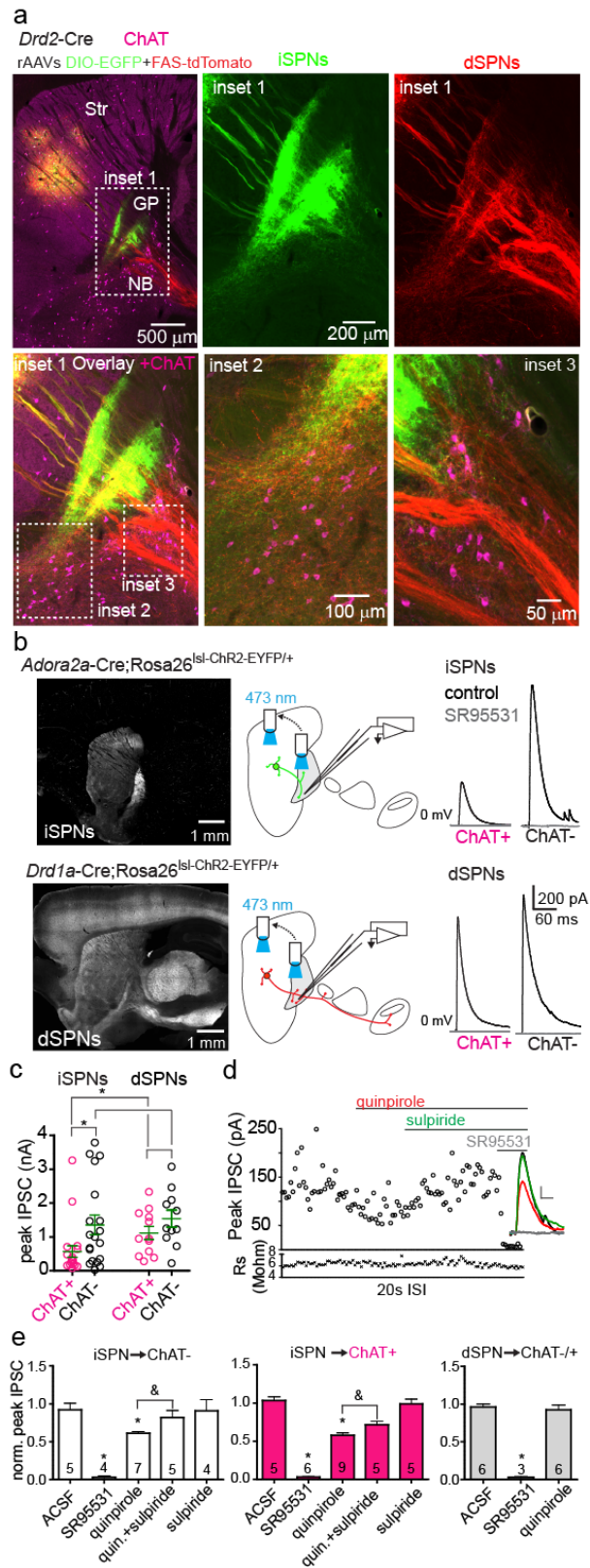
cells have similar peak IPSCs from dSPN and iSPN activation, while peak IPSCs from dSPN activation is larger onto ChAT+ cells than iSPN activation. Asterisk, $P < 0.05$ (Mann-Whitney). Bars denote mean \pm s.e.m.

d,e. iSPN but not dSPN synaptic currents are decreased through dopamine receptor 2 activation and reversed by an anti-psychotic.

d. Example iSPN peak IPSCs (20 s inter-stimulus interval) onto a ChAT- GP-FC cell under baseline ACSF conditions (NBQX, CPP, scopolamine, CGP55845 & AM251) and following bath application of quinpirole (gray), sulpiride (green) and SR95331 (red). Series resistance (R_s) is plotted below. *Inset*, average steady state currents for each pharmacological condition (scale bar = 20 pA, 10 ms).

e. Mean IPSCs amplitudes under baseline ACSF conditions and in drug conditions normalized to baseline. Asterisk, $P < 0.05$ vs. ACSF (Mann-Whitney); ampersand, $P < 0.05$ quinpirole vs. quinpirole + sulpiride (Paired t-test on the subset of cells with both conditions, $n=5$). Error bars denote s.e.m.

Figure 4.15 (Continued)



dSPN activation evoked larger peak synaptic currents onto ChAT+ cells than iSPN activation (dSPNs: 1.11 ± 0.19 , iSPNs: 0.57 ± 0.17 nA), consistent with the larger axonal territory of dSPNs at the GP/NB border. Activation of dSPNs and iSPNs evoked similar, strong synaptic currents onto ChAT- cells (dSPNs: 1.54 ± 0.25 , iSPNs: 1.35 ± 0.29 nA)([Figure 4.15c](#)). Synapses onto GP-FC neurons from dSPNs and iSPNs in dorsal striatum also displayed different short-term plasticity as reported by paired-pulse ratios (PPR), showing depression and facilitation, respectively, at short latencies (PPR at 25 ms ISI: dSPNs 0.59 ± 0.05 , iSPNs 1.01 ± 0.06 ; PPR at 50 ms ISI: dSPNs 1.03 ± 0.08 , iSPNs 1.37 ± 0.04 , n=15-23 cells) ([Figure 14.4 j,k](#)). Together these results indicate that GP-FC cells are functionally integrated into BG circuitry through direct, indirect and “hyperdirect” (STN-GP)^{19,40} pathways. Although iSPNs and dSPNs both inhibit GP-FC cells, differences in synaptic strength and short-term plasticity suggest that ongoing activity in each pathway could differentially inhibit the GP-FC projection.

The presence of a GABAergic output to cortex under control of striatal SPNs could be important for understanding the etiology and treatment of motor and psychiatric diseases that affect BG circuitry^{20,41}. One example is schizophrenia, which often presents in late adolescence, a period associated with dynamic developmental changes of inhibitory circuits in prefrontal cortex^{21,42}. Mounting evidence suggests that overactive dopamine signaling in the striatum may play an important part in the disease^{22,43}. A cornerstone of this theory is the mechanism of action of antipsychotic drugs, which relieve hallucinations and delusions by blocking D2rs^{6,23}. Schizophrenics exhibit imbalances in both GABA^{24,44,45} and ACh^{25,46} neurotransmitter systems, as well as

marked changes in morphology and gene expression of cortical interneurons^{26,47,48}.

Since GP-FC cells are present in primates (Figure 4.3), release GABA and ACh onto interneurons in FC (Figure 4.10), and are inhibited by D2r-expressing iSPNs (Figure 4.15), we examined whether D2r signaling affects iSPN synapses onto GP-FC cells.

Light-evoked IPSCs from iSPNs in dorsal striatum were measured in GP-FC neurons under voltage-clamp in brain slices from *Adora2a-Cre;Rosa26^{Isl-ChR2-EYP/+}* mice. Bath-application of the D2r agonist quinpirole reduced the size of light-evoked IPSCs in ChAT+ and ChAT- cells. This reduction was reversed by the antipsychotic sulpiride, which had no effect on IPSCs alone, and was not seen when IPSCs were evoked from D1r expressing dSPNs in *Drd1a-Cre;Rosa26^{Isl-ChR2-EYP/+}* mice (Figure 4.15d,e). These data suggest increased striatal dopamine could disinhibit GP-FC projection via anti-psychotic sensitive D2r signaling in iSPNs.

The circuit function of GP-FC cells suggests a major revision to accepted models of subcortical-cortical feedback circuitry. Within the BG, the direct and indirect pathways are thought to exert opposite effects on cortical activity through bidirectional control of thalamic activity^{4,27}. The GP-FC projection permits the BG to bypass thalamus and directly control cortical states. ChAT- GP-FC cells release GABA predominantly onto layer 5 pyramidal neurons and interneurons across layers, suggesting inhibitory and disinhibitory ionotropic effects on microcircuits. ChAT+ GP-FC disinhibit cortex by releasing both GABA and ACh onto interneurons. Unexpectedly, this co-release appears to occur via non-overlapping pools of synaptic vesicles which are located in the same or neighboring pre-synaptic terminals. Based on co-expression of *Vgat* and *GAD2*, GABA

co-release may be widespread in the basal forebrain cholinergic system and an important feature of subcortical regulation of behavioral state and cortical plasticity. In contrast to their opposing effects on thalamic output, the direct and indirect pathways both inhibit the GP-FC projection. Conversely, the hyperdirect pathway through the STN excites both thalamus via the SNr⁴⁹ and GP-FC neurons directly. This connectivity suggests that as cortical information enters the BG, the activity of each internal BG pathway will recruit the thalamic and cortical outputs differently, imposing distinct feedback effects across cortical areas in order to control behavior.

REFERENCES

1. Yin, H. H. & Knowlton, B. J. The role of the basal ganglia in habit formation. *Nat Rev Neurosci* **7**, 464–476 (2006).
2. Smith, Y., Bevan, M. D., Shink, E. & Bolam, J. P. Microcircuitry of the direct and indirect pathways of the basal ganglia. *Neuroscience* **86**, 353–387 (1998).
3. Kravitz, A. V. *et al.* Regulation of parkinsonian motor behaviours by optogenetic control of basal ganglia circuitry. *Nature* **466**, 622–626 (2010).
4. Freeze, B. S., Kravitz, A. V., Hammack, N., Berke, J. D. & Kreitzer, A. C. Control of Basal Ganglia Output by Direct and Indirect Pathway Projection Neurons. *J Neurosci* **33**, 18531–18539 (2013).
5. Goldberg, J. H., Farries, M. A. & Fee, M. S. Basal ganglia output to the thalamus: still a paradox. *Trends Neurosci* **36**, 695–705 (2013).
6. Seeman, P. Dopamine receptors and the dopamine hypothesis of schizophrenia. *Synapse* **1**, 133–152 (2004).
7. Tohen, M. & Vieta, E. Antipsychotic agents in the treatment of bipolar mania. *Bipolar Disord* **11**, 45–54 (2009).

8. Bloch, M. H. *et al.* A systematic review: antipsychotic augmentation with treatment refractory obsessive-compulsive disorder. *Mol Psychiatry* **11**, 622–632 (2006).
9. Hawrylycz, M. J. *et al.* An anatomically comprehensive atlas of the adult human brain transcriptome. *Nature* **489**, 391–399 (2012).
10. Takada, M., Ng, G. & Hattori, T. Single pallidal neurons project both to the striatum and thalamus in the rat. *Neurosci Lett* **69**, 217–220 (1986).
11. Kita, H. Globus pallidus external segment. *Prog Brain Res* **160**, 111–133 (2007).
12. Chan, C. S., Surmeier, D. J. & Yung, W.-H. Striatal information signaling and integration in globus pallidus: timing matters. *Neurosignals* **14**, 281–289 (2005).
13. Bevan, M. D., Magill, P. J., Hallworth, N. E., Bolam, J. P. & Wilson, C. J. Regulation of the timing and pattern of action potential generation in rat subthalamic neurons in vitro by GABA-A IPSPs. *J Neurophysiol* **87**, 1348–1362 (2002).
14. Saper, C. B. & Chelimsky, T. C. A cytoarchitectonic and histochemical study of nucleus basalis and associated cell groups in the normal human brain. *Neuroscience* **13**, 1023–1037 (1984).
15. Mesulam, M. M., Mufson, E. J., Levey, A. I. & Wainer, B. H. Atlas of cholinergic neurons in the forebrain and upper brainstem of the macaque based on monoclonal choline acetyltransferase immunohistochemistry and acetylcholinesterase histochemistry. *Neuroscience* **12**, 669–686 (1984).
16. McKinney, M., Coyle, J. T. & Hedreen, J. C. Topographic analysis of the innervation of the rat neocortex and hippocampus by the basal forebrain cholinergic system. *J Comp Neurol* **217**, 103–121 (1983).
17. Heimer, L., Van Hoesen, G., Trimble, M. & Zahm, D. *Anatomy of Neuropsychiatry: The New Anatomy of the Basal Forebrain and Its Implications for Neuropsychiatric Illness*. (Academic Press, 2007).
18. Grove, E. A., Domesick, V. B. & Nauta, W. J. Light microscopic evidence of striatal input to intrapallidal neurons of cholinergic cell group Ch4 in the rat: a study employing the anterograde tracer *Phaseolus vulgaris* leucoagglutinin (PHA-L). *Brain Res* **367**, 379–384 (1986).

19. Chang, H. T., Penny, G. R. & Kitai, S. T. Enkephalinergic-cholinergic interaction in the rat globus pallidus: a pre-embedding double-labeling immunocytochemistry study. *Brain Res* **426**, 197–203 (1987).
20. DeLong, M. R. Activity of pallidal neurons during movement. *J Neurophysiol* **34**, 414–427 (1971).
21. Schultz, W. Changes in behavior-related neuronal activity in the striatum during learning. *Trends Neurosci* **26**, 321–328 (2003).
22. Laplane, D. *et al.* Obsessive-compulsive and other behavioural changes with bilateral basal ganglia lesions. A neuropsychological, magnetic resonance imaging and positron tomography study. *Brain* **112 (Pt 3)**, 699–725 (1989).
23. Zaborszky, L. The modular organization of brain systems. Basal forebrain: the last frontier. *Prog Brain Res* **136**, 359–372 (2002).
24. Rye, D. B., Wainer, B. H., Mesulam, M. M., Mufson, E. J. & Saper, C. B. Cortical projections arising from the basal forebrain: a study of cholinergic and noncholinergic components employing combined retrograde tracing and immunohistochemical localization of choline acetyltransferase. *Neuroscience* **13**, 627–643 (1984).
25. Tkatch, T., Baranauskas, G. & Surmeier, D. J. Basal forebrain neurons adjacent to the globus pallidus co-express GABAergic and cholinergic marker mRNAs. *Neuroreport* **9**, 1935–1939 (1998).
26. Kosaka, T., Tauchi, M. & Dahl, J. L. Cholinergic neurons containing GABA-like and/or glutamic acid decarboxylase-like immunoreactivities in various brain regions of the rat. *Exp Brain Res* **70**, 605–617 (1988).
27. Mallet, N. *et al.* Dichotomous Organization of the External Globus Pallidus. *Neuron* **74**, 1075–1086 (2012).
28. Sarter, M. & Bruno, J. P. The neglected constituent of the basal forebrain corticopetal projection system: GABAergic projections. *Eur J Neurosci* **15**, 1867–1873 (2002).
29. Henny, P. & Jones, B. E. Projections from basal forebrain to prefrontal cortex comprise cholinergic, GABAergic and glutamatergic inputs to pyramidal cells or interneurons. *Eur J Neurosci* **27**, 654–670 (2008).

30. Mesulam, M. M., Mufson, E. J., Levey, A. I. & Wainer, B. H. Cholinergic innervation of cortex by the basal forebrain: cytochemistry and cortical connections of the septal area, diagonal band nuclei, nucleus basalis (substantia innominata), and hypothalamus in the rhesus monkey. *J Comp Neurol* **214**, 170–197 (1983).
31. Saunders, A., Johnson, C. A. & Sabatini, B. L. Novel recombinant adeno-associated viruses for Cre activated and inactivated transgene expression in neurons. *Front Neural Circuits* **6**, 47 (2012).
32. Lefort, S., Tomm, C., Floyd Sarria, J.-C. & Petersen, C. C. H. The excitatory neuronal network of the C2 barrel column in mouse primary somatosensory cortex. *Neuron* **61**, 301–316 (2009).
33. Markram, H. *et al.* Interneurons of the neocortical inhibitory system. *Nat Rev Neurosci* **5**, 793–807 (2004).
34. Shepherd, G. M. & Harris, K. M. Three-dimensional structure and composition of CA3→CA1 axons in rat hippocampal slices: implications for presynaptic connectivity and compartmentalization. *J Neurosci* **18**, 8300–8310 (1998).
35. Beaulieu, C. & Somogyi, P. Enrichment of cholinergic synaptic terminals on GABAergic neurons and coexistence of immunoreactive GABA and choline acetyltransferase in the same synaptic terminals in the striate cortex of the cat. *J Comp Neurol* **304**, 666–680 (1991).
36. Houser, C. R. Cholinergic synapses in the central nervous system: studies of the immunocytochemical localization of choline acetyltransferase. *J Electron Microscop Tech* **15**, 2–19 (1990).
37. (null), Ben-Ari, Y. & Hammond, C. Preservation of the direct and indirect pathways in an in vitro preparation of the mouse basal ganglia. *Neuroscience* **140**, 77–86 (2006).
38. Pan, W. X., Mao, T. & Dudman, J. T. Inputs to the Dorsal Striatum of the Mouse Reflect the Parallel Circuit Architecture of the Forebrain. *Front Neuroanat* **4**, (2010).
39. Chang, H. T., Wilson, C. J. & Kitai, S. T. Single neostriatal efferent axons in the globus pallidus: a light and electron microscopic study. *Science* **213**, 915–918 (1981).

40. Nambu, A., Tokuno, H. & Takada, M. Functional significance of the cortico-subthalamo-pallidal 'hyperdirect' pathway. *Neurosci Res* **43**, 111–117 (2002).
41. Albin, R. L., Young, A. B. & Penney, J. B. The functional anatomy of basal ganglia disorders. *Trends Neurosci* **12**, 366–375 (1989).
42. Insel, T. R. Rethinking schizophrenia. *Nature* **468**, 187–193 (2010).
43. Simpson, E. H., Kellendonk, C. & Kandel, E. A Possible Role for the Striatum in the Pathogenesis of the Cognitive Symptoms of Schizophrenia. *Neuron* **65**, 585–596 (2010).
44. Blum, B. P. & Mann, J. J. The GABAergic system in schizophrenia. *Int. J. Neuropsychopharma* **5**, 159–179 (2002).
45. Hashimoto, T. *et al.* Alterations in GABA-related transcriptome in the dorsolateral prefrontal cortex of subjects with schizophrenia. *Mol Psychiatry* **13**, 147–161 (2008).
46. Scarr, E., Gibbons, A. S., Neo, J., Udawela, M. & Dean, B. Cholinergic connectivity: it's implications for psychiatric disorders. *Front Cell Neurosci* **7**, 55 (2013).
47. Lewis, D. A., Hashimoto, T. & Volk, D. W. Cortical inhibitory neurons and schizophrenia. *Nat Rev Neurosci* **6**, 312–324 (2005).
48. Lewis, D. A., Curley, A. A., Glausier, J. R. & Volk, D. W. Cortical parvalbumin interneurons and cognitive dysfunction in schizophrenia. *Trends Neurosci* **35**, 57–67 (2012).
49. Ammari, R., Lopez, C., Bioulac, B., Garcia, L. & Hammond, C. Subthalamic nucleus evokes similar long lasting glutamatergic excitations in pallidal, entopeduncular and nigral neurons in the basal ganglia slice. *Neuroscience* **166**, 808–818 (2010).

METHODS

Mice. Bacterial artificial chromosome (BAC) transgenic mice expressing EGFP under control of the dopamine 2 receptor locus (*Drd2*-EGFP) were used to define the

anatomical border of the globus pallidus externus (GP) and ventral pallidum (VP) through the expression of EGFP in striatal iSPNs (GENSAT, founder line S118). Cre recombinase was targeted to specific cell types of the basal ganglia using knock-in or BAC transgenic mice to drive Cre expression under gene-specific regulatory elements. Cre knock-in mice for *choline acetyltransferase (ChAT)*¹ and *Slc32a1* (vesicular GABA transporter or *Vgat*)² were generously provided by Brad Lowell (Beth Israel Deaconess Medical Center) and are available from the Jackson Labs (*ChAT*^{i-Cre}, stock #006410; *Vgat*^{i-Cre}, stock #016962). *GAD2*^{i-Cre} were purchased from Jackson Labs (stock #010802)³. All knock-in mice link Cre expression to the gene of interest using an internal ribosome entry site. Targeting Cre expression in dSPNs was achieved with BAC transgenic mice expressing Cre under control of the dopamine receptor 1 (*Drd1a*) or in iSPNs with Cre under control of the adenosine 2A receptor (*Adora2a*) or dopamine receptor 2 (*Drd2*) regulatory elements and obtained from GENSAT (*Drd1a*-Cre, founder EY262, stock #017264-UCD; *Adora2a*-Cre, founder KG139, stock # 031168-UCD; *Drd2*-Cre, founder ER43, stock #017268-UCD). The ChAT-GFP BAC transgenic line used to identify ChAT⁺ neurons was purchased from Jackson Labs (#007902)⁴. To visualize the full processes of Cre expressing cells, Cre mice were bred to Cre-dependent TdTomato reporter allele⁵ (Ai14; Jackson Labs, stock # 007914; referred to as Rosa26^{lsl-tdTomato}). To visualize the somata of Cre expressing cells, the Cre-dependent ZsGreen reporter allele was used (Ai6; Jackson Labs, stock # 007906; referred to Rosa26^{lsl-zsGreen}). To target channelrhodopsin-2 (ChR2) to all Cre expressing cells, Cre driver mice were bred to a Cre-dependent **Chr2(H134R)-EYFP** transgene⁶ (Ai32; Jackson Labs, stock #012569;

referred to as Rosa26^{Isl-ChR2-EYFP}). Conditional knockout of *Slc32a1* (*Vgat*) was achieved by introgressing a *Slc32a* allele⁷ where the second exon is flanked by loxp sites (Jackson Labs, stock# 012897; referred to as *Vgat*^{fl/fl}) into *ChAT*^{i-Cre};Rosa26^{Isl-ChR2-EYFP} mice. In experiments designed to identify cortical cells neighboring ChR2⁺ ChAT⁺ or ChAT⁻ GP-FC axons as pyramids or interneurons, *ChAT*^{i-Cre} mice also carried a GAD67^{GFP} knock-in allele⁸ to highlight a subset of cortical interneurons synthesizing GABA. Wild type mice refer to C57BL/6 obtained from Charles River. Transgenic mice were of a mixed genetic background. All experimental manipulations were performed in accordance with protocols approved by the Harvard Standing Committee on Animal Care following guidelines described in the US National Institutes of Health *Guide for the Care and Use of Laboratory Animals*.

Virus Preparation. Cre-On or Cre-Off conditional expression was achieved using recombinant adeno-associated virus (rAAV) carry transgenic cassettes whose transcription was activated or inactivated by Cre⁹. Cre-On conditional expression of channelrhodopsin-2 (ChR2-mCherry, H134R variant), EGFP, mCherry, or Synaptophysin-mCherry was achieved by using a double-floxed inverted open reading frame (DIO). Cre-Off conditional expression of ChR2-mCherry was achieved by starting the open reading frame in the non-inverted orientation with respect to the promoter (DO). To achieve simultaneous Cre-On EGFP and Cre-Off tdTomato labeling, DIO-EGFP was mixed 1:1 with FAS-tdTomato, an alternative Cre-Off rAAV backbone that achieves Cre-Off expression through excision of the open reading frame using alternative loxp sites⁹. DIO, DO, and FAS rAAVs all use the EF1a promoter and were packaged in serotype 8 by a commercial

vector core facility (University of North Carolina). All rAAVs were stored in undiluted aliquots at a concentration $>10^{12}$ genomic copies per ml at -80°C until intracranial injection.

Stereotaxic intracranial injections. Male and female mice (postnatal day 20–120) were anesthetized with isoflurane and placed in a small animal stereotaxic frame (David Kopf Instruments). Under aseptic conditions, the skull was exposed and a small hole was drilled. For rAAVs injections, 200-350 nl total volume was delivered bilaterally into the ventral GP/dorsal NB or 500 nl into dorsal striatum through a pulled glass pipette at a rate of $200\text{ nl}\cdot\text{min}^{-1}$ using a Microinject system (World Precision Instruments). GP injection coordinates were 0.7 mm posterior from Bregma, 2.0 mm lateral and 3.8 mm below the pia. Dorsal striatum injection coordinates were 0.9 mm anterior from Bregma, 2.2 mm lateral and 2.5 mm below the pia. After surgical procedures, mice received flunixin for analgesia and were returned to their home cage for >21 days to allow for maximal gene expression. To identify GP neurons that project to frontal cortex, 200 nl of fluorescent retro beads (Red-1X or Green, Lumafluor) were injected into frontal (anterior to striatum) cortical areas including secondary motor (M2), primary motor (M1), primary somatosensory (S1) and dorsal and ventral agranular insular (AID and AIV) cortices. Frontal cortex injection coordinates were 1.9 mm anterior from Bregma, 1.8 mm lateral and 2 mm below the pia. Following surgery, mice received flunixin and were returned to their home cage for 3-9 days before experimentation. Stereotaxic coordinates were adjusted slightly by age.

Fixed Tissue Preparation and Imaging. Mice were deeply anesthetized with isoflurane and transcardially perfused with 4% paraformaldehyde (PFA) in 0.1 M sodium phosphate buffer (1x PBS). Brains were post-fixed for 1–3 days, washed in 1x PBS and sectioned (40 μm) coronally, sagittally, or horizontally using a Vibratome (Leica). Slices were then immunostained (see **Immunohistochemistry**) or mounted on slides (Super Frost). After drying, slices were coverslipped with ProLong antifade mounting media containing DAPI (Molecular Probes) and imaged with an Olympus VS110 slide scanning microscope using the 10x objective. Fluorescent proteins introduced through rAAVs or transgenic alleles were never immunoenhanced, except in 3D brain reconstructions (see **3D brain reconstruction and analysis**). Confocal images (1-2 μm optical sections) were acquired with an Olympus FV1000 laser scanning confocal microscope (Harvard Neurobiology Imaging Facility) through a 63x objective.

Immunohistochemistry. Immunohistochemistry conditions were the same for both mouse and macaque sections. For ChAT immunohistochemistry, slices were incubated in a 1x PBS blocking solution containing 5% normal horse serum and 0.3% Triton X-100 for 1 hour at room temperature. Slices were then incubated overnight at 4^oC in the same solution containing anti-choline acetyltransferase antibody (1:100, Millipore AB144P). The next morning, sections were washed three times for five minutes in 1x PBS for and then incubated for 1 hour at room temperature in the blocking solution containing donkey anti-goat Alexa 647 or Alexa 488 (1:500, Molecular Probes). For macaque sections, streptavidin conjugated to Alexa 350 or Alexa 488 (1:1000, Molecular Probes)

was also included in the secondary reaction. The same protocol was used for NeuN (1:100, Millipore MAB377) and Parvalbumin (1:7500, Swant PV235) immunostaining with anti-mouse Alexa 647 secondary antibodies (1:500, Molecular Probes).

Immunostained mouse sections were mounted and imaged as described above.

Immunostained *macaque* sections were mounted as described below.

Retrograde tracing in a *Rhesus macaque*. A 10 year-old male *rhesus macaque* was prepared for surgery under aseptic conditions. Anesthesia was initiated with ketamine (15 mg/kg) and valium (1 mg/kg) and the macaque was given an intravenous catheter and intubated. Isoflurane (1-2% in oxygen) was used to maintain anesthesia. Bilateral circular craniotomies were made over the frontal cortex, exposing the principal and arcuate gyri. Tracer injections were targeted to cortical areas that receive projections from the “Ch4id” and “Ch4iv” cell groups¹⁰. Specifically, tracers were injected along the principal and arcuate gyri (corresponding to the area between Mesulam et al. cases 23, 26 and 6) as well as the ventral orbital frontal cortex (Mesulam case 19) using a micromanipulator to guide a 10 µl Hamilton syringe. In the right hemisphere, Red 1X retro beads (Lumafluor) were injected at 16 dorsal locations and 4 ventral locations. In the left hemisphere, biotinylated dextran amine (BDA, 10% in sterile saline) was injected at 12 dorsal locations and 2 ventral locations. At each site, 0.5 µl of tracer was injected at 2 depths, 1 and 2 mm below the cortical surface. After injection, the skull fragments were replaced and the macaque was allowed to recover on a water heated pad under constant observation. After a 21 day survival period, the macaque was killed with a barbiturate overdose (>50 mg/kg, to effect) and perfused through the heart with normal

saline followed by 4% formaldehyde in 1X PBS, pH 7.4. The brain was removed from the skull and post-fixed for 24 hours in the same fixative solution. Following cryoprotection for 3 days in 30% sucrose solution, the hemispheres were separated, blocked and cut in 40 μm coronal sections using a freezing microtome. Throughout the extent of GP, coronal slices from both hemispheres were sampled 1 out of 12 to check for retrograde labeling. To visualize BDA labeling in the left hemisphere, sliced were rinsed in 1X PBS and immunostained (see **Immunohistochemistry**). Slices from the bead-injected right hemisphere were unenhanced. Slices were mounted on gelatin-covered slides using an acetone-xylene drying procedure then coverslipped with DPX-medium. Sampled sections from the right hemisphere showed non-specific fluorescent microsphere labeling throughout subcortical areas and thus were not considered further. Sampled sections from left hemisphere contained cells with retrograde labeling in the GP/NB area consistent with Ch4iv and Ch4id groups. Flanking sections to those showing retrograde labeling were then double immunostained for ChAT and BDA (see **Immunohistochemistry**) and imaged as above. All experimental manipulations were performed in accordance with protocols approved by the Harvard Standing Committee on Animal Care following guidelines described in the US National Institutes of Health *Guide for the Care and Use of Laboratory Animals*.

Slice preparation. Acute brain slices were obtained from mice using standard techniques. Mice were anesthetized by isoflurane inhalation and perfused through the heart with ice-cold artificial cerebrospinal fluid (ACSF) containing (in mM) 125 NaCl, 2.5

KCl, 25 NaHCO₃, 2 CaCl₂, 1 MgCl₂, 1.25 NaH₂PO₄ and 11 glucose (~308 mOsm·kg⁻¹).

Cerebral hemispheres were removed, placed in ice-cold choline-based cutting solution (consisting of (in mM): 110 choline chloride, 25 NaHCO₃, 2.5 KCl, 7 MgCl₂, 0.5 CaCl₂, 1.25 NaH₂PO₄, 25 glucose, 11.6 ascorbic acid, and 3.1 pyruvic acid), blocked and transferred into a slicing chamber containing ice-cold choline-based cutting solution. Sagittal slices (350 μm thick) were cut with a Leica VT1000s vibratome and transferred to a holding chamber containing ACSF at 34°C for 30 minutes and then subsequently at room temperature. Both cutting solution and ACSF were constantly bubbled with 95% O₂/5% CO₂. In a subset of experiments, acute brain slices were cut in ice-cold ACSF.

Acute slice electrophysiology and two-photon imaging. Individual slices were transferred to a recording chamber mounted on a custom built two-photon laser scanning microscope (Olympus BX51WI) equipped for whole-cell patch-recordings and optogenetic stimulation. Slices were continuously superfused (3.5–4.5 ml·min⁻¹) with ACSF warmed to 32–34°C by through a feedback-controlled heater (TC-324B; Warner Instruments). Cells were visualized through a water-immersion 60x objective using differential interference contrast (DIC) illumination. Epifluorescence illumination was used to identify those cells labeled by fluorescent microspheres and/ or expressing fluorescent genetic markers. Patch pipettes (2–4 MW) pulled from borosilicate glass (G150F-3, Warner Instruments) were filled either with a Cs⁺-based low Cl⁻ internal solution containing (in mM) 135 CsMeSO₃, 10 HEPES, 1 EGTA, 3.3 QX-314 (Cl⁻ salt), 4 Mg-ATP, 0.3 Na-GTP, 8 Na₂-Phosphocreatine (pH 7.3 adjusted with CsOH; 295 mOsm·kg⁻¹

¹) for voltage-clamp recordings, or with a K⁺-based low Cl⁻ internal solution composed of (in mM) 135 KMeSO₃, 3 KCl, 10 HEPES, 1 EGTA, 0.1 CaCl₂, 4 Mg-ATP, 0.3 Na-GTP, 8 Na₂-Phosphocreatine (pH 7.3 adjusted with KOH; 295 mOsm·kg⁻¹) for current-clamp recordings. Alexa Fluor 594 (20 μM) was added to the both internals. Series resistance (<25 MΩ) was measured with a 5 mV hyperpolarizing pulse in voltage-clamp and left uncompensated. Membrane potentials were corrected for a ~7 mV liquid junction potential. After the recording was complete, cellular morphology was captured in a volume stack using 740 nm two-photon laser light (Coherent). All recorded GP-FC neurons were labeled with microspheres following injection in frontal cortex. In experiments where ChAT expression was not marked fluorescently, ChAT⁺ or ChAT⁻ GP-FC neurons were distinguished based on soma size and spontaneous firing rate in cell attached mode. Cortical neurons were classified as pyramids or interneurons based on dendritic morphology and GAD67^{GFP} expression.

Acute slice data acquisition and analysis. Membrane currents and potentials were recorded using an Axoclamp 700B amplifier (Molecular Devices) filtered at 3 kHz and digitized at 10 kHz using National Instruments acquisition boards and a custom version of ScanImage written in MATLAB (Mathworks). Electrophysiology and imaging data were analyzed offline using Igor Pro (Wavemetrics), ImageJ (NIH), MATLAB (Mathworks) and GraphPad Prism (GraphPad Software). In figures, voltage-clamp traces represent the average waveform of 3–6 acquisitions; current-clamp traces are individual acquisitions. Passive membrane properties were calculated from current deflections in voltage-clamp ($V_{\text{hold}} = -70$ mV). Cells were considered spontaneously active with maintained action

potential firing (>20s) within 2 minutes of whole-cell break in. Average V_{rest} was calculated for non-spontaneously active cells 1-3 minutes after break in. Peak amplitudes were calculated by averaging over a 1 ms window around the peak. In Figure 4.14 d,e, AMPAR and NMDAR currents were isolated from the stimulation artifact by subtracting the NBQX resistant component ($V_{hold} = -70$ mV) followed by the CPP/NBQX resistant component ($V_{hold} = +40$ mV) following a 3 minute wash-in period from current averages consisting of 10-15 consecutive acquisitions (20 s inter-stimulus interval). For pharmacological analyses in Figure 4.15d,e current averages were calculated from 15 consecutive acquisitions (20 s inter-stimulus interval) before and after a 3 minute wash-in period and then normalized to averages corresponding to the same time with no drug flow in. For pharmacological analyses in Figure 4.10c and Figure 4.12e,f, 3-7 consecutive acquisitions (20 s inter-stimulus interval) were averaged following a 3 minute wash-in period for NBQX and CPP or a 4 minute wash-in period for MEC, MLA, and DH β E. For TTX and 4AP conditions, current averages were composed of the acquisitions following full block or first-recovery of ChR2 evoked currents, respectively. Data (reported in text and figures as mean \pm s.e.m.) were compared statistically using the following Mann-Whitney test or Fisher's Exact test. *P* values smaller than 0.05 were considered statistically significant.

Optogenetic and electrical stimulation in acute slices. To activate ChR2 in acute slices, 473 nm laser light (Optoengine) was focused onto the back aperture of the 60x water immersion objective to produce collimated whole-field illumination. Square pulses of

laser light were delivered every 20 seconds and power was quantified for each stimulation by measuring light diverted to a focal plane calibrated photodiode through a low-pass dichroic filter. For ChR2 activation of dSPN or iSPN inputs onto GP-FC cells (*Drd1a-Cre*;Rosa26^{lsl-ChR2-EYFP/+} or *Adora-Cre*;Rosa26^{lsl-ChR2-EYFP/+} mice), a consistent light stimulation (1 ms; 1.3 mW·mm⁻²) was delivered directly over the recorded cell and the resulting currents were used to compare synaptic strength across cells. For paired-pulse comparisons, the objective was moved 0.16 – 1.4 mm into dorsal striatum (median = 0.4 mm) and stimulation strength and duration (0.5–1 ms; 0.06 –4.4 mW·mm⁻²) were adjusted to produce 1st peak currents between 26 – 547 pA (median = 226 pA). Stronger light powers (2-7 ms;4.4 mW·mm⁻²) were used activate ChR2 in *ChAT*^{i-Cre} cells (*ChAT*^{i-Cre};Rosa26^{lsl-ChR2-EYFP/+} mice) in cortex. For ChR2 introduced with rAAVs, light (2 ms;1.3-4.4 mW·mm⁻²) was used across conditions except in some cases following bath application of TTX and 4AP where increasing the power or duration of light stimulation was necessary to recover currents (for example, changing the duration from 2 to 4 ms). For electrical activation of the STN axonal projection into the GP, a bipolar tungsten electrode (TST33A10KT; World Precision Instruments) was placed at the anterior border of the STN and 0.1-0.5 ms square pulse of current was applied and power adjusted to maintain evoked currents while minimizing the stimulus artifact.

Reagents. Drugs (all from Tocris) were applied via bath perfusion: SR95531 (10 μM), tetrodotoxin (TTX; 1 μM), 4-aminopyridine (4AP; 500 μM), Scopolamine (10 μM), (2S)-3-[[[(1S)-1-(3,4-Dichlorophenyl)ethyl]amino-2-hydroxypropyl]](phenylmethyl)phosphinic

acid (CGP 55845; 5 μ M), *N*-(Piperidin-1-yl)-5-(4-iodophenyl)-1-(2,4-dichlorophenyl)-4-methyl-1*H*-pyrazole-3-carboxamide (AM-251; 10 μ M), 2,3-dihydroxy-6-nitro-7-sulfamoyl-benzo(*f*)quinoxaline (NBQX; 10 μ M), *R,S*-3-(2-carboxypiperazin-4-yl)propyl-1-phosphonic acid (CPP; 10 μ M), *N*,2,3,3-Tetramethylbicyclo[2.2.1]heptan-2-amine, (MEC; 10 μ M), [1 α ,4(*S*),6 β ,14 α ,16 β]-20-Ethyl-1,6,14,16-tetramethoxy-4-[[[2-(3-methyl-2,5-dioxo-1-pyrrolidinyl)benzoyl]oxy]methyl]aconitane-7,8-diol (MLA; 0.1 μ M), (2*S*,13*bS*)-2-Methoxy-2,3,5,6,8,9,10,13-octahydro-1*H*,12*H*-benzo[*j*]pyrano[3,4-*g*]indolizin-12-one (DH β E; 10 μ M), (*S*)-(-)-5-Aminosulfonyl-*N*-[(1-ethyl-2-pyrrolidinyl)methyl]-2-methoxybenzamide ((-)-sulpiride; 10 μ M) and (4*aR*-trans)-4,4*a*,5,6,7,8,8*a*,9-Octahydro-5-propyl-1*H*-pyrazolo[3,4-*g*]quinolone ((-)-Quinpirole; 8 μ M). CPP and NBQX were combined to make a cocktail of antagonists to target ionotropic glutamate receptors, while MEC, MLA and DH β E were combined to make a cocktail to antagonize nicotinic receptors.

Biocytin labeling of STN axonal projections. Acute parasagittal slices (350 μ m thick, 10° off-sagittal) were prepared from wild type mice (post natal day 34) as described above. This cutting orientation preserves the reciprocal connections between the subthalamic nucleus (STN) and the GP¹¹. In circulating warm ACSF (32-34°C), patch pipets filled with biocytin (0.2%, Molecular Probes) containing internal solution containing (in mM) 135 mM KMeSO₄, 5 mM KCl, 5 mM HEPES, 4 mM Mg-ATP, 0.3 mM Na₂-Phosphocreatine (pH 7.4 adjusted using KOH; 295 mOsm·kg⁻¹) were targeted to the STN under DIC illumination. A picospritzer (Picospritzer III; Parker Instrumentation) was used to puff

the solution into the center of STN for 1 hour (400 ms pulse at 1 Hz, 5-10 PSI). The slice was allowed to recover for 0.5 hour before being transferred to 4% PFA in 1x PBS overnight. The following morning, slices were rinsed in 1x PBS before avidin-biotinylated HRP complex (ABC) processing (Vectastain)¹². Slices were then wet-mounted onto glass slides, coverslipped, and imaged under bright-field illumination using the 10x objective of an Olympus VS110 slide scanner microscope.

***In vivo* physiology.** At least 1 week after the initial injections, mice were surgically implanted with a permanent titanium headpost. In this surgery the coordinates for GP, FC, and M1 were marked on the surface of the skull based on stereotaxic coordinates. The headpost was secured and the animal's skull was covered with C&B metabond (Parkell Inc). Animals subsequently singly housed and allowed to recover for 1 week before habituation to restraint. Mice were water restricted (to 80% of their free feeding weight) and habituated to restraint in a custom-made lever-press training rig. This rig allows the animal to press a lever in response to an auditory cue. Animals were trained for increasing durations for at least 3 days until they were able to tolerate head restraint for 90 min without struggling. During this time animals achieved an intermediate level of performance on the task, where they knew the association between lever press and reward, but were not proficient at recognizing and responding to tones. One day before the first recording day animals were anesthetized with isoflurane and received a craniotomy over the region of interest. In this surgery, a chronic fiber (62.5 μ m core multimode fiber, ecablemart.com) attached to a ceramic LC ferrule (Pfp Inc.) was

implanted at the same coordinates as the GP viral injection but at depth 3.0 mm. All chronic fibers were pre-screened to have >80% transmission at 473 nm light. A ceramic ferrule connector linked the chronic fiber to a standard LC cable. Light shuttering and output control was through an accuosto optic modulator (AA systems) and had >1000:1 occlusion ratio. Recordings were made using 16 or 32 channel silicone probes with 177 μm^2 recording sites (Neuronexus Technologies) spaced 50 μm apart and lowered to a depth of ~ 1000 μm below the surface of the brain. Optrode recordings were made with a 16 channel probe of the same configuration fitted with a fiberoptic 100 μm above the top recording site (Neuronexus Technologies, OA series). All *in vivo* electrophysiology was acquired using the omniplex system (Plexon Inc) and filtered at 300-8 KHz. Spike detection was done by level crossing generally at 50 μV and clustering to remove the noise cluster using offline sorter (Plexon Inc). Units that were separable were counted separately, but many units were accepted as multi-unit. All analysis here assumes each unit as a possible multi-unit and is only separated when necessary. All analysis was performed using custom scripts in Igor Pro and etch-a-sketch. Data visualization and statistical analysis was done using Igor Pro and GraphPad Prism.

Three-dimensional brain reconstruction and analysis. Following fixation, brains were frozen and sectioned at 50 μm . GFP and tdTomato were immunoenhanced in free floating sections using mouse-anti GFP (1:1000, abCam ab1218) and rabbit-anti RFP (1:2000, Rockland Antibodies 600-401-379) followed by anti-mouse Alexa488 (1:200, Jackson Immunoresearch 115-545-062) and anti-rabbit Cy3 (1:2000; Jackson

Immunoresearch 111-165-144) secondary antibodies. Sections were mounted on slides and counterstained with Neurotrace Blue (Invitrogen) and imaged on a Zeiss microscope with a Ludl motorized stage controlled with Neurolucida software (Microbrightfield). Imaging was done with a 10x objective and a Hamamatsu Orca Flash 4 camera. Each coronal section containing between 80-200 tiles merged with Neurolucida software. Coronal sections were aligned and Nissl labeling normalized using Neurolucida, Adobe Photoshop and ImageJ software. Aligned sections were rendered in three dimensions and cortical areas defined using Imaris software (Bitplane). Custom algorithms were written in MATLAB (Mathworks) to detect and quantify axons by cortical area. Briefly, multiscale hessian filtering¹³ was followed by non-maximum suppression and then by hysteresis thresholding¹⁴. Hysteresis thresholds were applied to both the response (largest eigenvalue of hessian) and anisotropy (difference of eigenvalues after normalizing by Gaussian filter response).

Array Tomography. Mice were deeply anesthetized with isoflurane and transcardially perfused with 4% PFA, 2% Sucrose in 0.1 M sodium phosphate buffer (1x PBS). Brains were post-fixed for 1 day, washed in 1x PBS and sectioned into 300 μ m sagittal slabs using a Vibratome (Leica). Frontal cortex was then cut out using a razor blade and dehydrated through a series of alcohol dilutions before being infiltrated with LR White acrylic resin (Sigma Aldrich L9774-500G) overnight. Tissue was then placed in a LR White filled gel cap that was polymerized at 50°C overnight. Blocks of tissue were cut on an ultramicrotome (Leica EM UC7) into ribbons of 70 nm thin sections. Sections were then

manually lifted onto gelatin coated slides, air dried and then heated on a hot plate (80°C) for ten minutes. Slides were marked by Pap Pen liquid blocker. Ribbons were treated with 50 mM glycine in TBS for 5 minutes, followed by 5 minutes in blocking buffer (5% BSA, .05% Tween 20 in TBS) before primary antibody staining. Staining was performed in blocking buffer overnight at 4° C. The dilutions and staining order are as follows:

Stain 1: chκGFP 1:100(GTX13970, GeneTex); musαGephyrin 1:100(612632, Biosciences Pharmingen); rabαGAD 65-67 1:1000(ab11070, Abcam)

Stain 2: rabαPSD95 1:100(3450, Cell Signaling Tech.)

Stain 3: musαBassoon 1:100 (ab82958, Abcam); rabαSynapsin 1 1:100 (5297S, Cell Signaling Tech.)

Stain 4: rabαParvalbumin 1:100(PV-25, Swant)

Stain 5: musαVACHT 1:100(139 103, Synaptic Systems); rabαVGAT 1:100(131 011, Synaptic Systems)

Imaging was performed using a Zeiss Axio Imager Z1 Upright Fluorescence Microscope. A position list was generated at 20x in cortex to identify the ROI on each section. Four images were then acquired with Zeiss Plan-Apochromat 63x/1.4 Oil DIC Objective and stitched into a single final image (Mosaix, Axiovision). Individual stacks were aligned in FIJI using the MultiStackReg plugin, initially using the DAPI channel and then a second alignment to the stack from the first imaging session. Fine alignments were the performed using the Synapsin1 stack and the Register Virtual Stack Slices plugin of FIJI to correct for warping. Background fluorescence was then subtracted from the aligned

stacks using a 10 pixel rolling ball filter and contrast was adjusted to 0.1% through the FIJI software. Image analyses were carried out with custom written scripts in MATLAB (Mathworks). GFP⁺ “pearls” and diffraction-limited synaptic markers were computationally detected from image stacks. Pearls were identified as belonging to a “string,” with multi-plane spanning volumes. All synaptic markers were treated as single pixel point-sources within a given z plane. Images were segmented to exclude DAPI⁺ nuclei and areas containing no tissue. Co-localization analyses of GFP⁺ pearls and synaptic markers were performed by quantifying the occurrences/voxel at particular distances for the real data or following rounds of spatial randomization for either the GFP⁺ pearls or synaptic markers. Z scores were calculated from 0 distance occurrences in the real data and following 10 rounds of randomization using the same pearl volumes.

REFERENCES

1. Rossi, J. *et al.* Melanocortin-4 Receptors Expressed by Cholinergic Neurons Regulate Energy Balance and Glucose Homeostasis. *Cell Metab* **13**, 195–204 (2011).
2. Vong, L. *et al.* Leptin Action on GABAergic Neurons Prevents Obesity and Reduces Inhibitory Tone to POMC Neurons. *Neuron* **71**, 142–154 (2011).
3. Taniguchi, H. *et al.* A Resource of Cre Driver Lines for Genetic Targeting of GABAergic Neurons in Cerebral Cortex. *Neuron* **71**, 995–1013 (2011).
4. Tallini, Y. N. *et al.* BAC transgenic mice express enhanced green fluorescent protein in central and peripheral cholinergic neurons. *Phys Genomics* **27**, 391–397 (2006).
5. Madisen, L. *et al.* A robust and high-throughput Cre reporting and characterization system for the whole mouse brain. *Nat Neuro* **13**, 133–140 (2010).

6. Madisen, L. *et al.* A toolbox of Cre-dependent optogenetic transgenic mice for light-induced activation and silencing. *Nat Neuro* 1–12 (2012).
7. Tong, Q., Ye, C.-P., Jones, J. E., Elmquist, J. K. & Lowell, B. B. Synaptic release of GABA by AgRP neurons is required for normal regulation of energy balance. *Nat Neuro* **11**, 998–1000 (2008).
8. Tamamaki, N. *et al.* Green fluorescent protein expression and colocalization with calretinin, parvalbumin, and somatostatin in the GAD67-GFP knock-in mouse. *J Comp Neurol* **467**, 60–79 (2003).
9. Saunders, A., Johnson, C. A. & Sabatini, B. L. Novel recombinant adeno-associated viruses for Cre activated and inactivated transgene expression in neurons. *Front Neural Circuits* **6**, 47 (2012).
10. Mesulam, M. M., Mufson, E. J., Levey, A. I. & Wainer, B. H. Cholinergic innervation of cortex by the basal forebrain: cytochemistry and cortical connections of the septal area, diagonal band nuclei, nucleus basalis (substantia innominata), and hypothalamus in the rhesus monkey. *J Comp Neurol* **214**, 170–197 (1983).
11. Beurrier, Y., Ben-Ari, Y. & Hammond, C. Preservation of the direct and indirect pathways in an in vitro preparation of the mouse basal ganglia. *Neuroscience* **140**, 77–86 (2006).
12. Marx, M., Günter, R. H., Hucko, W., Radnikow, G. & Feldmeyer, D. Improved biocytin labeling and neuronal 3D reconstruction. *Nat Protoc* **7**, 394–407 (2012).
13. Eberly, D., Gardner, R., Morse, B., Pizer, S. & Scharlach, C. Ridges for image analysis. *Journal of Mathematical Imaging and Vision* **4**, 353–373 (1994).
14. Canny, J. A computational approach to edge detection. *IEEE Trans Pattern Anal Mach Intell* **8**, 679–698 (1986).

Chapter 5

Conclusions and Outlook

Following the experimental framework outlined in the introduction, this thesis has extended our understanding of how BG cell types control cortical activity. In Chapter 3 we show that during development, activity in iSPNs and dSPNs oppositely affects motor behavior and the excitatory drive of cortical and thalamic inputs into the striatum. These results confirm the phenomenology of the accepted pathway model of BG function. However, the constituent cell types considered in the model are drastically oversimplified. Using novel rAAVs outlined in Chapter 2 to systematically describe this complexity, we describe in Chapter 4 two GP cell types that provide a direct output of the BG to cortex. The presence of a non-thalamic BG output necessitates a major revision to the underlying circuitry by which iSPNs and dSPNs affect cortex. Listed below are short summaries for each chapter with a selection of results for further discussion and future study.

Chapter 2. Novel recombinant adeno-associated viruses for Cre activated and inactivated transgene expression in neurons

Summary: We developed rAAV vectors that use alternative lox sites to achieve Cre-mediated inhibition of transcription. These novel “Cre-Off” rAAVs can be used with other “Cre-On” rAAVs or nuclear transgenic elements that use more common loxp and lox2272 sites.

Discussion/Future Work

•**Mechanisms of rAAV interference.** rAAVs that share lox sites with other transduced rAAVs or genomic loci can interfere with transcription. One mechanism could be inter-molecular Cre-mediated insertion of rAAV DNA. This mechanism should be tested directly. If rAAVs are capable of inserting parts of their backbones into genomic loci carrying lox sites, this phenomenon may offer a novel mechanism for transgenesis at endogenous loci. Since rAAVs have been touted as promising vectors for gene therapy, preventing the putative insertion of rAAV DNA into the nuclear genome would greatly improve the safety of rAAVs us in humans.

Chapter 3. Recurrent network activity drives striatal synaptogenesis

Summary: Here show that post-natal activity in dSPNs and iSPNs of striatum has opposite effects on the development of glutamatergic synaptogenesis on SPNs

themselves. This phenomenon is not cell autonomous but rather depends on activity throughout the BG, thalamus and cortex.

Discussion/Future Work

•**Spatial structure of recurrent feedback.** The BG are believed to be organized in a parallel looped architecture, yet little is known about the anatomical or functional nature of these putative loops. Motor regions of the BG display rough somatotopy and inter-BG axonal projections maintain a roughly parallel organization. However the functional “closedness” for any synaptic loops within the BG has not been directly evaluated. Careful anatomical work challenges the parallel nature of these loops. First, the BG show large-scale changes in spatial convergence/divergence of axonal inputs across nuclei, which differ drastically in both volume and cell number. For example, in rat¹, stereological estimates of total neuron number per nuclei are:

Cortex > **Striatum** (2.79×10^6) > **GP** (4.6×10^4) > **SNr** (2.63×10^4) > **STN** (1.36×10^4) > **SNC** (7.2×10^3) > **GPI** (3.2×10^3)

In terms of ratios, for a single STN neuron, there are ~3.4 in the GP, ~0.5 in the SNC, and ~ 200 cells in the striatum. Second, single-cell tracing experiments have demonstrated that axons from individual BG can have very large arbors. For example, dopaminergic cells of the SNC and PV- neurons of the GP arborize over huge swaths of striatal territory, and are thus positioned to innervate thousands, if not tens of thousands, of

neurons. Thus while inter-BG connectivity is roughly parallel in nature, there are anatomical opportunities for crosstalk across loops.

In the retina, crosstalk between feed-forward neural inputs is necessary for even the most basic computations such as surround excitation and inhibition. Understanding how crosstalk across loops contributes to BG computation necessitates mapping networks of synaptically connected neurons across nuclei. These networks could be visualized with synapse-hopping recombinant viruses in combination with whole-brain imaging. Once the closed vs. open architecture of a single loop is established, endoscopic imaging could be used to record neural activity from neurons across BG nuclei participating in the same or a parallel network during behavior.

To complement these challenging experiments, one could take advantage of the recurrent nature of SPN activity during development we describe to address the size and independence of these loops. SPNs in specific portions of the striatum could be manipulated and synaptogenesis assayed within and outside of those affected areas, offering functional insight into the large-scale organization of cortico-BG- thalamo feedback.

•**Role of dopamine.** The activity dependent synaptogenesis we describe not only requires glutamate, but is likely affected by other neurotransmitters and neuromodulators. In cortex, *de novo* synaptogenesis requires PKA signaling. In striatum, PKA activity can be controlled through neuromodulators like dopamine and adenosine. Dopamine is thought to have opposite effects on PKA in dSPNs and iSPNs. Whereas

D1Rs activate PKA in dSPNs, D2R inhibit PKA in iSPNs. This canonical cell signaling suggests that dopamine may drive synaptogenesis in dSPNs while inhibiting synaptogenesis in iSPNs. Coincident dopamine signaling offers a plausible mechanism for how the release of glutamate could thus lead to pathway-specific synapse formation in striatum.

How then does activity in the cortico-BG-thalamo loop self organize? Let us consider how SPN activity and dopamine could mediate both positive and negative feedback in developmental wiring. We know that dSPN activity drives while iSPN activity inhibits synaptogenesis in SPNs from both pathways. This effect is likely caused through opposite changes in the firing rates of striatal-projecting glutamatergic neurons in cortex and thalamus. Striatal dopamine signaling coincident to glutamate release could bias synaptogenesis toward dSPNs and away from iSPNs, offering a plausible mechanism how differential pathway wiring could be sculpted. Since dSPNs are thought to inhibit striatal dopamine releasing SNc neurons, dSPN activity could target the amount of pathway drive to a set point through dopamine-mediated negative feedback. This negative feedback might be necessary to compensate for the glutamate-mediated positive feedback that dSPN activity triggers through the cortico-BG-thalamo loop. Such a model not only begs for experimental scrutiny, but also highlights important theoretical concerns. For example, resolving the “chicken and the egg” phenomena with dopamine and SPN activity in development. What signals are instructive?

Activity-dependent synaptogenesis in the striatum offers a straightforward and quantitative read out to determine how dopamine, adenosine and other

neuromodulators control synapse formation in single SPN. After these contributing signals are identified, it will be important to find their cellular sources within the BG circuits. Once the sources are identified and activity monitored during development, we will have a better idea about how the rest of the brain contributes to wiring the direct and indirect pathways.

• **Role of other BG cell types.** The effects of developmental wiring caused by inhibition of dSPNs and iSPNs has lent phenomenological support for the direct and indirect pathway model of BG organization. Do other BG cell types contribute to the direct and indirect pathway? Or is this organization entirely dependent on SPNs? This question can be experimentally addressed using similar methods to dampen firing or prevent transmitter release from other cell types within the BG while assaying synaptogenesis in the striatum.

Chapter 4. A direct GABAergic output of the basal ganglia to frontal cortex

Summary: Here we show that SPNs of dorsal striatum and the STN control a projection system from the GP directly to frontal cortex. The GP-FC projections consist of two cell types which function to activate cortex by releasing either GABA or GABA/ACh mostly onto cortical interneurons. The GP-FC projection stands as a major revision to the accepted model wherein the BG modulate the cortex indirectly via the thalamus.

Discussion/Future Work

•**Cortical interactions between GP and thalamus-based BG feedback.** Activity in striatal SPNs will affect cortex through both the thalamic and non-thalamic outputs. Internal to the BG, dSPNs and iSPNs have different effects on these two outputs: GP-FC cells are inhibited by both SPN types, while dSPNs and iSPNs impose largely opposite effects on BG-thalamus cell firing. Despite these differences in internal control, both outputs increase cortical firing rates, but differ in their mechanisms: GP-FC cells activate cortex by inhibiting local interneurons, while cortico-thalamic cells increase activity through glutamatergic drive. It will be vital to understand how these two BG outputs are controlled by SPNs and interact in cortex during behavior, development and to coordinate plasticity.

•**Pathway and target-specific short-term synaptic plasticity.** dSPNs and iSPNs have distinct short-term synaptic plasticity properties onto GP-FC cells (Figure 4.14j). iSPN IPSCs are slightly facilitating, while dSPN IPSCs are depressing. These results suggest SPNs of each pathway likely recruit GP-FC cells differently. Future work should focus on describing the synaptic properties of dSPNs/iSPNs onto other GP cell types. This data could serve as the basis for understanding the how SPN activity controls GP cells *in vivo* and for defining the molecular mechanisms responsible for the cell type specific differences in synaptic properties. For example, do pathway specific pre-synaptic differences affect how bursts of SPN action potentials inhibit PV+ GP neurons that

control “downstream” nuclei such as the STN and SNr versus mostly PV- GP neurons that feedback “upstream” into striatum?

•**GP-FC cells and behavioral/cellular effects of anti-psychotics.** GP-FC cells are synaptically positioned between D2R-expressing iSPNs and interneurons of frontal cortex and thus are likely to convey at least some of the therapeutic benefit of anti-psychotic drugs. Recent genetic association studies in schizophrenic vs. healthy humans have demonstrated that variants in both D2R and nicotinic receptor subunit genes are some of the ~100 genome variants that can cause disease predisposition². This convergence of genetics with pharmacological/behavioral/post-mortem data suggests that D2R iSPNs may not just be important for the mechanism of action of anti-psychotic drugs, but can be linked to the pathophysiology of Schizophrenia.

In our simple model, Schizophrenia ensues through excessive dopamine in the striatum. Excessive dopamine tends to over-activate D2Rs on iSPNs, lowering the efficacy of iSPN inhibition onto GP-FC cells. Increased GP-FC cell activity will tend hyperactivate cortex by greater inhibition of local interneurons, causing cell type specific compensatory changes in cortical architecture over time. Experimental manipulations of activity and transmitter release in ChAT+ and ChAT- GP-FC cells in conjunction with anti-psychotic administration will be important to determine the necessity and sufficiency of this projection system for the behavioral and cellular changes induced by these drugs.

Future work will also need to define the exact interneuron and pyramidal cell types directly controlled by GP-FC cells. For example, do ChAT- innervate both

pyramidal-tract and intratelencephalic pyramidal neurons? Which exact types of interneurons do ChAT+ and ChAT- GP-FC cells control? Unpublished rabies-mediated retrograde tracing experiments from the labs of Josh Huang and Nat Heintz suggests GP-FC cells directly innervate chandelier cells in the upper regions of layer 2/3, as well as somatostatin+ interneurons and VIP interneurons expressing HTR_{3a} in mPFC.

Unfortunately, these experiments did not distinguish ChAT+ vs. ChAT- GP neurons.

Regardless of their ChAT identity, these data suggest that the GP-FC projection collectively influences cortex via a diverse set of interneuron types. While this diversity of this cortical cell connectivity may prove confusing in the short-term, in the long-term, should greatly inform how coordinated modulation of neighboring interneuron types affect cortical processing and behavior.

•**GP-FC cells for drug targeted therapy.** Typical anti-psychotic drugs can cause devastating motor side effects. Molecular characterization of GP-FC cells could present specific, drug-targetable receptors that could alter GP-FC activity without large-scale effects on dopamine signaling.

•**Mechanisms of ACh/GABA co-release from ChAT+ cells of GP and basal forebrain.** In cortex, the pre-synaptic terminals of ChAT+ GP-FC cells have a spatially mixed identity: along the same axon, some terminals contain both VGAT and VAcHt while others contain either of the vesicular transporters (Figure 4.10g-k). Importantly, VGAT and VAcHt punctae tend to be ~300 nm apart and thus likely are targeted to distinct

vesicular pools. Future work will be needed to work out the logic and mechanisms of this co-release. What distinguishes VGAT and VAcHT containing vesicles biochemically? Are these distinct vesicular pools released by the same types of activity? Do terminals containing these distinct synaptic pools target the same synapses or cell types? Is ACh vs. GABA release affected by developmental or behavior state? What role does co-release play in synaptic plasticity?

References

1. Oorschot, D. E. Total number of neurons in the neostriatal, pallidal, subthalamic, and substantia nigral nuclei of the rat basal ganglia: a stereological study using the cavalieri and optical disector methods. *J Comp Neurol* **366**, 580–599 (1996).
2. Ripke, S. *et al.* Biological insights from 108 schizophrenia-associated genetic loci. *Nature* **511**, 421–427 (2014).

Appendices

Figures in appendices contain unpublished work from Chapters 3 (Appendix A) and Chapter 4 (Appendix B) and are not referenced in the Chapters themselves. Movies in the appendix will be included with the published form of Chapter 4 but are not referenced in the Chapter 4 of this thesis.

Figure A.1. rAAV rescue of *Slc32a1* in striatum restores MSN GABAergic transmission

a. Example voltage-clamp recordings from ChR2-mCherry⁻ MSNs in D1-Cre mice. Traces are from 3 distinct mice with 1 or 0 functional *Slc32a1* alleles (*Vgat*^{fl/+} or *Vgat*^{fl/fl})

following injection of DIO-ChR2-mCherry or DIO-ChR2-mCherry + DIO-*Vgat* in striatum.

b. Summary graph of peak currents demonstrating that Cre-conditional rAAV-mediated

overexpression of *Slc32a1* is sufficient to rescue GABAergic transmission in mice where

Vgat was conditionally deleted (D1-Cre: n=20 cells *Vgat*^{fl/+} + DIO-ChR2, n=7 *Vgat*^{fl/fl} +

DIO-ChR2, n=13 cells *Vgat*^{fl/fl} + DIO-ChR2 & DIO-*Vgat*; D2-Cre: n=12 *Vgat*^{fl/+} + DIO-ChR2,

n=7 *Vgat*^{fl/fl} + DIO-ChR2, n=13 *Vgat*^{fl/fl} + DIO-ChR2 & DIO-*Vgat*). Mean±sem.

Figure A.1 (Continued)

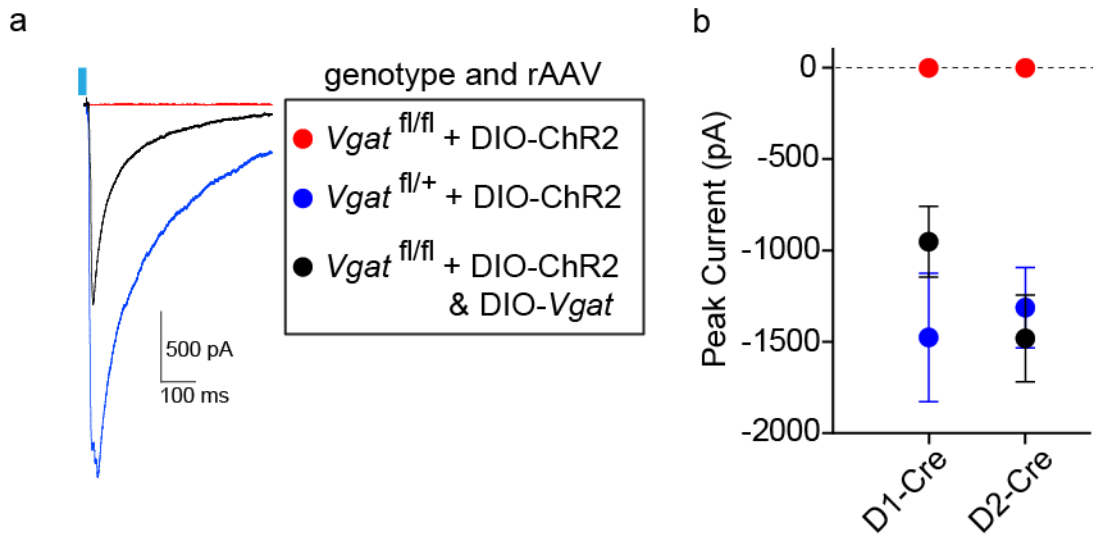
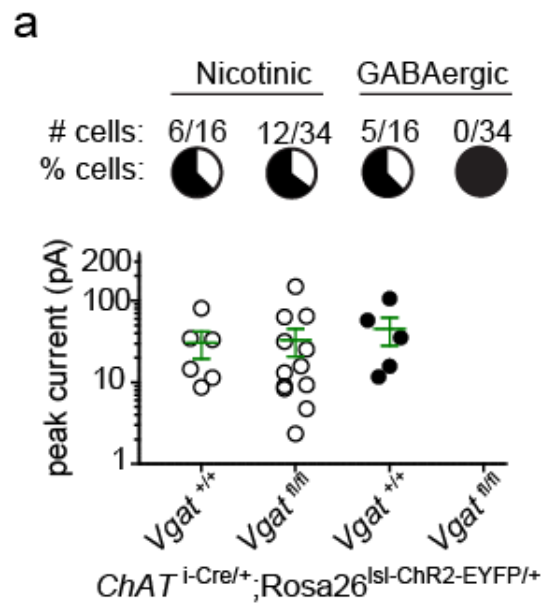


Figure B.1 Cortical GABAergic neurotransmission from *ChAT*^{i-Cre} neurons is *Slc32a1* dependent

a. Conditional knockout of *Slc32a1* (*Vgat*^{fl/fl}) from *ChAT*^{i-Cre}; *Rosa26*^{lsl-ChR2-YFP} expressing cells eliminates direct GABAergic but not direct nicotinic currents. *Top*, number and percentage of layer 1 interneurons exhibiting optogenetically evoked direct currents with 2 (*Vgat*^{+/+}) or 0 (*Vgat*^{fl/fl}) functional *Slc32a1* alleles. *Bottom*, direct current peak amplitudes.

Figure B.1 (Continued)



B.Movie 1. Three-dimensional whole-brain reconstructions of axonal projections from ChAT+ (magenta) and ChAT- (green) GP-FC cells. rAAVs DIO-EGFP (Cre-On) and FAS-tdTomato (Cre-Off) were injected into the GP and adjacent dorsal NB in a *ChAT*^{i-Cre/+} mouse. The max projection movie begins with a lateral to medial view of the injection site and Rt. A posterior to anterior fly through of cortex shows axons in frontal cortex and the lateral amygdala, followed by a medial to lateral view which exhibits subcortical projections to the Str, STN, SNr/c, PF and LH. A small amount of FAS-tdTomato expression in striatum contributes to the Cre-Off projection in SNr. Rt, thalamic reticular nucleus; Str, striatum; SNr/c, substantia nigra reticulata/compacta; PF, thalamic parafascicular nucleus; LH, lateral habenula.

B.Movie 2. Three-dimensional whole-brain reconstructions of axonal projections from iSPNs (green) and dSPNs (magenta) from dorsal striatum into GP/dorsal NB.

rAAVs DIO-EGFP (Cre-On) and FAS-tdTomato (Cre-Off) were injected into the dorsal striatum of *D2r-Cre* mouse, to differentially label Cre⁺ iSPNs and Cre⁻ non-iSPNs. Since SPNs provide the only output of striatum, this strategy selectively labels iSPN and dSPN projections. Following a rotated lateral view of the whole brain, the movie proceeds anterior to posterior, following single coronal slices through the injection site and back and forth through the GP before continuing to the SNr. Visualizing iSPNs and dSPNs individually illustrates that dSPN axons arborize widely in the ventral and posterior regions of GP/NB containing GP-FC cells.